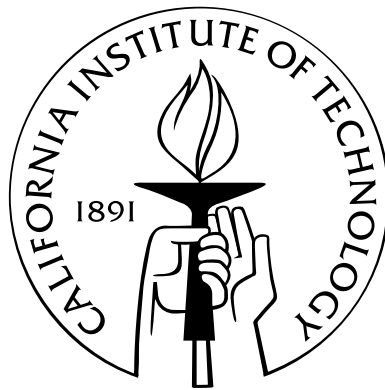# Faint optically selected AGN at $z = 3$

Thesis by

Matthew Philip Hunt

In Partial Fulfillment of the Requirements

for the Degree of

Doctor of Philosophy

California Institute of Technology

Pasadena, California

2004

(Defended May 20, 2004)

For my parents.

Acknowledgements

First and foremost, I would like like to thank my advisor, Chuck Steidel, without whom this thesis would not have been possible. His generosity with his time, ideas, and resources was considerable and essential. My fellow travellers in the group, especially Alice Shapley and Kurt Adelberger, not only contributed to the science of this thesis, but also to my happiness as a graduate student. I don't know how I would have survived so many nights in so many domes (through blizzards, earthquakes, fires, and aurorae) without their conversation and friendship. It seems like Dawn Erb and Naveen Reddy just joined the group, but it has been a few years and countless observing runs, and I am grateful for their company and input.

This thesis also required the hard work of the staff members at the Keck and Palomar observatories. Rick Burruss, Karl Dunscombe, and Jean Mueller spent more time with me at Palomar than anyone should endure, and their respect for the telescope and its science is revealed in their dedication. Palomar Observatory is one of the most special places I have been privileged to visit. The day crew, night assistants, and Monastery hosts all contribute to the best observing environment I can imagine.

Gwen Porter managed to balance the despair of first-year classes with fun and humor, along with the occasional bottle of beer. Mike Santos was always available for pie or conversation, no matter how many deadlines of his own he had. No topic, from large-scale structure formation to monetary policy to teen movies, escaped his grasp. Bryan Jacoby has been the steadiest, best friend I could ask for. Our constant conversations on topics scientific, political, automotive, and œnological required him to spend months in Australia, where he could actually get some work done.

Rob Simcoe and George Becker have not only been wonderful officemates, but as Wal's protégés, their understanding of QSO and IGM phenomena has proved helpful. Jon Sievers, a font of knowledge if there ever was one, led us to multiple victories at the intramural Quiz

Abstract

We present the results of two surveys for $z \approx 3$ AGN, the Lyman break galaxy (LBG) survey and a new survey based on the same techniques, but over a wider area. These surveys, spanning more than 2 deg^2, yield 24 new QSOs, and 17 new narrow-lined AGN. The combined data from these surveys span a range of luminosity that is unprecedented at high redshift, covering 6.5 mag of the faint end of the QSO luminosity function. We find a substantially flatter faint-end slope at high redshift than in the local universe, $\beta_l = 1.20$, which has important implications for the study of supermassive black hole (SMBH) accretion and galaxy formation, as well as the state of the IGM at $z \approx 3$. We also present estimates of the QSO lifetime ($\sim 10^7$ yr) and compare our AGN sample with those obtained by deep X-ray imaging. We also present a guide to the reduction of imaging data from the Large Format Camera (LFC) on the Hale Telescope.

Contents

List of Figures

Chapter 1

Introduction

1.1   Background and motivation

The demographics of $z \approx 3$ QSOs have been a popular subject of study for many years. Such work has direct implications for the state of the IGM (due to the UV radiation of QSOs), and also on our understanding of galaxy and SMBH formation. Important, well-characterized surveys, including the work of Schmidt et al. (1995), Boyle et al. (1988, 2000), Kennefick et al. (1995), and Fan et al. (2001b), have contributed to the measurement of the QSO luminosity function (QSO LF) at $z \approx 3$. However, all of these surveys have an important limitation: Because of the large distance modulus to $z = 3$, these surveys only went deep enough to observe the brightest QSOs at that redshift.

As a consequence, until the work described in this thesis, there was little reliable information about the demographics of faint QSOs in the distant universe. Pei (1995) drew together an overview of our knowledge of the QSO LF at all redshifts. He found that a double-power law, like that proposed by Boyle et al. (1988), was a good fit to existing LF data at all redshifts, and that there was no evidence for evolution in the faint-end slope $(\beta_l = 1.64)$[1], bright-end slope $(\beta_h = 3.52)$, or normalization $(\Phi_\star)$. The redshift evolution of the LF could be modeled with pure luminosity evolution (PLE): The luminosity of the power-law break is a function of redshift, $L_z(z)$. The functional form of $L_z(z)$ was a Gaussian in z; clearly, this is not a physically-motivated model, but a successful approximation

---

[1]Unless otherwise specified, an $\Omega_m = 1$, $\Omega_\Lambda = 0$, $h = 0.5$ cosmology is used throughout this thesis. This cosmology facilitates comparison with most QSO LF work.

to the data. The expressions describing the Pei (1995) model are as follows:

$$\Phi(L, z) = \frac{\Phi_\star / L_z}{(L/L_z)^{\beta_l} + (L/L_z)^{\beta_h}} \tag{1.1}$$

$$L_z(z) = L_\star (1 + z)^{-(1+\alpha)} \exp[-(z - z_\star)^2 / 2\sigma_\star^2] \tag{1.2}$$

Here, $z_\star = 2.75$, which may be considered the redshift of peak QSO activity, and $\sigma_\star = 0.93$. The normalization is $\log(\Phi_\star / \mathrm{Gpc}^{-3}) = 2.95$ and the luminosity of the power law break is derived from $\log(L_\star / L_\odot) = 13.03$. The typical spectral index of QSOs is taken to be $\alpha = -0.5$, a value which is generally used throughout this thesis. The Pei (1995) fit was obtained from LF data in the rest-frame B band, which was the most common choice at the time. Rest-frame 1450 Å magnitudes, in the continuum between Lyman-α and C IV, have largely replaced B magnitudes at high redshift, for ease of measurement in the optical. AB 1450 Å magnitudes are generally used throughout this thesis, with other results being transformed to this system as necessary.

There are some important limitations to the Pei (1995) fit, however. First, as described above, data on the faint end of the LF were available only at low redshift. Thus, while a constant β_l was able to fit the available data at all redshifts, the high redshift data did not contribute to this constraint. This thesis offers results that improve our understanding of the faint end at high redshifts. Second, even at the bright end, data were limited to $z \lesssim 4.5$, and offered minimal constraints on the bright-end slope at $z \gtrsim 3.5$. Since then, we have learned that the bright-end slope is *not* constant at all redshifts; Fan et al. (2001b) have used Sloan Digital Sky Survey (SDSS) data to demonstrate that $\beta_h \approx 2.5$ at $z \approx 4$, significantly flatter than the slope of 3.52 at lower redshifts.

Why has it taken so long to measure the faint end of QSO LF at high redshift? At first glance, the problem may not seem daunting. At $z \approx 3$, observing a number of QSOs down to g' or r' of 24 mag would yield a useful measurement, and such magnitudes are easily reached with modern telescopes and instruments, for both imaging and spectroscopy. The problem is twofold. At the faintest magnitudes, say $r' \gtrsim 24$, QSOs are substantially outnumbered by non-active galaxies at the same redshift, and it is difficult to distinguish between them by photometry[2]. Thus, a large number of faint candidates must be observed

---

[2]Except, perhaps, by many-filter photometry (which is essentially very-low-resolution spectroscopy); for example, COMBO–17 (Wolf et al. 2003). Deep imaging through a large number of filters naturally requires a substantial amount of telescope time, and thus is not a complete solution to the problem.

spectroscopically, and only a small fraction of them will yield the desired prey. A QSO survey conducted in this regime would be very costly in effort and telescope time.

At brighter magnitudes, but still within the faint end of the LF ($24 \lesssim r' \lesssim 21$), the problems are different. Contamination by galaxies is no longer a serious problem. QSOs at these magnitudes are less common than fainter ones, due to the shape of the LF, and contamination from stars may be expected (depending on the details of one's color selection). This source of contamination is not necessarily excessive or difficult to deal with, as we will discuss later. The biggest problem is simply that QSOs are fairly rare objects, and a survey needs to cover a substantial amount of sky (at least a couple of square degrees). It was only recently that wide-field mosaic CCD imagers, such as the Mosaic camera (Muller et al. 1998) on the KPNO 4-m Mayall Telescope and the Large Format Camera (LFC; Simcoe 2003) on the 5-m Hale Telescope, became available. Instruments like these make such surveys considerably more feasible.

In this thesis, we discuss the sample of QSOs[3] (as well as narrow-lined AGN) discovered in two surveys. The first was the survey for Lyman break galaxies (LBGs; Steidel et al. 2003), which is introduced in §1.2 and presented in detail in Chapters 2 and 3. The second is a survey specifically targeting medium-luminosity QSOs, which is introduced in §1.3 and discussed more thoroughly in Chapter 4. In addition to the discussions in their respective chapters, an overview of the survey results, and their implications, is provided in §1.4. Finally, Chapter 5 presents a method for the efficient reduction of LFC data, which was used for the work in this thesis, and has been widely adopted by the Palomar observing community.

1.2   The LBG survey

In the mid-1990's, an ambitious survey was undertaken to discover and study a large sample of star-forming galaxies at $z \approx 3$. The survey took advantage of photometric pre-selection made possible by the "Lyman break" in the SED of such galaxies, and we refer to the galaxies as Lyman break galaxies (LBGs), and the survey as the LBG survey. The methodology, which is described more completely by Steidel & Hamilton (1993) and Steidel et al. (2003),

---

[3]Throughout this thesis, "QSO" and "type I AGN" are both used to refer to any AGN with broad emission lines, without imposing a minimum luminosity. "Narrow-lined AGN (NL AGN)" and "type II AGN" refer to any AGN with narrow emission lines. In the observed spectra, there is a clear dichotomy between these groups.

was to image a survey field in three filters, U_n, G^4, and $\mathcal{R}$, with 4–5 m telescopes. The bandpasses of these filters, not including atmospheric opacity, are shown in Figure 1.1. The $\mathcal{R}$ filter is a custom filter, which is wider than r' or i', and whose central wavelength is intermediate between them.

The imaging data were used to select candidates for spectroscopic observation, based on the following photometric criteria:

$$\mathcal{R} > 19 \tag{1.3}$$

$$\mathcal{R} < 25.5 \tag{1.4}$$

$$G - \mathcal{R} < 1.2 \tag{1.5}$$

$$(G - \mathcal{R}) + 1 < (U_n - G) \tag{1.6}$$

The criterion fundamental to the Lyman break technique, Equation 1.6, selects for objects whose 912 Å Lyman break falls between the U_n and G filters; in other words, at $z \approx 3$. A diagram of the selection window in color space is shown in Figure 1.2.

Whether due to the intrinsic SED, or the substantial opacity of the IGM at $z \approx 3$, QSOs at that redshift also show a Lyman break in their spectra, and hence are included in the photometric selection process as well. They are, in a sense, a "contaminant" in the survey for normal star-forming galaxies, albeit a very small one. At its completion, the LBG survey covered 0.38 deg^2 in 17 fields. 2,347 objects met the photometric criteria listed above, and 1,320 of those (56%) were observed spectroscopically at the W. M. Keck Observatory using the Low Resolution Imaging Spectrometer (LRIS; Oke et al. 1995). Of those, 957 (72%) objects were identified as galaxies at $z > 2$. Twelve of those[5] (1.2%) were QSOs. Another 16 objects were identified as NL AGN.

It is clear that such a survey, taking hundreds of hours on large telescopes, would not have been undertaken for the sole purpose of finding a dozen faint QSOs. But the LBG survey, having been devised and executed for other purposes, provides us with an unprecedented collection of faint, distant QSOs combined with a readily characterized survey methodology.

---

[4]U_n and G are essentially identical to the more recent u' and g' filters. The names are used interchangeably in this thesis, generally reflecting the "official" names of the filters used in particular observations.

[5]One of the twelve was known *a priori*.
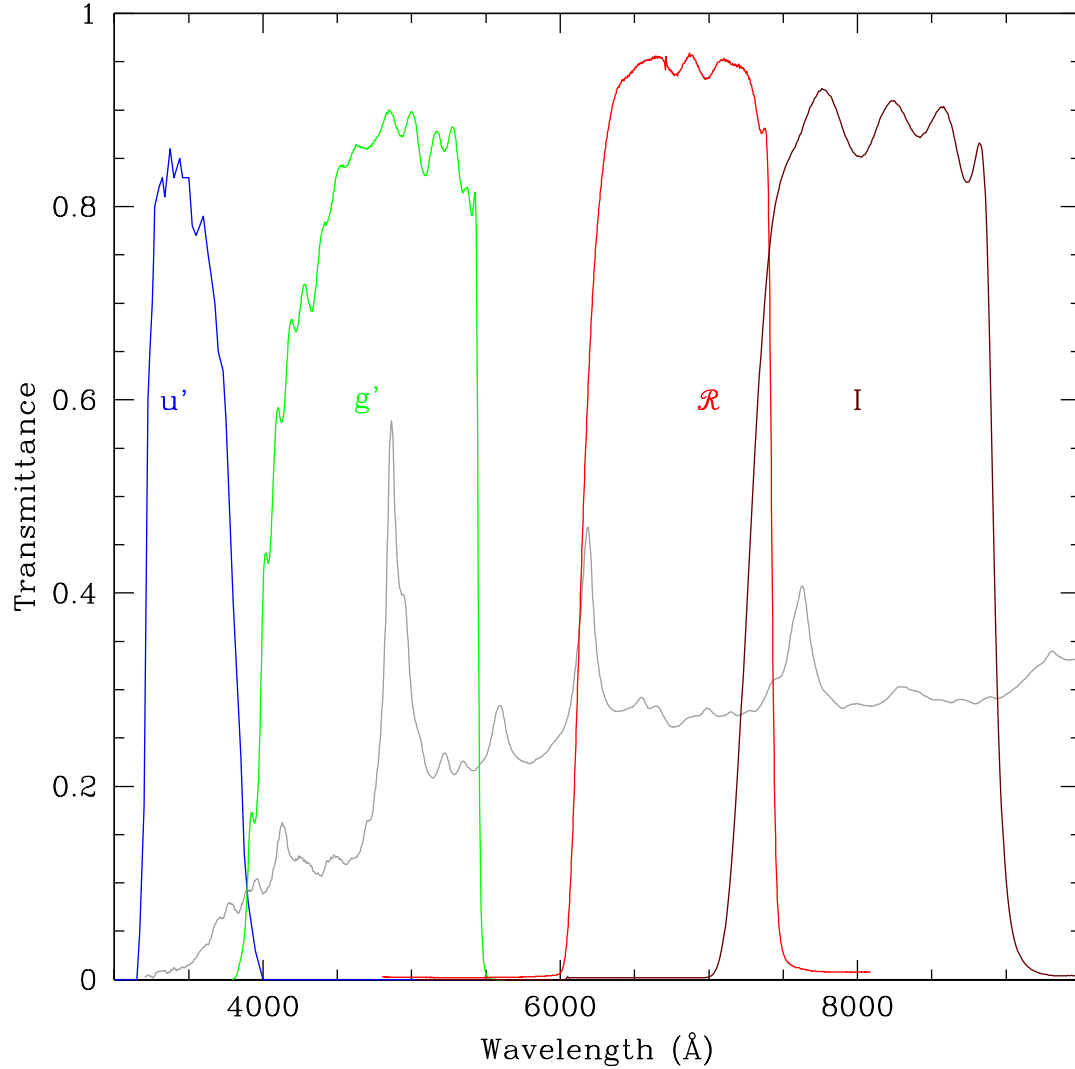
Figure 1.1 The $u'g'\mathcal{R}I$ filter set used for the surveys described in this thesis. The u' and g' filters are essentially identical to the U_n and G filters referred to in certain LBG survey papers (e.g., Steidel & Hamilton 1993). The I filter is not used for $z \approx 3$ selection, but is useful for similar techniques at lower redshifts. A typical $z = 3$ QSO spectrum is superimposed, to illustrate the observed wavelengths of the Lyman break and emission lines.
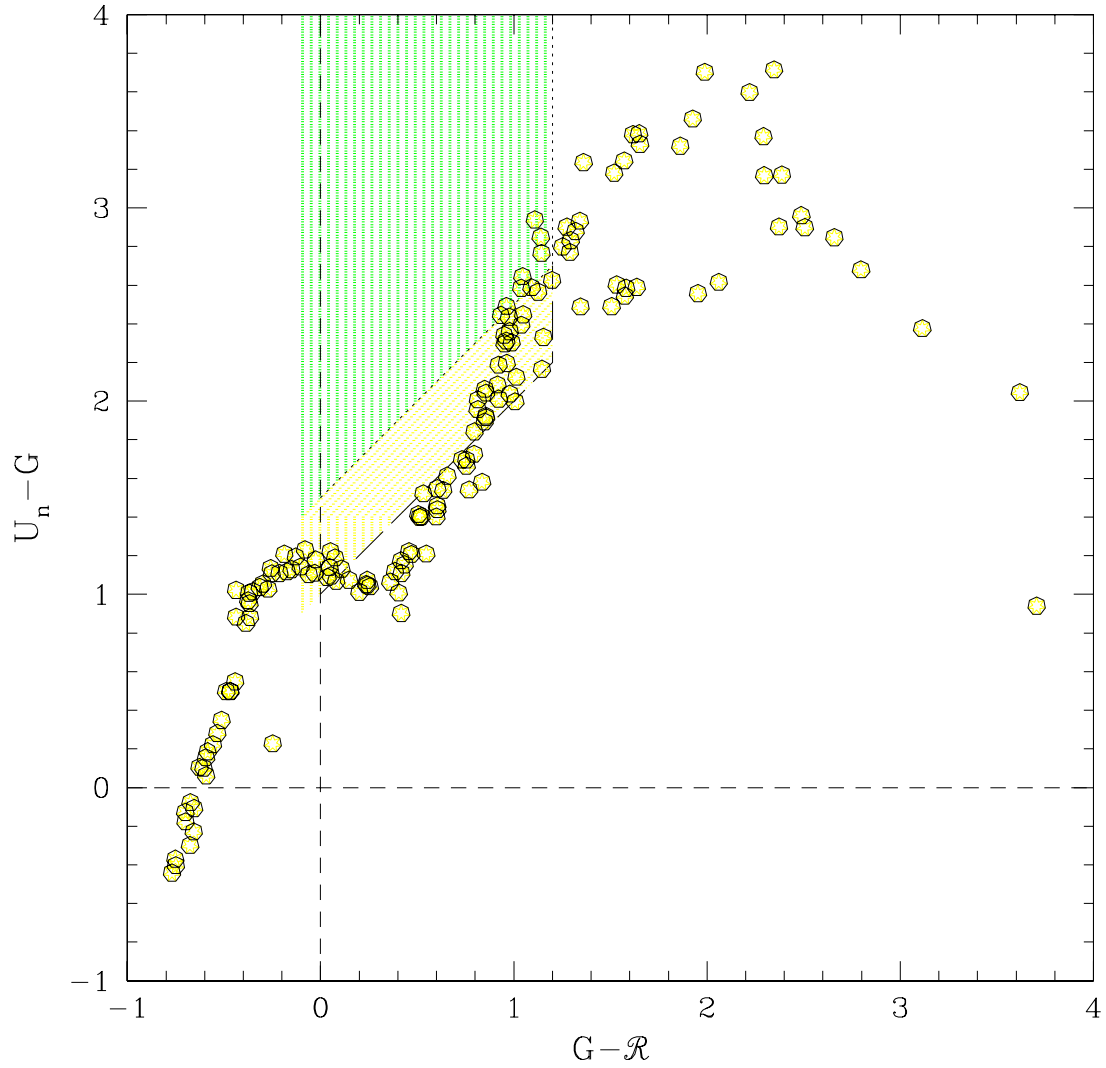
Figure 1.2 The LBG photometric selection criteria, in $(U_n - G, G - \mathcal{R})$ color space. The green and yellow regions indicate "strong" and "weak" Lyman breaks; the distinction is relevant to selection techniques in Chapter 4. The yellow points represent the stellar locus, based on the atlas of Gunn & Stryker (1983).

1.3 The medium-luminosity QSO survey

The LBG survey magnitude limit ($\mathcal{R} = 25.5$; $M_{1450} \approx -20$) is several magnitudes fainter than the other surveys mentioned in §1.1. In fact, when the notion of measuring the LF from these QSOs arose, it was realized that there would be a range of QSO luminosities whose statistics *still* would not be well constrained. The LBG data would place the first constraints on the very faint end of the LF, to about 6 mag fainter than $L_z(z = 3)$, and previous work already constrained the bright end $[L \gtrsim L_z(z = 3)]$. But in between, from perhaps $M_{1450} = -23$ to -25, it was not expected (based on the assumed shape of the LF) that the 0.38 deg^2 LBG data would contain enough QSOs to strongly constrain the LF.

This part of the LF, near the power-law break, is perhaps the most important. With a fairly flat faint-end slope, and steep bright-end slope, a great deal of the total luminosity comes from QSOs just to the faint side of the break. Since we are interested in the QSO contribution to the metagalactic UV radiation field, and QSOs' effect on the IGM, a good understanding of the integrated LF is essential.

It was therefore decided to conduct a QSO survey essentially identical to the LBG survey, but to shallower depth ($\mathcal{R} = 23$ instead of 25.5) and over a larger area (about 2 deg^2). The photometric criteria (Equations 1.3, 1.5–1.6) would be nearly the same, with some adjustments (borne of experience) to exclude stellar contaminants. Since the selection criteria were the same as the LBG survey, the new "medium luminosity" survey wasn't restricted to QSOs *per se*, but based on the magnitude distributions of QSOs, LBGs, and NL AGN from the LBG survey, QSOs were expected to strongly outnumber the other $z \approx 3$ objects.

It follows naturally from the photometric criteria that the u' imaging data must be substantially deeper than the g' or $\mathcal{R}$ data. Furthermore, reaching a certain magnitude in u' takes considerably longer than reaching the same magnitude in the other filters. Thus, the u' imaging would largely determine the amount of telescope time required to meet the goals stated above. Realizing that a considerable amount of time would be required, we sought a collaboration with A. Connolly, who had already obtained (for another project) sufficiently deep U imaging, in several large fields, using the KPNO Mosaic camera. Combining these data with new g' and $\mathcal{R}$ LFC imaging allowed the imaging portion of the survey to be completed relatively quickly and efficiently.

Following the imaging and photometric candidate selection, candidates were observed spectroscopically with the Double Spectrograph (Oke & Gunn 1982) on the Hale Telescope, in various low-resolution configurations. 13 QSOs at $z \approx 3$ were identified by their spectra (as was a single NL AGN), and were merged with the LBG survey QSOs to produce a well-characterized data sample offering good statistics over 6.5 mag in luminosity.

1.4   Results and conclusions from the QSO surveys

The primary result from these surveys was the first measurement of the faint end of the QSO LF at high redshift. A plot of the LF is shown in Figure 4.4 (page 53), along with data points from other surveys. The unexpected finding is that the faint-end slope is substantially flatter at $z \approx 3$ than in the local universe, $\beta_l = 1.20$, compared to 1.64. (The details of the fit are described in §3.4 and §4.3.3.) The integrated LF produces only 50% of the total luminosity predicted by earlier work (e.g., Pei 1995).

Scaling the results of Haardt & Madau (1996), this fit for the LF produces an H I photoionization rate of $\Gamma_{\mathrm{H\,I}} \approx 8.0 \times 10^{-13}$ s^{-1}, which can account for a metagalactic flux of $J_{912} \approx 2.4 \times 10^{-22}$ erg s^{-1} cm^{-2} Hz^{-1} sr^{-1}. The constraints on the ionizing flux from "proximity effect" analyses of the Lyα forest are uncertain, but are consistent with the integrated QSO value at $z \approx 3$ (e.g., Scott et al. 2002). In any case, the ratio of the total non-ionizing UV luminosity density of star forming galaxies relative to that of QSOs at $z \approx 3$ implies that QSOs must have a luminosity-weighted Lyman continuum escape fraction that is approximately 10 times higher than that of galaxies if they are to dominate the ionizing photon budget.

At shorter wavelengths, like those required to ionize He II, there is essentially no galactic contribution. Instead, QSOs are the primary source of radiation for the reionization of He II, which is known to occur at $z \approx 3$ (Jakobsen et al. 1994). As we discuss in detail in §4.4, the improved measurement of the faint end slope helps to explain several interesting aspects of He II Lyman-α forest observations, including the strong fluctuations in He II column density relative to H I (e.g., Shull et al. 2004).

The evolution of the QSO LF clearly has implications for the study of supermassive black hole (SMBH) growth, which is intricately tied to galaxy formation. It has long been predicted (e.g., Small & Blandford 1992), based on the LF shape and ignoring mergers,

that massive SMBHs form earlier than low-mass holes. This prediction is supported by recent observational evidence that even at very high redshifts, luminous QSOs have already formed massive SMBHs. For example, Vestergaard (2004) notes that in luminous $z \gtrsim 4$ QSOs, primarily from SDSS, central black holes of 10^9 M$_\odot$ are already present. The author also remarks that, based on their average spectrum (Figure 2.1), the QSOs discovered in the LBG survey have central black hole masses of $\gtrsim 10^8$ M$_\odot$. If the host galaxies of these QSOs are essentially LBGs, such large SMBH masses suggest that the black holes are fully-formed before the host galaxies.

Similarly, Wyithe & Loeb (2003) use the local SMBH mass function, in conjunction with a feedback model for SMBH accretion in QSOs, to predict the accretion histories of SMBHs. Their model predicts that the most massive SMBHs are in place by $z \approx 6$, in keeping with the observational results described above. In another paper (Wyithe & Loeb 2002), the authors present a physical model for the QSO LF evolution. This model predicts that the QSO phase is triggered by galaxy mergers, and that the duration of the Eddington accretion phase is determined by the mass ratio of small and final galaxies in the merger. Their model successfully predicts the observed bright-end slope of $\beta_h \approx 2.5$ at $z \gtrsim 4$ (Fan et al. 2001b), which is shallower than in the local universe.

Thus, it would appear that theory and observations are in general agreement concerning the most luminous QSOs and the most massive SMBHs. As Small & Blandford (1992) predicted, massive SMBHs appear to form quite early. But just as observations have been scarce regarding the faint end of the QSO LF, so has been the theoretical work. There have been few models or predictions about the faint end thus far. One of the few is again due to Wyithe & Loeb (2003), whose self-regulated growth model predicts a *steeper* faint-end slope at high redshift; combined with the evolution of the bright-end slope, they predict the "break" to disappear at high redshift. This result, of course, is contrary to the observations presented here, and is discussed in Chapter 4. Their prediction is also contrary to a result from the Great Observatories Origins Deep Survey (GOODS) team (Cristiani et al. 2004); as discussed in §4.4, they observe a deficiency of faint high-redshift QSOs, suggesting a flatter faint-end slope.

Granato et al. (2001) suggest that even though the most massive SMBHs grow rapidly and early, before their host galaxies, the situation is reversed for smaller holes. They propose that feedback from supernovae and accretion in smaller halos is capable of slowing down, and

halting, both the QSO activity and star formation, leading to a correlation between the BH and stellar masses. In this scenario, LBGs are generally in the pre-QSO phase, undergoing strong star formation before QSO feedback begins. Such a prediction is consistent with the observations described above, and also with the results of Hosokawa (2004), who concludes that most $z \approx 3$ LBGs do not have SMBHs, provided mass accretion is dominant process for SMBH growth. (If mergers and/or direct formation are important compared to accretion, the author cannot rule out SMBHs in most LBGs.)

The relationship between LBGs and QSOs at $z \approx 3$ merits further study. In Chapter 2, we calculate a typical QSO duty cycle of approximately 10^7 yr by noting the fraction of AGN compared to LBGs in the survey (3%) and the average duration of star forming activity in LBGs. This argument rests on the assumption that LBGs are the host galaxies of QSOs at the same redshift. If LBGs do not undergo a strong AGN phase until later (at $z \lesssim 2.7$), and the host galaxies of $z \approx 3$ QSOs are not LBGs at that time, this assumption does not hold. However, various other predictions for the QSO lifetime from other methods are in good agreement (e.g., Hosokawa 2002; Wyithe & Loeb 2002; Yu & Lu 2004; Grazian et al. 2004), and measurements of the cross-correlation between QSOs and LBGs at $z \approx 3$ (Chapter 2) suggest that both objects formed in similar halos, suggesting a similar evolutionary history between LBGs and QSO host galaxies.

The sample of QSOs and NL AGN from the LBG survey also provides an interesting comparison between UV- and X-ray selected samples. As discussed in §3.4, UV selection has done a very satisfactory job of identifying $z \approx 3$ AGN. Even those X-ray selected objects which do not meet the LBG photometric criteria (Equations 1.3–1.6) are generally just outside the selection window, and have optical spectra which are largely similar to the UV-selected objects. There is no evidence for a distinct, X-ray bright population at high redshift that is fundamentally different from the UV-selected AGN.

It is also worth noting that the LBG survey contained a NL AGN, "HDF–oMD49," which was well above the survey magnitude limit but not present in the 2 Ms *Chandra* Deep Field North (CDF–N) image at a level sufficient for inclusion in the main catalog (Alexander et al. 2003). The optical spectrum is shown in Figure 2.3. Because the CDF–N is the deepest X-ray image yet taken, we believe it is important to note that X-ray selection does not have a clear-cut advantage over deep optical imaging. Neither method can lay sole claim to the AGN population. It is not surprising that this is the case. Using the Green

et al. (1995) expression for the optical-to-X-ray slope, α_{ox}, we find that the expected soft X-ray flux of a $\mathcal{R} = 25$, $z = 3$ QSO is about $F_{0.5-2.0\ keV} \approx 2.7 \times 10^{-17}$ erg s^{-1} cm^{-2}, which is very similar to the on-axis sensitivity limit of the 2 Ms *Chandra* Deep Field (Alexander et al. 2003). There is considerable scatter in α_{ox}, so it is not unexpected that some of our faint AGN do not have sufficient X-ray flux to be detected by *Chandra*.

The results presented in this thesis substantially alter our understanding of AGN demographics at high redshift. We believe that the improved picture of the QSO LF will benefit researchers studying galaxy formation and SMBH growth, as well as the intergalactic medium at high redshift.

Chapter 2

AGN discovered in the $z = 3$ LBG survey

2.1 Introduction

Until very recently, virtually all surveys for QSOs and AGN at high redshift have been geared toward the detection of relatively "extreme" and rare objects, ranging from UV excess or color selection of QSOs (e.g., Fan et al. 2001b; Boyle et al. 2000; Warren et al. 1994) to the selection of objects by their extreme radio power (e.g., White et al. 2000; Dunlop & Peacock 1990; McCarthy 1993). These surveys have been quite successful because they make use of selection techniques that can be applied over large swaths of sky, and for which spectroscopic follow-up has proved straightforward and highly efficient due to the optical brightness of the sample. There are few constraints on broad-lined AGN drawn from the faint end of the UV/optical luminosity distribution [the faintest published survey is still that of Koo & Kron (1988), reaching the equivalent of $\mathcal{R} \approx 21$ at $z \approx 3$]; these fainter objects are expected to dominate the production of photons that, together with emission from young galaxies, maintain the ionization of the intergalactic medium at intermediate redshifts ($1 \lesssim z \lesssim 5$). Thanks to results from the *Chandra* X-Ray Observatory (Mushotzky et al. 2000; Barger et al. 2001; Alexander et al. 2001), we are just beginning to learn about the high redshift ($z > 2$) population of narrow-lined, obscured AGN of "type II". These objects can be quite unobtrusive at the optical (rest-UV) or radio wavelengths used by most AGN surveys in the

past. Despite their possible importance to the overall AGN demographics, only a handful have been identified to date (e.g., Stern et al. 2002; Norman et al. 2002).

At the same time, a very strong case has been developed in the local universe for a tight correlation between the properties of the stellar populations in bulges and spheroids and the mass of central black holes (e.g., Kormendy & Richstone 1995; Magorrian et al. 1998; Merritt & Ferrarese 2001). The presence of this correlation over a very wide range of mass scale strongly suggests that the formation of the spheroid stellar populations and the central black hole are causally linked. One might then reasonably expect that the era during which the spheroid stars were formed might also be that during which the black holes were most likely to be accreting material from gas-rich environs. The "quasar era" is now known to be rather strongly peaked near $z \approx 2.5$, declining rapidly at both higher and lower redshifts (e.g., Boyle et al. 2000; Warren et al. 1994; Schmidt et al. 1995; Kennefick et al. 1995; Fan et al. 2001b; Shaver et al. 1999). Since it is now possible to routinely observe star-forming galaxies near the peak of the "quasar era," there is the opportunity to assess the level of AGN activity that is ongoing as the galaxies are undergoing rapid star formation.

In this paper, we present some initial results on the AGN component of a moderately large spectroscopic survey for galaxies selected by their large unobscured star formation rates at redshifts $z \approx 3$. The survey should contain all but the most heavily obscured star forming galaxies at such redshifts (Adelberger & Steidel 2000), and as we detail below, is well-suited for detecting active accretion power in the same star forming objects because of the selection criteria used and the large number of spectra obtained. For the first time at high redshift, it may be possible to assess the fraction of rapidly star forming galaxies that are simultaneously playing host to significant accretion power. In any case, the survey has uncovered a relatively large number of UV-selected, relatively faint, broad-lined and narrow-lined AGN, whose properties we summarize.

We assume a cosmology with $\Omega_m = 0.3$, $\Omega_\Lambda = 0.7$, and $h = 0.7$ throughout this chapter.

2.2 The AGN sample

2.2.1 General Properties and Sample Definitions

The full LBG survey consists of 16 independent fields covering a total of 0.38 deg^2. The effective volume covered by a color-selected survey depends in a relatively complex way on

the color, magnitude, and redshift of objects in the targeted sample (Steidel et al. 1999; Adelberger 2002). Some of the details of the LBG selection function are presented in Steidel et al. (1999); the AGN described in this paper satisfied precisely the same photometric criteria as the star forming galaxies in the sample. The complete details of the LBG photometric and spectroscopic survey are presented by Steidel et al. (2003); here we concentrate on the small sub-sample for which there is spectroscopic evidence for the presence of AGN.

At redshifts $z \approx 3$, the distinctive colors of Lyman break objects depend largely on properties of the intervening intergalactic medium (IGM) where the mean free path of photons shortward of 912 Å in the rest frame is short, resulting in a pronounced drop in flux in the observed U_n band even for objects whose spectra do not have intrinsic breaks at the Lyman limit (e.g., Madau 1995; Steidel & Hamilton 1993). Because objects in the spectroscopic sample were selected without regard to morphology (i.e., no attempt was made to remove point sources from the catalog), we expect that our spectroscopic sample should be at least as complete for objects dominated by non-stellar emission as compared to normal star forming galaxies.

The complete catalog of LBG candidates in the $z \approx 3$ survey fields consists of 2440 objects in the apparent magnitude range $19.0 \leq \mathcal{R} \leq 25.5$. Simulations suggest that only about 50% of objects with LBG-like intrinsic colors at $z \approx 3 \pm 0.3$ will be included in our color-selected photometric catalogs due to various sources of incompleteness (Steidel et al. 1999). While we attempted to obtain uniform data in each field, variations in Galactic extinction, seeing, sky brightness, and integration time would require each field to be treated independently in a proper evaluation of completeness. Over the full survey, we spectroscopically observed a total of 1344 objects (55% of the photometric sample), of which 51 are identified as Galactic stars, 988 are high redshift objects with $\langle z \rangle = 2.99 \pm 0.29$, and 306 remain unidentified. We classified an object as a broad-lined AGN if its spectrum contained any emission line with FWHM greater than 2000 km s^{-1}. Such objects always contained several broad emission lines, usually at least Lyman-α+N v, Si iv λ1397, C iv λ1549, and C iii] λ1909. Of the 13 broad-lined AGN identified, two show evidence for "associated" broad absorption lines of high ionization species such as O vi, N v, Si iv, and C iv. Objects were classified as narrow-lined AGN if their strong Lyman-α emission was accompanied by significant emission in C iv λ1549 and if no emission line had FWHM greater than 2000 km s^{-1}. These objects usually had He ii λ1640 and C iii] λ1909, and

often detectable N v λ1340 and O vi λ1034. Given the quality of the typical LBG survey spectrum, the narrow C iv emission line would have to exceed equivalent widths of a few angstroms in the rest frame, or line fluxes of $\sim 2 \times 10^{-17}$ erg s^{-1} cm^{-2}, to have been recognized. The coarse properties of the two AGN samples are summarized in Table 2.1.

The composite spectra of both classes of AGN, formed by shifting each spectrum into the rest frame based on the emission line redshift, normalizing by the median continuum level in the rest-frame 1600–1800 Å range, and averaging, are shown in Figure 2.1. The top panel of Figure 2.1 also shows for comparison the composite spectrum of much brighter QSOs [typically $V \sim 18$, from Sargent et al. (1989) and Stengler-Larrea et al. (1995)] that would satisfy the same LBG color selection criteria. We note the striking similarity of the two QSO samples, which are separated by a factor of about 100 in UV luminosity. There is clear evidence for the Baldwin (1977) effect in the increasing strength of the C iv emission line with decreasing continuum luminosity, and the faint QSO composite has a much more prominent narrow He ii λ1640 emission line.

Our definition of a narrow-lined AGN, based on the detected presence of high ionization emission lines, is admittedly somewhat arbitrary; however, it relies on the fact that the vast majority of LBGs show no detectable emission in C iv and He ii even when Lyman-α emission is strong, and that it is difficult to produce significant nebular lines of these high ionization species without the hard ionizing spectrum of an AGN component. The line ratios observed among the objects identified as narrow-lined AGN are quite similar to those of local Seyfert 2 galaxies—in fact, for the composite spectrum shown in the bottom panel of Figure 2.1, the Lyα/C iv and Lyα/C iii] ratio are essentially identical to a composite Seyfert 2 spectrum presented by Ferland & Osterbrock (1986). The composite narrow-lined AGN spectrum is also strikingly similar, in both continuum and emission line properties, to the composite spectrum of high redshift radio galaxies from Stern et al. (1999).

A separate, but related, issue is how the narrow-lined, UV-selected AGN fit in with the so-called "type II" QSOs discovered recently in deep *Chandra* images. The optical spectra of faint X-ray sources detected with *Chandra* are quite diverse, ranging from broad-lined AGN to objects without clear UV/optical indicators of the presence of AGN (e.g., Barger et al. 2001; Hornschemeier et al. 2001; Mushotzky et al. 2000, and references therein). However, for the relatively small number of published spectra of identified *Chandra* sources at $z > 2$, every one would have satisfied either our "broad-lined" or "narrow-lined" AGN criteria.

In particular, the spectra of the 2 published "type II" QSOs at high redshift (Stern et al. 2002; Norman et al. 2002) both resemble our faint optically selected narrow-lined AGN spectra in their UV emission line properties. As discussed below, at present there is only limited information on the X-ray emission from objects in the optically selected samples. Clearly, optical/UV selection of AGN will impose different selection criteria than X-ray selection, and there may well be strong X-ray emitting AGN at $z > 2$ that would either not be detected at all in the rest-UV, or not be recognizable as AGN from their UV spectra, because of heavy obscuration. Similarly, because of greater absolute sensitivity in the UV and widely varying UV/X-ray flux ratios (for whatever reason), it may be that faint AGN selection in the UV can identify objects whose X-ray fluxes are still beyond the deepest *Chandra* integrations. We discuss this issue further in §2.3.

2.2.2   Estimates of internal completeness of the AGN sub-sample

While a more detailed analysis of the AGN selection function and a derivation of the UV luminosity function of faint AGN are deferred to Chapter 3, here we make some approximate statements on the completeness of our spectroscopic AGN sample. When we could not determine a redshift from a spectrum we had obtained, it was usually due to an absence of emission lines and inadequate continuum signal to measure the relatively weak absorption lines which help establish redshifts for a large fraction of our galaxy sample. Since every AGN in our sample has several strong emission lines (including strong Lyman-α emission), it is unlikely that an AGN with UV-detectable features in the target redshift range would not have been recognized even in spectra of much lower than average quality. We can estimate an upper limit on the number of unrecognized narrow-lined AGN (for reasons of inadequate S/N in the spectra) among those objects identified as normal star-forming galaxies by examining high S/N composite spectra of the LBGs (with identified AGN excluded). The average intensity of C IV emission in the narrow-lined AGN sample is about 20% that of Lyman-α (see Figure 2.1). If we assume that this ratio is characteristic of narrow-lined AGN that we failed to flag as such, and we use the fact that the intensity ratio of Lyman-α to C IV emission in the spectral composite of non-AGN LBGs is $\gtrsim 100$ for the quartile of the LBG sample having the strongest Lyman-α emission strength[1], then an upper limit on the

---

[1]This is the only sub-sample of the LBGs that has a mean Lyman-α equivalent width close to that of the AGN.

fraction of AGN-like spectra to have contributed to that sub-sample is $\sim 5/100 = 5\%$. The corresponding limit on the fractional contribution of unrecognized AGN to the full LBG sample would then be $\sim 0.25 \times 5 \simeq 1\%$. The true fraction with unrecognized AGN-like spectra is likely to be smaller than this limit, since in most individual spectra we could have recognized C IV emission at the level seen in the composite AGN spectrum, and because low-level C IV emission (part of which is due to the stellar P-cygni feature) is expected in the rapidly star forming galaxies even without AGN excitation.

Thus, we expect that, with respect to the photometric LBG sample, the spectroscopic AGN sample is close to $N_{\mathrm{obs,spec}}/N_{\mathrm{phot}} = 1344/2440 \sim 55\%$ complete, i.e., that any AGN in the LBG photometric sample that was attempted spectroscopically would have yielded a redshift. We estimate that our present spectroscopic AGN sample contains only $\sim 30\%$ of the AGN in our fields with $2.7 \lesssim z \lesssim 3.3$ and satisfying our photometric criteria $\mathcal{R} \leq 25.5$, $G - \mathcal{R} < 1.2$, and $U_n - G > (G - \mathcal{R}) + 1$ (i.e., the spectroscopic completeness of 0.55 times the estimated photometric completeness of $\sim 50\%$). The mean redshift of the narrow-lined AGN in our sample is somewhat different from that of the galaxies, probably due to a combination of the subtleties of how the emission lines have affected the broad-band photometry and the redder continuum color (see below). The broad-lined AGN completeness within the photometric sample is expected to be smaller than that of galaxies at a given redshift and apparent magnitude because, at $z \approx 3$, only about 60% of (bright) QSO spectra have intervening optically thick Lyman limit systems at high enough redshift to produce the distinctive UV color that we depend on to identify them (Sargent et al. 1989). Galaxies do not suffer this form of incompleteness because they are expected to have significant intrinsic Lyman limits from a combination of stellar spectral energy distributions and opacity to their own Lyman continuum radiation from the interstellar medium[2]. Again, a careful treatment of these effects is deferred to Chapter 3, but this additional source of incompleteness for broad-lined AGN is likely to be of roughly the same order as the spectroscopic advantage which AGN enjoy when they are observed.

With these caveats in mind, a reasonable estimate of the fraction of AGN among objects in our LBG sample is approximately the same as the fraction of AGN within the spectroscop-

---

[2]We cannot rule out the possibility that faint broad-lined AGN are subject to increased internal Lyman continuum opacity compared to the bright QSOs that have been studied to date; however, the absence of detectable interstellar absorption lines in the composite broad-lined QSO spectrum does suggest that the typical H I column density within the host galaxies along our line of sight is significantly smaller than that for typical LBGs.

ically confirmed sample: 29/988, or $\sim 3\%$. This number would increase to $\sim 4\%$ allowing for the maximal incompleteness of the narrow-lined sample discussed above. The observed ratio of narrow-lined to broad-lined AGN, $N(\mathrm{NL})/N(\mathrm{BL}) = 1.2 \pm 0.4$, is consistent with the ratio of broad-lined and narrow-lined radio-loud AGN found by Willott et al. (2001), although we emphasize that our numbers are not yet corrected for relative incompleteness.

2.3 X-ray properties of optically faint AGN at $z \sim 3$

At present, there is only a small amount of information on the X-ray properties of the optically faint AGN in our sample. A cross-correlation of our LBG survey with the 1 Ms exposure of the *Chandra* Deep Field North (the HDF North region) yields X-ray detections for 4 of the 148 candidates[3] ($\sim 3\%$) in an $8.7' \times 8.7'$ field centered on the deep HST pointing (Nandra et al. 2002). Of these, two have not yet been observed spectroscopically. The other two are a faint broad-lined AGN with $\mathcal{R} = 24.15$ and $z = 3.406$ (HDF–oC34=J123633.4+621418), and a narrow-lined AGN with $\mathcal{R} = 24.84$ and $z = 2.643$ (HDF-MMD12=J123719.9+620955). Both of these AGN have rest-frame 2–10 keV luminosities (uncorrected for intrinsic absorption) of $\sim 5 \times 10^{43}$ erg s^{-1}. Our spectroscopic Lyman break galaxy sample also contains a clear narrow-lined AGN spectrum, shown in Figure 2.2, that is undetected in the deep *Chandra* image and thus has an unobscured X-ray luminosity of $\lesssim 5 \times 10^{42}$ erg s^{-1} in the 2–10 keV band. Thus, while we expect that a large fraction of the optically faint AGN in our sample would be detected in the deepest *Chandra* exposures, there is likely also to be a sub-sample that is relatively X-ray faint that would not be detected in even the deepest X-ray pointings to date. Given the overall completeness estimate of $\sim 30\%$ discussed above, we expect ~ 20 optically faint ($21 \lesssim \mathcal{R} \lesssim 25.5$) AGN (of which ~ 11 would be broad-lined objects) over a redshift interval of $\Delta z \simeq 0.6$ near $z = 3$ per $17'$ by $17'$ *Chandra* ACIS field[4]. Ostensibly this number is significantly larger than the number of AGN (in a similar redshift range) identified with *Chandra* sources in the deep fields (e.g., Barger et al. 2001; Hornschemeier et al. 2001; Barger et al. 2001; Stern et al. 2002) although the numbers are small and the follow-up of optically faint *Chandra* sources is still underway. More complete surveys of both *Chandra* sources and faint optically-selected

---

[3]None of these objects is detected in the radio continuum with the VLA (Nandra et al. 2002)

[4]The number 20 is just $29/(0.3*0.38) \simeq 250$ AGN per square degree. We note, however, that the region in which 4 LBGs were directly detected with *Chandra* was only $\sim 25\%$ of the full *Chandra* field of view.

AGN in the same fields will significantly improve our understanding of the overall AGN demographics at high redshift.

2.4 Are LBGs the hosts of the optically faint AGN?

It would be interesting in the context of understanding the history and efficiency of accretion-powered luminosity in galaxies if one could verify that the AGN in the sample are hosted by the equivalent of LBGs[5]. The range of continuum apparent magnitudes (i.e., the lack of objects brighter than $\mathcal{R} \approx 23$) of the narrow-lined AGN in the spectroscopic sample is similar to that of the non-AGN LBGs in the sample (Table 2.1). The strength of the few interstellar absorption lines that are not strongly masked by emission lines in the composite narrow-lined AGN spectrum are quite similar to those of a composite spectrum of non-AGN LBGs with Lyman-α seen in emission (see Figure 2.3). Unfortunately, the strongest stellar feature in the spectra of LBGs is the C IV P-Cygni profile, which is badly affected by C IV emission in the composite narrow-lined AGN spectrum. We cannot say with certainty whether the continuum light of the narrow-lined AGN is produced by stellar or non-stellar emission—making this distinction is notoriously difficult even for nearby Seyfert galaxies (e.g., Gonzalez Delgado et al. 1998). However, the far-UV continuum slope ($\beta = -0.4$, where $f_\lambda \propto \lambda^\beta$) of the composite narrow-lined AGN is redder than all but $\sim 10\%$ of the LBG sample, and is much redder than the subsample of LBGs with similarly strong Lyman-α emission, as illustrated in Figure 2.3. If the continuum were attributed to starlight in the same manner as other LBGs then the implied extinction would be a factor of ~ 50 (Adelberger & Steidel 2000). At this time, only one of the narrow-lined AGN has been observed in the K band, HDF–oMD49 (see Figure 2.2). This object has $\mathcal{R} - K = 4.20$, making it the third-reddest LBG in the observed sample of 118 (Shapley et al. 2001).

The brightest broad-lined object in the sample is more than 2 magnitudes brighter than the brightest narrow-lined object, and there are 5 broad-lined AGN brighter than the brightest narrow-lined AGN. There is some evidence for a flatter magnitude distribution for the broad-lined AGN than for the narrow-lined AGN, but small number statistics and numerous possible selection effects prevent us from making too much of this trend at this time. The relative absence of very UV-bright narrow-lined AGN is at least qualitatively

---

[5]Analysis of HST images of the host galaxies of a small sample of $z \sim 2$ radio quiet QSOs by Ridgway et al. (2001) indicates that the hosts are consistent with the luminosities and morphologies of LBGs.

consistent with the possibility that much of the AGN-produced UV continuum is obscured. There is considerable overlap between our survey fields and planned deep surveys with the *Spitzer Space Telescope* (SST), so that it should soon be possible to measure many of these optically selected AGN at mid-IR wavelengths, where any bolometrically luminous obscured AGN are expected to be quite prominent.

Assuming that the broad-lined AGN are the less-obscured versions of similar AGN activity, let us suppose for the sake of argument that the mass of putative LBG black holes scales with stellar bulge mass according to the relation established locally, $M_{\rm BH} \approx 2 \times 10^{-3} \, M_{\rm bulge}$ (e.g., Ho 1999). Adopting the range of inferred stellar masses of LBGs in our survey from Shapley et al. (2001), we expect typical black hole masses of $3 \times 10^7 \, {\rm M}_\odot$ and a range from 2×10^6 to perhaps $2 \times 10^8 \, {\rm M}_\odot$. If these black holes were radiating at the Eddington limit, they would be expected to have observed[6] $20.0 \lesssim \mathcal{R} \lesssim 24.7$, close to the observed range (for the broad-lined AGN) of $20.6 \lesssim \mathcal{R} \lesssim 24.8$. Apparently, LBGs would be capable of hosting broad-lined AGN with the range of observed UV luminosities.

A more quantitative test of whether the AGN and the LBGs share the same host dark matter halos comes from an evaluation of the clustering statistics of the AGN with respect to LBGs. We have performed tests, using methods similar to those outlined by Adelberger (2002), of the density of LBGs around AGN as compared to that of other (non-AGN) LBGs. Evaluated on scales $\delta z = 0.0085$ and $\delta \theta = 200$ arcmin, we find that the density of LBGs in the vicinity of narrow-lined AGN is 0.96 ± 0.24 times the density of LBGs around other LBGs. The density of LBGs around broad-lined AGN is 1.58 ± 0.33 times higher than the density of LBGs around other LBGs. These crude tests suggest that the narrow-lined AGN cluster very similarly to non-AGN LBGs, and that broad-lined AGN may be more strongly clustered than typical LBGs.

In any case, it seems plausible that the observed AGN may be hosted by the equivalent of LBGs. If this is indeed the case, the fraction of LBGs in which obvious AGN activity is present may provide a rough timescale for near-Eddington accretion rates onto central black holes, as follows. The characteristic timescale for star formation episodes in LBGs is estimated to be ~ 300 Myr, inferred from the modeling of the far-UV to optical (rest-frame) colors (Shapley et al. 2001; Papovich et al. 2001). If the 3% AGN activity reflects

---

[6]Here we assume a radiative efficiency of $\epsilon \sim 0.1$ for the accretion and that $\nu L_\nu(UV)$ is a reasonable approximation to the bolometric luminosity.

the duty cycle of significant black hole accretion in LBGs, it would imply an active accretion timescale of $\sim 10^7$ years, broadly consistent with the expected black hole masses given the implied Eddington mass accretion rate of ~ 1 M$_\odot$ yr^{-1}. AGN lifetimes of this order have been inferred from theoretical studies of black hole growth based on mergers in hierarchical models of structure formation (e.g., Kauffmann & Haehnelt 2000) and from consideration of the QSO luminosity functions and the distribution of black hole masses in the local universe (e.g., Haehnelt et al. 1998; Yu & Tremaine 2002). Significantly longer accretion timescales of ~ 500 Myr have been suggested by Barger et al. (2001) based on the observation that $\sim 4\%$ of "$L_\star$ galaxies at all redshifts" are X-ray sources, but such timescales may refer to a very different, more protracted process of sub-Eddington accretion onto black holes in well-formed galaxies primarily at $z < 1$.

2.5 Discussion

While we defer more quantitative statements to a future chapter, there are several statements we can make that are unlikely to change after more careful modeling of incompleteness. First, narrow-lined AGN that are identifiable optically using LBG color selection criteria are quite common, with a space density (at $z \approx 3$) 50 to 100 times larger than that of the spectroscopically similar high redshift radio galaxies (cf. Willott et al. 2001). The implied surface density of AGN per square degree per unit redshift at $z \approx 3$ reaches approximately 400. It is still uncertain, due to small number statistics and incomplete surveys, what fraction of this number would also be *Chandra* sources that may contribute significantly to the X-ray background[7]. Nevertheless, we can say with some confidence that narrow-lined AGN make a negligible contribution to the $z \approx 3$ UV background: the total 1500 Å luminosity of narrow-lined AGN in our sample is only $\sim 20\%$ that contributed by the broad-lined AGN, and less than about 2% of that contributed by non-AGN LBGs. We do not know the narrow-lined AGN contribution to the *ionizing* UV background, but it is likely to be far smaller than 20% of the broad-lined AGN background judging by the red continuum colors and the expectation that the objects are fairly heavily obscured.

Using currently accepted parameterizations of the $z \approx 3$ QSO luminosity function (Pei 1995), about 75% of the AGN-produced ionizing radiation field would come from QSOs

---

[7]About half of the narrow-lined AGN in our sample would be classified as "optically faint," defined by Alexander et al. (2001) to be objects with $I > 24$, or $I_{AB} \gtrsim 24.5$.

Table 2.1. Properties of the AGN among the $z \approx 3$ LBG sample

	Broad-lined	Narrow-lined	LBGs[a]
Number	13	16	959
$\langle z \rangle \pm \sigma_z$	3.03 ± 0.35	2.67 ± 0.35	2.99 ± 0.30
$\langle \mathcal{R} \rangle$[b]	23.3	24.4	24.6
$\mathcal{R}$ Range	$20.6 - 24.8$	$22.6 - 25.4$	$22.8 - 25.5$

[a]Excluding objects identified as AGN.

[b]Mean AB magnitude at an effective wavelength of 6830 Å or $\simeq$ 1700 Å in the rest frame at $z \simeq 3$.

that have apparent magnitudes in the range $20 \lesssim \mathcal{R} \lesssim 25.5$, and only about 7% comes from brighter QSOs. Thus, while our sample of broad-lined AGN is fairly small, it extends far deeper than existing QSO surveys[8], allowing for the first time a direct measurement of the AGN contribution to the ionizing radiation field at high redshift. While it is possible that star formation in LBGs may dominate the production of Lyman continuum photons at $z \approx 3$ (Steidel et al. 2001), broad-lined AGN such as those in our faint sample almost certainly provide a substantial fraction of the higher energy photons which apparently reionized He II near $z \approx 3$. An accurate measurement of the AGN ionizing photon production requires careful attention to issues of photometric and spectroscopic completeness, which will be presented in Chapter 3.

---

[8]The faintest broad-lined AGN in our sample are considerably fainter than the traditional dividing line between QSOs and Seyfert 1 nuclei of $M_B = -23$. This absolute magnitude, for the adopted cosmology, corresponds to $\mathcal{R} \simeq 23$.
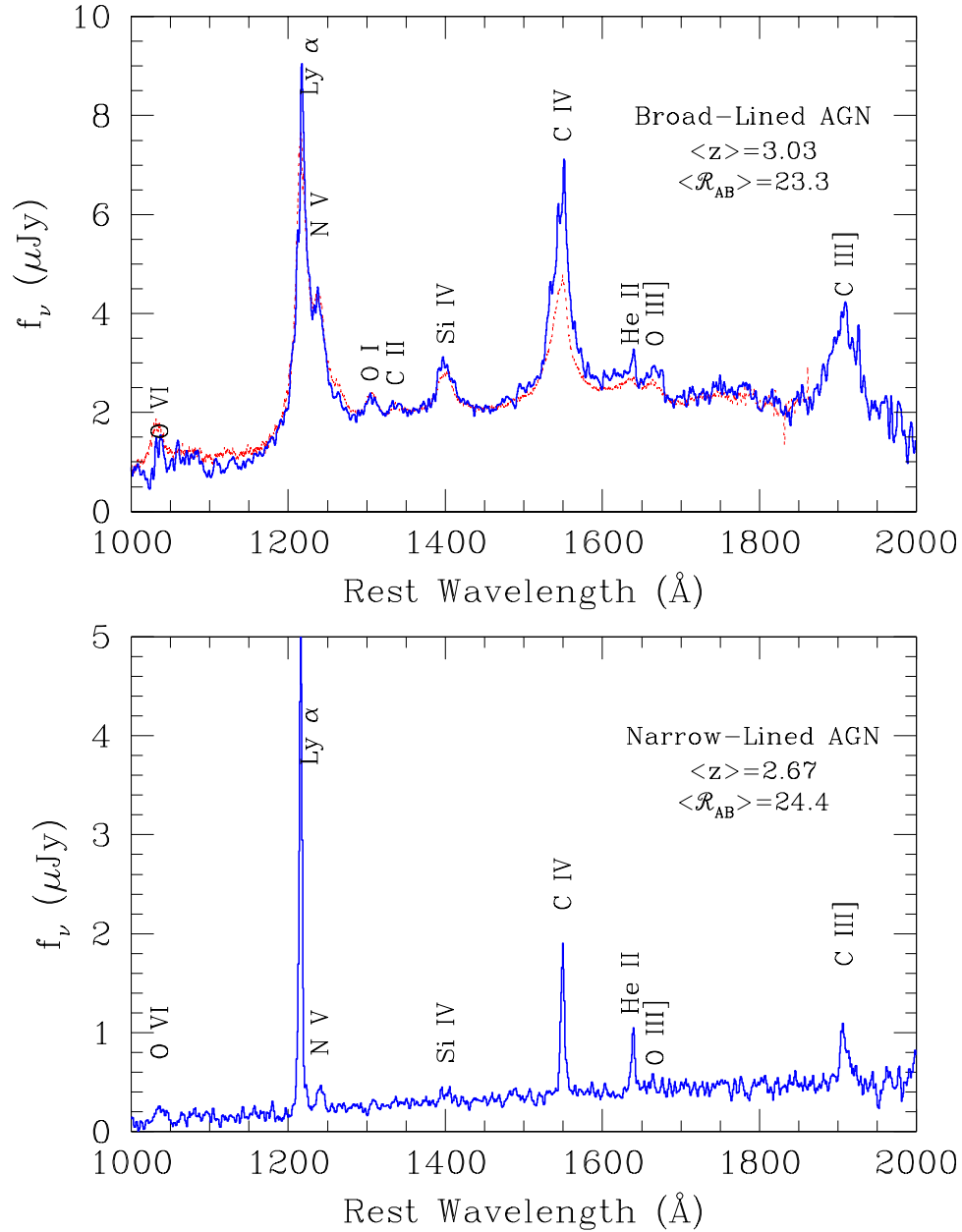
Figure 2.1 a) The composite spectra of the 13 "type I" AGN (blue). Superposed in red is the (scaled) composite spectrum formed from a sample of QSOs that is 100 times brighter on average (Sargent et al. 1989; Stengler-Larrea et al. 1995). b) The composite spectrum formed from the 16 "type II" AGN (blue) in the LBG spectroscopic sample.
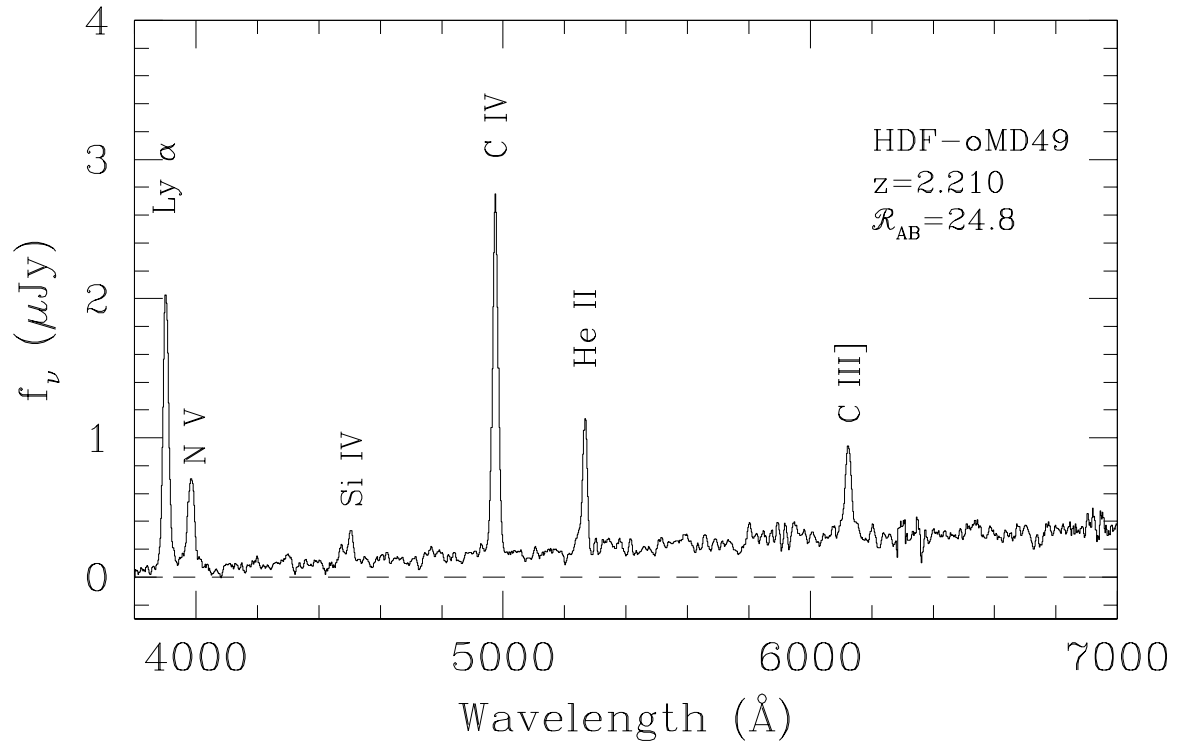
Figure 2.2 The observed spectrum of HDF–oMD49, a type II AGN that is undetected in the 1 Ms *Chandra* Deep Field North X-ray image. This object has an unusually weak Lyman-α emission line with respect to the high ionization N V and C IV lines, possibly indicating a large amount of extinction in the narrow line region.
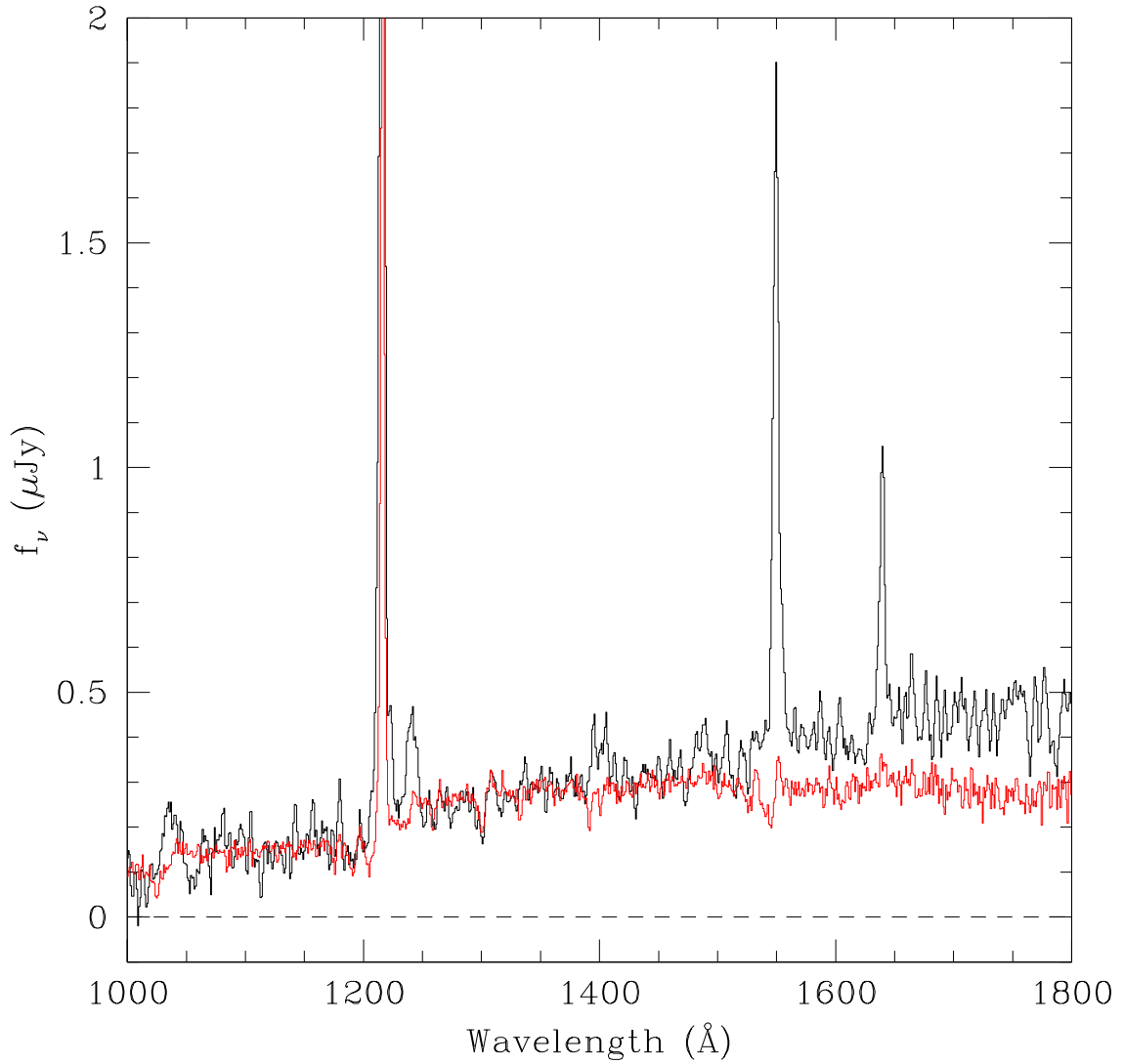
Figure 2.3 Comparison of the continua of the composite (non-AGN) LBG spectra culled from the subset with strong Lyman-α emission (red; Shapley et al. 2003) compared to that of the identified type II AGN (black). Note that the AGN spectrum has much stronger emission lines and is considerably redder in the continuum. Note the similarity of the strength of the interstellar O I+Si II feature near 1303 Å.

Chapter 3

Luminosity function from the $z = 3$ LBG survey

This chapter is essentially identical to a paper published in the *Astrophysical Journal*, 605, 625. © 2004. The American Astronomical Society. All rights reserved.

3.1 Introduction

The QSO luminosity function (LF) at high redshifts provides important constraints on the ionizing UV radiation field of the early universe. Until now, however, the faint end of the QSO LF has not been measured at high redshift. Instead, low-redshift measurements of the faint end were combined with high-redshift measurements of the bright end to estimate the entire LF at high redshift. Various models of LF evolution have been proposed; for example, a model proposed by Pei (1995) consists of a double power-law (Boyle et al. 1988) whose bright- and faint-end slopes are independent of redshift, and whose power-law break $L_z(z)$ comes at a luminosity which is proportional to a Gaussian in z, with a maximum near $z_\star = 2.75$ and $\sigma = 0.93$ redshift. This model is representative of "pure luminosity evolution" models, as the overall normalization and the power-law slopes are independent of redshift. While pure luminosity evolution has been shown to work well at $z < 2.3$ (Boyle et al. 1988, 2000), there is now evidence that it is insufficient at high redshift; for example, SDSS results demonstrate that the bright-end slope is flatter at $z > 3.6$ than in the local universe (Fan et al. 2001b). The luminosity of the power-law break and the faint-end slope have not been measured at high redshifts prior to the survey presented here.

　　We have made the first direct measurement of the faint end of the QSO LF at high

redshift, using a sample of 11 faint $z \sim 3$ QSOs discovered in a survey for Lyman break galaxies. Figure 3.1 illustrates the depth of this survey relative to previous $z = 3$ QSO surveys and demonstrates that the vast majority of the total QSO UV luminosity arises from QSOs bright enough to be included in this survey.

Throughout this paper, the term "QSO" is used to describe all broad-lined AGN without imposing the traditional $M_B < -23$ luminosity cutoff. Spectral properties of such objects are essentially the same across at least two decades of luminosity (Chapter 2), thus we find no reason to impose such a cutoff. In Section 3.2, we will present an overview of the survey parameters and photometric criteria for candidate selection. In Section 3.3, we will describe our measurements of photometric and spectroscopic completeness, and our calculation of the survey effective volume. The QSO luminosity function will be presented in Section 3.4, followed by a discussion of its implications for the UV radiation field in Section 3.5.

3.2   Survey information

The Lyman break technique has proved to be a successful and efficient means of photometrically identifying star-forming galaxies and AGN at $z = 3$ (Steidel et al. 2003). Similar multicolor approaches have been used in previous, shallower surveys for high-redshift QSOs with good success (e.g. Koo et al. 1986; Warren et al. 1991; Kennefick et al. 1995). Survey fields were imaged in U_n (effective wavelength 3550 Å), G (4730 Å), and $\mathcal{R}$ (6830 Å) filters (Steidel & Hamilton 1993). A star-forming galaxy at $z = 3$ will have a Lyman break in its SED that falls between the U_n and G filters, resulting in a $U_n - G$ color that is substantially redder than its $G - \mathcal{R}$ color. Objects meeting the following photometric criteria were selected as candidate $z = 3$ galaxies:

$$\mathcal{R} > 19 \tag{3.1}$$

$$\mathcal{R} < 25.5 \tag{3.2}$$

$$G - \mathcal{R} < 1.2 \tag{3.3}$$

$$G - \mathcal{R} + 1.0 < U_n - G \tag{3.4}$$

At $z = 3$, the intergalactic medium provides sufficient opacity to also select many QSOs with this technique even if their intrinsic SED lacks a strong Lyman break. The details are

Table 3.1.   The mean and sigma of the Gaussian distributions used for simulating the colors of QSOs (see section 3.3.1). The C IV equivalent width was scaled in proportion to that of Lyα+N V in order to maintain the template's original line ratio.

Parameter	Mean	Sigma
Continuum slope (F_ν)	0.46	0.30
EW(Lyα+N V) (Å)	80.0	20.0

addressed in Section 3.3.

The LBG survey fields used for this study cover 0.43 deg^2 in 17 fields, which are discussed in detail in Chapter 2). A composite spectrum and other information relating to the 13 QSOs discovered in the survey also appear in Chapter 2. Two of these QSOs satisfied earlier versions of the photometric criteria, but do not satisfy the final versions listed above, and have been excluded from this paper's results. The sample discussed in this paper, therefore, comprises 11 QSOs.

3.3   Sensitivity to QSOs

3.3.1   Photometric completeness

The intrinsic $U_n - G$ and $G - \mathcal{R}$ colors of QSOs depend primarily on the spectral index of their continuum and their Lyman-α+N V equivalent width. To measure the distribution of intrinsic colors (i.e., without the effects of measurement error), we produced a template QSO spectrum consisting of 59 QSOs studied by Sargent et al. (1989, hereafter SSB). These QSOs were discovered using objective prism techniques and are not expected to have significant selection biases in common with multicolor selection techniques. The SSB QSOs are about 100 times brighter than LBG survey QSOs, but a comparison of the SSB and LBG composite spectra suggests that the two populations are sufficiently similar that using the SSB composite as a template is satisfactory (Chapter 2). An average intergalactic absorption spectrum was used to absorption-correct the template using the model of Madau (1995), and portions of the spectrum having poor signal-to-noise were replaced with a power-law fit to the continuum.

The template spectrum was repeatedly altered to have continuum slopes and Lyman-α

equivalent widths drawn from the Gaussian distributions described in Table 3.1, a compromise between the results of Vanden Berk et al. (2001), Fan et al. (2001a), and our SSB template. Each altered spectrum was redshifted to 40 redshifts spanning $z = 2.0$ to $z = 4.0$. Intergalactic absorption was added by simulating a random line-of-sight to each QSO with absorbers distributed according to the MC-NH model of Bershady et al. (1999). (For comparison, an average intergalactic extinction curve (Madau 1995) was also employed. The results were not significantly different.) The spectrum was then multiplied by our filter passbands to produce a distribution of intrinsic colors which reflects the QSO population.

These colors were used to place artificial QSOs into the survey images. 5000 QSOs drawn uniformly from the redshift interval $2.0 < z < 4.0$ and apparent magnitude interval $18.5 < \mathcal{R} < 26$ were simulated in each of the 17 survey fields. The apparent magnitude interval is 0.5 magnitudes larger than the selection window on each end, in order to allow measurement errors to scatter objects into the selection window. The artificial QSOs added to an image were given radial profiles matching the PSF of that image (i.e., they were assumed to be point sources). This assumption has little practical effect, because even galaxies are barely resolved at $z = 3$, and no morphological criteria were applied to candidates during the LBG survey. The images were processed using the same modified FOCAS (Jarvis & Tyson 1981) software which was used for the actual candidate selection, and the observed colors of the simulated objects were recorded. The intrinsic QSO color distribution was thus transformed to an observed color distribution. Figure 3.2 shows the fraction of simulated QSOs that meet the photometric selection criteria as a function of redshift. As a consistency check, the curve shown was multiplied by $\int \Phi(L, z) \, dL$ to reflect the underlying redshift distribution of QSOs, and compared to the distribution of QSOs discovered in this survey, using a Kolmogorov-Smirnov test. The result was $P = 0.49$ using the Pei (1995) LF, and $P = 0.45$ using the LF shape measured in Section 3.4, indicating consistency between the expected and actual distribution of QSO redshifts.

3.3.2 Spectroscopic completeness

With the observed color distribution, we can measure the fraction of QSOs which meet the LBG color criteria as a function of absolute magnitude and redshift. In order to determine the effective volume of the survey, it is also necessary to know the probability of a photometric candidate being observed spectroscopically. At faint apparent magnitudes

($\mathcal{R} > 23$), there were 2,289 candidates in the 17 fields, enough to measure the spectroscopic observation probability as a function of ($\mathcal{R}$, $G - \mathcal{R}$). The photometric candidates were divided into bins in ($\mathcal{R}$, $G - \mathcal{R}$) parameter space, using an adaptive bin size which increases resolution where the parameter space is densely filled with candidates. The probability of spectroscopic observation was measured for each bin.

At $\mathcal{R} < 23$, there are too few photometric candidates to obtain an accurate measurement of the selection probability. However, at these apparent magnitudes, candidates with relatively blue $G - \mathcal{R}$ were likely to be QSOs and hence were nearly always observed spectroscopically. Candidates with red $G - \mathcal{R}$ were likely to be stellar contaminants, and were less likely to be observed. Hence we have estimated the probability of spectroscopic observation to be unity for candidates with observed magnitudes $\mathcal{R} < 23$ and $G - \mathcal{R} < 1$, and 0.5 for candidates with $\mathcal{R} < 23$ and $G - \mathcal{R} > 1$. The results are insensitive to the latter value because the colors of QSOs are rarely observed to be so red.

We assume that any spectroscopically observed QSO will be identified as such and a redshift obtained, since our spectroscopic integration times were chosen so that we could often identify faint LBGs using their absorption lines (typically 90 minutes using Keck–LRIS). Because QSOs have strong, distinctive emission lines they are easily identifiable even at the faintest apparent magnitudes in the survey ($\mathcal{R} = 25.5$).

3.3.3 Effective volume of the survey

For comparison with other work, e.g., SDSS, we wish to measure the QSO luminosity function with respect to 1450 Å rest frame AB absolute magnitude (M_{1450}). At any given redshift in this study, we estimated an object's apparent magnitude m_{1450} as a linear combination of its $\mathcal{R}$ and G magnitudes. A small redshift-dependent correction, derived from our simulations of QSO colors, was then made to the value. This correction, typically of order 0.25 mag, accounts for Ly-α emission in G, Ly-α forest absorption, and similar effects. If we denote by $f_{\text{phot}}(m_{1450}, z)$ the probability that a QSO of apparent 1450 Å rest frame AB magnitude m_{1450} and redshift z will have observed colors and magnitudes that meet the selection criteria for LBGs, and we denote by $f_{\text{spec}}(m_{1450}, z)$ the fraction of such candidates that will be observed spectroscopically, we can measure the effective volume of the survey

as a function of absolute magnitude,

$$V_{\text{eff}}(M) = \int_\Omega \int_{z=0}^{z=\infty} f_{\text{phot}}(m_{1450}(M,z),z) \ f_{\text{spec}}(m_{1450}(M,z),z) \ \frac{dV}{dz \ d\Omega} \ dz \ d\Omega \qquad (3.5)$$

where $m_{1450}(M_{1450},z)$ is the apparent magnitude corresponding to absolute magnitude $M_{1450}(\mathcal{R},G,z)$, Ω is the solid angle of the survey, and $dV/dz \ d\Omega$ is the co-moving volume element corresponding to a redshift interval dz and solid angle $d\Omega$ at a redshift z and using an assumed cosmology. This approach is explained in detail by Adelberger (2002). For this measurement of the LF, we averaged V_{eff} over bins 1 mag in width. The effective volume of the survey, as a function of absolute magnitude (and in two cosmologies) is shown in Figure 3.3.

3.4 The luminosity function

Having measured the effective volume of the survey as a function of absolute magnitude, we can place points on the QSO luminosity function simply by placing the observed QSOs in absolute magnitude bins and dividing by the effective volume of the survey at that absolute magnitude. A plot of the luminosity function is shown in Figure 3.4. The vertical errorbars indicate 1-sigma confidence intervals reflecting the Poisson statistics due to the number of QSOs in the bin. The uncertainty in V_{eff} is not reflected, as the Poisson statistics dominate (e.g., there is only 1 QSO in the faintest bin, where imprecisions in photometry lead to the greatest V_{eff} uncertainty). The horizontal errorbars indicate the rms width of the bin, weighted according to the effective volume and expected luminosity function (Pei 1995) as a function of absolute magnitude; for a bin centered on $M = M_0$ and 1 magnitude wide, the position of the point and its errorbar width are given by

$$\langle M \rangle = \frac{\int_{M_0-1/2}^{M_0+1/2} M \ V_{\text{eff}}(M) \ \Phi(M) \ dM}{\int_{M_0-1/2}^{M_0+1/2} V_{\text{eff}}(M) \ \Phi(M) \ dM} \qquad (3.6)$$

$$\sigma_M = \left(\frac{\int_{M_0-1/2}^{M_0+1/2} (M - \langle M \rangle)^2 \ V_{\text{eff}}(M) \ \Phi(M) \ dM}{\int_{M_0-1/2}^{M_0+1/2} V_{\text{eff}}(M) \ \Phi(M) \ dM} \right)^{1/2} \qquad (3.7)$$

where $\Phi(M)$ is the $z = 3$ luminosity function of Pei (1995); as both the Pei LF and the observed points are quite flat at these magnitudes, this calculation is insensitive to the

precise slope assumed for $\Phi(M)$, and retroactively trying our fitted value has no significant effect on the results. An $\Omega_m = 1$, $\Omega_\Lambda = 0$, $h = 0.5$ cosmology has been assumed for comparison with previous work.

Comparison with the other points shown in Figure 3.4 suggests that our results are largely consistent with previous measurements (Wolf et al. 2003; Warren et al. 1994; Fan et al. 2001b) in the region of overlap. The shape of the LF near the power-law break is somewhat unclear, and our present sample is unable to resolve this issue. The total luminosity of the LF is quite sensitive to the location of the break. A shallower, wide-field survey using identical LBG techniques is nearing completion (Chapter 4), and should better constrain the $-27 < M_{1450} < -24$ portion of the luminosity function.

The observed faint-end slope appears to be considerably flatter than $\beta_l = 1.64$ used by Pei (1995). The Pei $z = 3$ LF is shown as the dashed curve in Figure 3.4. In order to quantify the difference, we have fit the double power-law of Boyle et al. (1988), identical in form to that used by Pei,

$$\Phi(L, z) = \frac{\Phi_\star/L_z}{(L/L_z)^{\beta_l} + (L/L_z)^{\beta_h}}, \tag{3.8}$$

where β_l and β_h are the faint- and bright-end slopes, respectively, $L_z(z)$ is the luminosity of the power-law break, and $\Phi_\star$ is the normalization factor. We have combined our data with those of Warren et al. (1994) to fit the entire luminosity function. The SDSS data plotted in Figure 3.4 were excluded because they were measured at $z > 3.6$, and the authors have demonstrated redshift evolution in the bright-end slope. Given the relatively small number of data points and large errorbars, fits for the four parameters $(L_z, \Phi_\star, \beta_l, \beta_h)$ are degenerate. We have therefore assumed that the Pei (1995) luminosity evolution model still holds, and adopted the same values for L_z and $\Phi_\star$. A weighted least-squares fit for β_l and β_h was performed, and the measured faint-end slope was $\beta_l = 1.24 \pm 0.07$. The measured bright-end slope was $\beta_h = 4.56 \pm 0.51$, but in addition to the large uncertainty, this parameter is highly degenerate with the assumed parameters L_z and $\Phi_\star$, and is very sensitive to the brightest data point. Likewise, the errorbars for the faint-end slope are smaller than they would be for a general four-parameter fit. The reduced χ^2 for the fit is 1.12. This fit for the luminosity function is shown as a dashed curve in Figure 3.4.

A possible explanation for the flat faint-end slope is that we have overestimated our

completeness at the faint end, by failing to identify the AGN signatures in faint QSOs, perhaps because faint AGN might be overwhelmed by the light from their host galaxies. We do not believe this to be the case, for several reasons. First, in no case have we observed "intermediate" cases of star forming galaxies with broad emission lines superposed. In contrast to virtually all LBG spectra (Shapley et al. 2003), we do not see interstellar absorption lines in any of the spectra of broad-lined objects at $z \sim 3$. However, perhaps the strongest argument comes from examining the spectral properties of identified $z > 2.5$ X-ray sources in the 2 Ms catalog for the *Chandra* Deep Field North and other very deep X-ray surveys. If it were common for AGN to be overwhelmed by their host galaxies, there would be a significant number of faint X-ray sources with spectra that resemble those of ordinary star forming galaxies. To date, virtually all published spectra of objects identified in the redshift range of interest have obvious AGN signatures in their spectra, whether they are broad-lined or narrow-lined AGN.

We can also directly compare the Barger et al. (2003) CDF–N catalog with our own color-selected catalog in their region of overlap, with the following results: There are 2 AGN (1 narrow-lined, 1 QSO) which are detected by *Chandra* and also discovered in the LBG survey; there are 2 QSOs which are detected by *Chandra* but did not have LBG colors in our survey (one of which does have LBG colors in more recent photometry); and there is 1 QSO detected by *Chandra* which has LBG colors but is slightly too faint for inclusion in our survey. These results are consistent with our overall completeness estimates, which are approximately 50% over the range of redshifts considered. In addition, there is a narrow-lined AGN ("HDF–oMD49") discovered in the LBG survey which is detected in the *Chandra* exposure (Chapter 2) at a level below the limit for inclusion in the main catalog (Alexander et al. 2003); another identified narrow-lined AGN at $z = 2.445$ has no *Chandra*-detected counterpart. Of the 84 objects with $2.5 \leq z \leq 3.5$ in our current color-selected spectroscopic sample in the GOODS–N field, only 2 are detected in the 2 Ms *Chandra* catalog, and both are obvious broad-lined QSOs.

Taken together, all of these arguments suggest that optically faint QSOs are unlikely to be missed because of confusion with the UV luminosity of their host galaxies, and thus we believe that our statistics at the faint end are robust.

3.5 Implications for the UV radiation field at $z = 3$

Having measured the luminosity function of QSOs at $z = 3$, we can now place constraints on their contribution to the UV radiation field at that redshift. Integrating over the above parametric fit for the QSO luminosity function, in its entirety, yields a specific luminosity density $\epsilon_{1450} = 1.5 \times 10^{25}$ erg s^{-1} Hz^{-1} h Mpc^{-3}. The luminosity density from our parametric fit is 50% of that predicted from the Pei (1995) fit ($\beta_l = 1.64$, $\beta_h = 3.52$), and is $\sim 8\%$ of the UV luminosity density produced by LBGs at the same redshift based on the luminosity function of Adelberger & Steidel (2000).

Scaling the results of Haardt & Madau (1996), this fit for the LF produces an H I photoionization rate of $\Gamma_{\rm H\ I} \approx 8.0 \times 10^{-13}$ s^{-1}, which can account for a metagalactic flux of $J_{912} \approx 2.4 \times 10^{-22}$ erg s^{-1} cm^{-2} Hz^{-1} sr^{-1}. The ionizing background spectrum and He II ionization fraction, which affect this calculation, are the results of models and are discussed in detail by Haardt & Madau (1996). This value should be considered an upper limit, because the ability of ionizing photons produced by faint AGN to escape their host galaxies has not been measured, and may be lower than for the bright QSOs for which self-absorption in the Lyman continuum is rare (see SSB)[1].

The constraints on the ionizing flux from "proximity effect" analyses of the Lyα forest are uncertain, but are still consistent with the integrated QSO value at $z \sim 3$ (e.g. Scott et al. 2002). In any case, the ratio of the total non-ionizing UV luminosity density of star forming galaxies relative to that of QSOs at $z \sim 3$ implies that QSOs must have a luminosity-weighted Lyman continuum escape fraction that is $\gtrsim 10$ times higher than that of galaxies if they are to dominate the ionizing photon budget.

The detection of the He II Gunn–Peterson effect in $z \sim 3$ QSO spectra has demonstrated that helium reionization occurs during this epoch. Unlike the reionization of hydrogen, which can be effected by radiation from both massive stars and QSOs, the reionization of helium requires the hard UV radiation produced only by QSOs. The improved measurement of the faint-end slope, and hence the total UV luminosity density, will improve simulations of the progress of reionization, which have previously assumed the Pei (1995) value for

---

[1]A propensity to have a higher fraction of Lyman continuum "self-absorbed" QSOs at faint UV luminosities would translate directly into an over-estimate of the completeness correction for a color selected survey such as ours, since an optically thick Lyman limit at the emission redshift makes a QSO more likely to be selected using our color criteria and we are missing fewer than our estimates above would indicate . In this case, we have over-corrected the space density, and the there would be even fewer faint QSOs than we measure above.

the faint-end slope (e.g. Sokasian et al. 2002). Miralda-Escudé et al. (2000) have shown that the previously observed bright end of the luminosity function is sufficient to reionize helium by $z = 3$ under most reasonable assumptions, so the flatter faint-end slope should not dramatically alter the current picture of He II reionization; however, our results may have an effect on the "patchiness" of the reionization as it progresses.

A fortunate consequence of the flat faint-end slope, with implications for IGM simulations, is that the integrated luminosity $\int \Phi(L)\ L\ dL$ converges more rapidly, making the integral insensitive to the lower limit of integration. Simulations will therefore be more robust, with less dependence on the poorly understood low-luminosity AGN population at high redshift.

3.6   Conclusions

Using the 11 QSOs discovered in the survey for $z \sim 3$ Lyman-break galaxies, we have measured the faint end of the $z = 3$ QSO luminosity function. This represents the first direct measurement of the faint end at high redshift. While the entire luminosity function remains well-fit by a double power-law, the faint-end slope differs significantly from the low-redshift value of $\beta_l = 1.64$, being best fit by a slope $\beta_l = 1.24 \pm 0.07$. This results in only half the total QSO UV luminosity compared to previous predictions. As measurements of J_{912} from the Lyα forest continue to improve, we may find that this diminished luminosity from QSOs requires a substantial contribution from star-forming galaxies.

We believe that the survey described here is successful at detecting the same broad-lined QSOs that could be detected in even the deepest X-ray surveys. While the faint X-ray sources that remain unidentified in the *Chandra* Deep Fields may be heavily obscured AGN of similar bolometric luminosity at similar redshifts, these objects do not contribute significantly to the UV luminosity density of the $z \sim 3$ universe. For the first time, we have measured the space density of $z \sim 3$ QSOs down to luminosities that account for essentially all of the UV photon production from AGN. This measurement is of primary interest for an understanding of the physical state of the IGM at high redshift, and not necessarily the evolution of black hole accretion, which is more difficult to quantify without extensive multi-wavelength campaigns. Nevertheless, the results of this paper can be compared directly with a vast literature observing UV-selected broad-lined AGN. Our results on the QSO luminosity

function suggest that either the mass function and accretion efficiency of super-massive black holes at $z \sim 3$ is very different from that at lower redshift, or there has been significant differential evolution of AGN obscuration as a function of bolometric luminosity and/or redshift. If the results are interpreted as a difference in the mass function of supermassive black holes, then they may be consistent with some theoretical work which predicts that low-mass SMBHs form at smaller redshifts than the most massive black holes (e.g. Small & Blandford 1992).
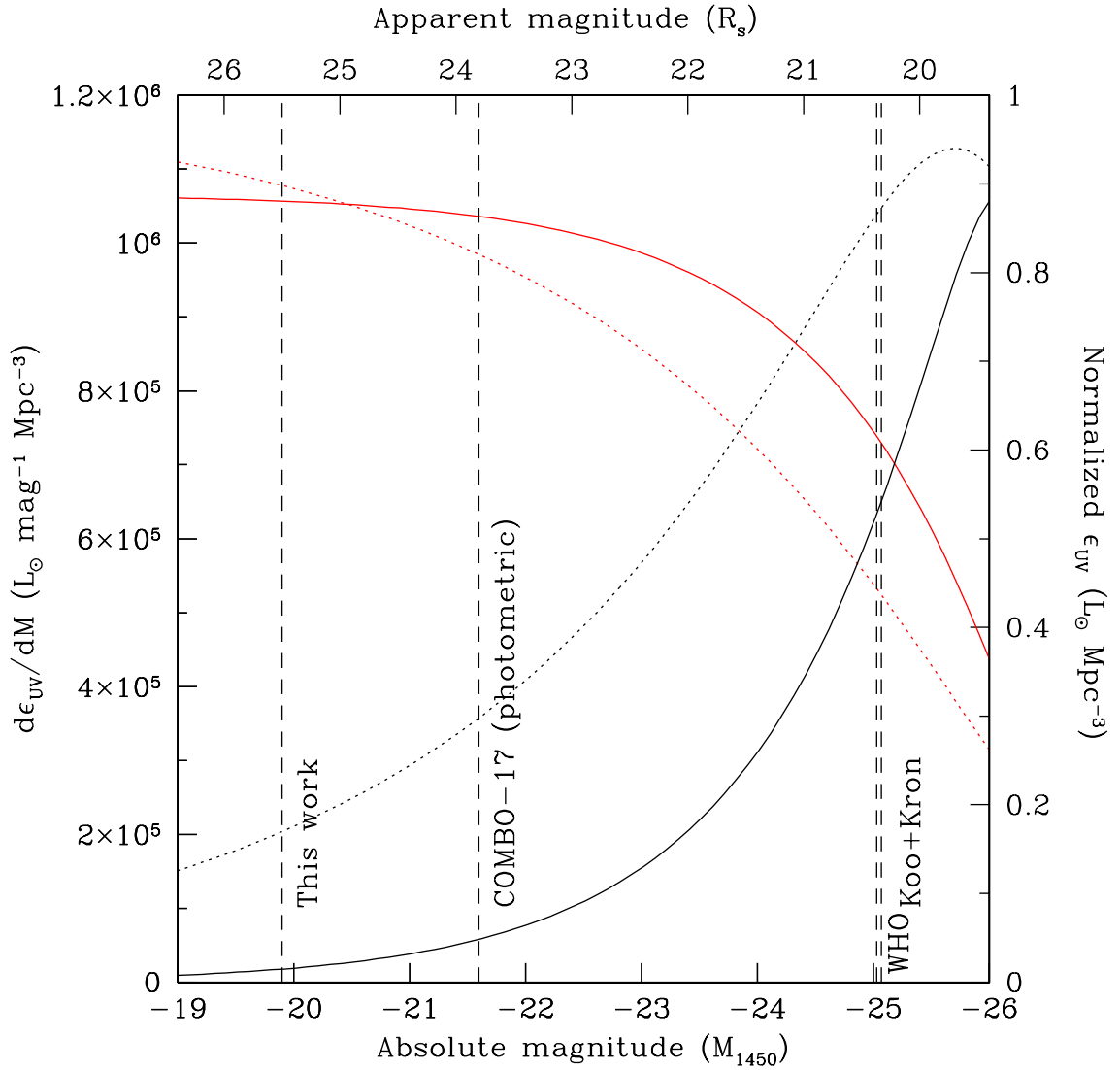
Figure 3.1 The 1450 Å UV luminosity density produced by QSOs as a function of absolute magnitude, assuming the $z = 3$ luminosity function of Pei (1995) (dashed) and our fit described in Section 3.4 (solid). The differential luminosity density is shown by the black curve and is read from the left scale. The cumulative luminosity density is shown by the red curve and read from the right scale, which is normalized to the total. The magnitude limits of this work and other surveys are indicated by dashed lines. The corresponding apparent $\mathcal{R}_s$ magnitude is indicated at the top. It is immediately clear that this work explores a substantially fainter portion of the luminosity function and accounts for virtually all of the total UV luminosity from QSOs.
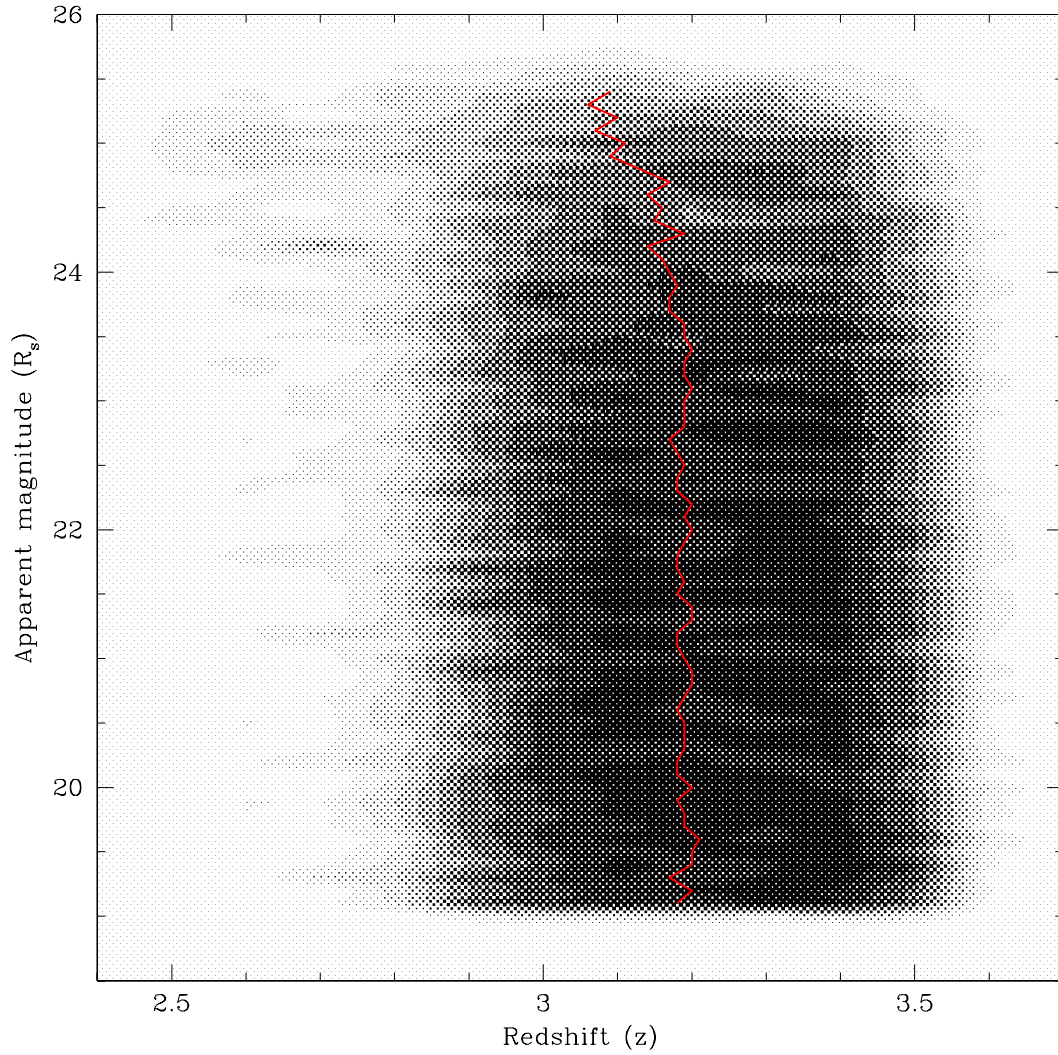
Figure 3.2 The fraction of simulated QSOs having measured colors that satisfy the photometric selection criteria (equations 3.1–3.4) as a function of redshift and apparent $\mathcal{R}_s$ magnitude. The QSOs were simulated using the method described in Section 3.3.1. This plot does not include the effects of spectroscopic incompleteness. The centroid of the distribution, as a function of magnitude, is marked with a red curve. The grayscale levels are evenly spaced at 10% intervals; the darkest level represents completeness in excess of 90%.
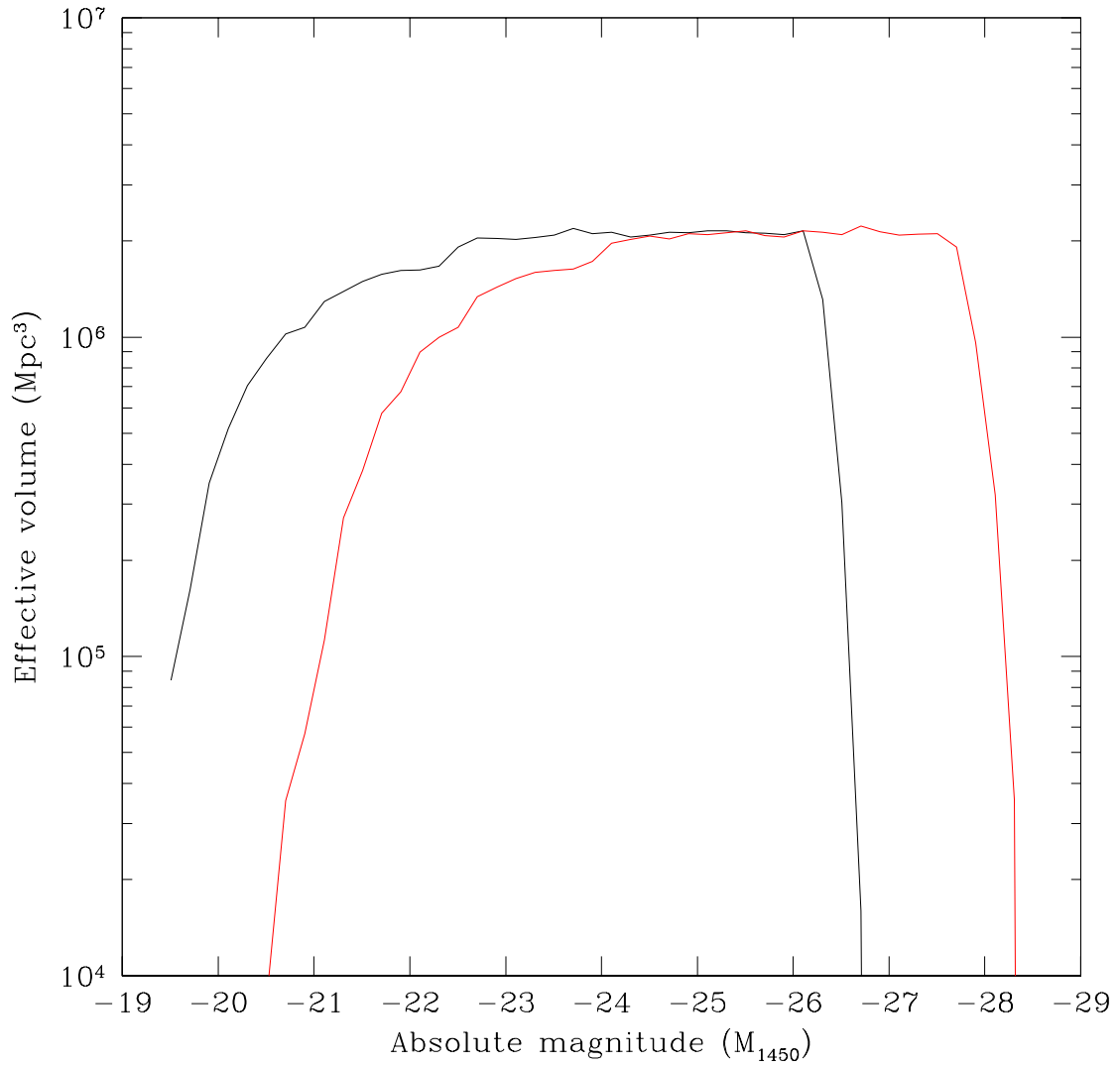
Figure 3.3 The effective volume of the survey as a function of absolute magnitude, calculated using the method described in §3.3.3, using an $\Omega_m = 1$, $\Omega_\Lambda = 0$, $h = 0.5$ cosmology (black) and an $\Omega_m = 0.3$, $\Omega_\Lambda = 0.7$, $h = 0.7$ cosmology (red).
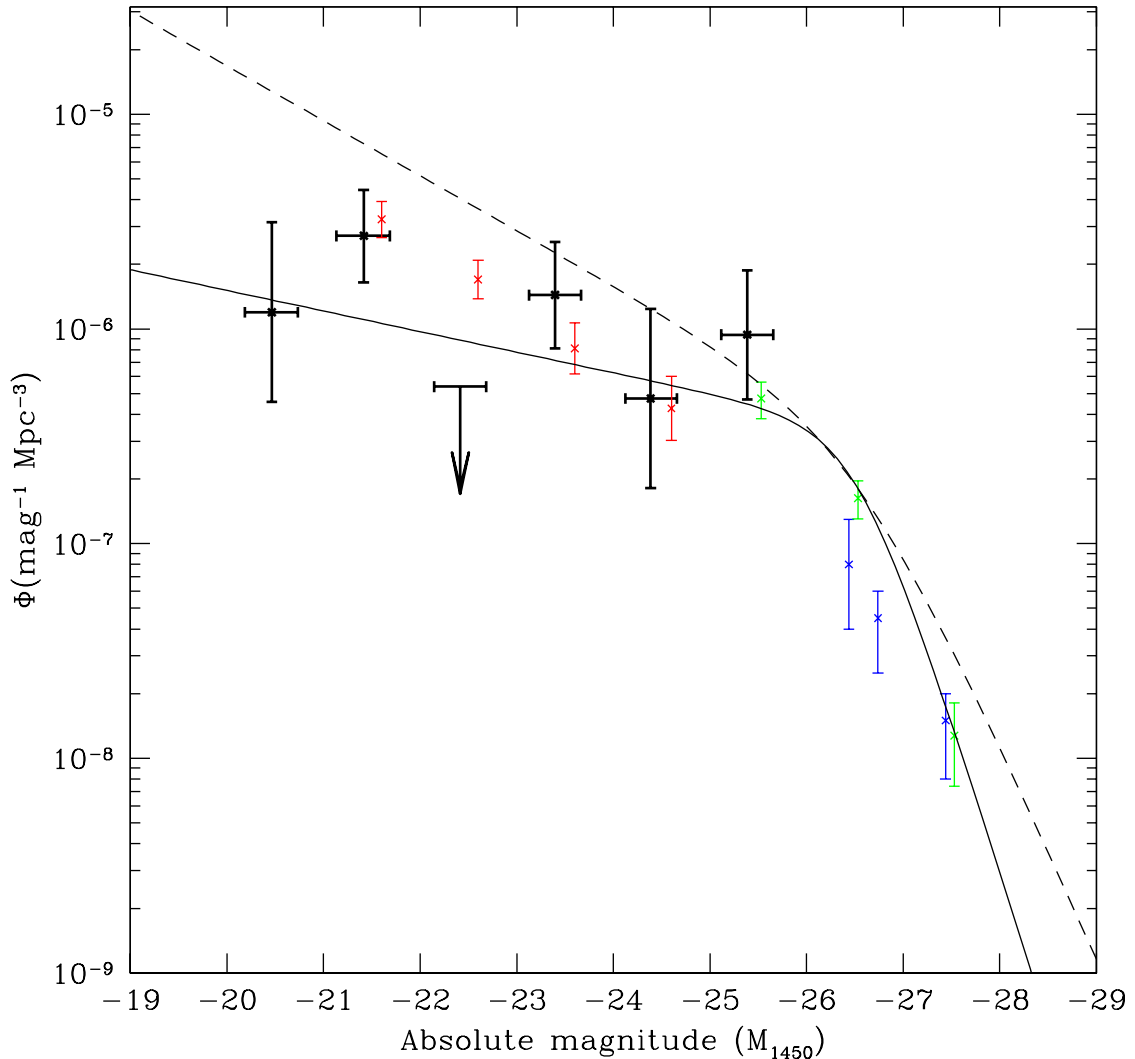
Figure 3.4 The faint end of the $z = 3$ QSO luminosity function under an assumed $\Omega_m = 1$, $\Omega_\Lambda = 0$, $h = 0.5$ cosmology. The vertical errorbars indicate 1-sigma uncertainties arising from Poisson statistics. The horizontal errorbars indicate the expected rms scatter of magnitudes of detectable QSOs in each magnitude bin. The arrow indicates a 1-σ upper limit from an empty bin. The double power-law $z = 3$ LF of Pei (1995) has been converted from M_B to M_{1450} (using an assumed $\alpha = -0.5$ continuum slope) and has been plotted as well using a dashed curve, and our fit is plotted with a solid curve. SDSS points (Fan et al. 2001b) from $3.6 < z < 3.9$ have been evolved to $z = 3.0$ using the luminosity evolution of Pei (1995) and plotted in blue for comparison. The $2.2 < z < 3.0$ and $3.0 < z < 3.5$ points of WHO (Warren et al. 1994) have been combined and plotted in green, and the $2.4 < z < 3.0$ and $3.0 < z < 3.6$ points of COMBO-17 (Wolf et al. 2003) have been combined and plotted in red.

Chapter 4

The survey for medium luminosity $z = 3$ QSOs

4.1 Introduction

When the AGN sample was first culled from the $z \approx 3$ Lyman-break galaxy catalog (see Chapter 2), it became clear that while the survey would provide the first accurate census of faint AGN at that redshift, going much deeper than previous work. In fact, it was likely that a "gap" would occur in our knowledge of the QSO luminosity function at high redshift. Previous work at $z \gtrsim 3$ (e.g., Warren et al. 1994; Fan et al. 2001b) probed only the bright end of the luminosity function [essentially, $L > L_z(z = 3)$ in the Pei (1995) formulation]. The LBG survey data, while being much deeper, covered just 0.38 deg^2; consequently, there are relatively few QSOs at the bright end of the LBG survey, where it joins the previous surveys.

Thus, there were few QSOs in either the LBG survey or previous work to constrain the shape of the LF near $L_z(z = 3)$, the power-law break. Because we are particularly interested in the total QSO contribution to the background UV radiation field, it is essential to understand the LF in this region: the integrated LF is quite sensitive to the luminosity of the power-law break[1]. It was therefore decided to conduct a survey specifically for "medium-luminosity" ($-22.5 \lesssim M_{1450} \lesssim -26$) QSOs at $z \approx 3$.

In order to take advantage of our understanding of the LBG survey's characteristics (see Chapter 3), the medium-deep survey was designed to be essentially identical. Several fields

---

[1]With the benefit of hindsight, we see that this is even more the case than previously thought: The flatter the faint-end slope, the more the "break" region contributes to the integrated LF. As shown in Chapter 3, the faint-end slope is flatter than previously believed.

(ultimately yielding 2 deg^2 of useful data) were imaged in U, g', and $\mathcal{R}_s$. The photometric selection of candidates followed the method of the LBG survey (Chapter 3), with some adjustments as described below (§4.2). The photometric candidates were followed up with low-resolution spectroscopy. Ultimately, the resulting catalog of QSOs was merged with the LBG survey results, to produce a valuable and unique sample, which provides good, reliable statistics over a luminosity range of 6.5 magnitudes.

4.2 Survey description and observations

The intent of the survey was to apply the Lyman-break technique to find medium-luminosity QSOs at $z \approx 3$. In contrast to the survey for Lyman-break galaxies, which surveyed approximately 0.4 deg^2 to a depth of $\mathcal{R} = 25.5$, this survey would cover approximately 2 deg^2 to a depth of $\mathcal{R} = 23$. The large sky coverage would be facilitated by the latest generation of wide-field imagers, including the Large Format Camera (LFC) on the Hale Telescope (see Chapter 5). Recall that the $z = 3$ Lyman-break technique requires imaging in u', g' and $\mathcal{R}$ (or similar filters), and uses the following photometric criteria:

$$\mathcal{R} > 19 \tag{4.1}$$

$$\mathcal{R} < \mathcal{R}_{\text{limiting}} \tag{4.2}$$

$$g' - \mathcal{R} < 1.2 \tag{4.3}$$

$$(g' - \mathcal{R}) + 1 < (u' - g'). \tag{4.4}$$

It is clear from these requirements that the u' imaging must be substantially deeper than the $\mathcal{R}$ or g' filters. Furthermore, it takes longer to reach a given depth in u' than in redder filters, because seeing, atmospheric opacity, and instrument QE tend to be substantially worse in u'. Thus, it seemed that the main observational challenge would be to obtain enough imaging data in u', especially given the unreliable seeing conditions at Palomar.

Fortunately, a solution presented itself. A. Connolly had $UBVRI$ imaging of DEEP2 survey fields, taken with the Mosaic camera on the Kitt Peak 4-m telescope. This imaging data had several desirable properties: It covered several square degrees, the fields were well-spaced in RA to permit flexible telescope scheduling, and the U data were sufficiently deep to allow the QSO survey to reach $\mathcal{R} = 23$, as hoped. A collaboration was formed to

allow the use of the U data for the QSO survey.

The use of KPNO data in other filters (e.g., B and R) was considered, but for consistency with the LBG data set, it was decided to image the DEEP2 fields in g' and $\mathcal{R}$ with LFC. Each Mosaic image could be well-covered by three LFC pointings. Typical LFC observations were 12–16 minutes (in 2 exposures) in each of g' and $\mathcal{R}$.

The LFC imaging data were reduced in the standard way for the LFC, as described in Chapter 5. The KPNO Mosaic data were provided in reduced form (a result of the same `mscred` package for IRAF). The LFC data were then placed in register with the corresponding Mosaic data; typically, three LFC pointings were registered onto each Mosaic image. The total useful survey area, as defined in detail below, was 1.95 deg^2.

In the LBG survey, photometry was performed using a customized version of FO-CAS (Jarvis & Tyson 1981). For the survey discussed here, it was decided to instead use Sextractor[2], for a variety of reasons. Sextractor is considerably faster than FOCAS, which is an important advantage with the large images from this survey. FOCAS also has hardcoded limits for various internal lists, which were exhausted with the large data, and would have required code modifications to remedy. Because the ultimate goal was to merge the results from both surveys, consistency of results was a priority, and a subset of the images were photometered with both FOCAS and Sextractor to verify consistent, bias-free results.

The U data, at the time they were provided, had not been photometrically calibrated. The zeropoints for these data were obtained through comparison with calibrated data from other surveys, including SDSS. Some of the g' and $\mathcal{R}$ data were taken under photometric conditions, and were calibrated using standard stars (Massey et al. 1988). In other cases, they were calibrated using data from other surveys, as with the U data. Because $\mathcal{R}$ is a custom filter, it was necessary to transform SDSS photometry using $\mathcal{R} = (r' + i')/2$. Data in the Hubble Deep Field North, where imaging data in $\mathcal{R}$, r', and i' exist, were used to verify that this transformation is accurate enough for the purposes of this survey.

Photometric selection of candidates proceeded essentially as described in Equations 4.1–4.4, with $\mathcal{R}_{\text{limiting}} = 23$. There were a few exceptions: First, one pointing (`Hr23_3`) was limited to $\mathcal{R} < 22$, because observing conditions did not permit accurate photometry to $\mathcal{R} = 23$. Second, candidates with $g' - \mathcal{R} > 0.8$ were excluded, to various degrees, from

---

[2]Source Extractor by E. Bertin, available from `http://terapix.iap.fr/rubrique.php?id_rubrique=91`.

spectroscopic follow-up. In this survey, contamination from stars (especially K stars) was an important problem, resulting in wasted spectroscopic observations. These stars were not a major problem in the LBG survey, because at faint magnitudes ($24 \lesssim \mathcal{R} \lesssim 25.5$) LBGs far outnumber stars; but this is not the case at $\mathcal{R} < 23$. Fortunately, QSOs at $z = 3$ tend to be blue ($0.5 \lesssim g' - \mathcal{R} \lesssim 0.8$), while the stellar contaminants tend to be red ($1.0 \lesssim g' - \mathcal{R} \lesssim 1.2$). Thus, after obtaining enough data for red objects to verify the above claims, it was decided to devote less time to the red objects. Third, initial spectroscopic observations were limited to candidates with a strong Lyman break $[(g' - \mathcal{R}) + 1.2 < (u' - g')]$. This decision was a hedge against inaccurate photometry and also served to probe a region of color space with minimal stellar contamination. After experiencing success with these candidates, the selection was expanded to the normal LBG criterion, with a minimum "break" of 1.0 mag (Equation 4.4). These various modifications to the selection criteria are summarized in Table 4.1. Naturally, all of these variations were taken into account when computing the effective volume of the survey.

Before each spectroscopy run, the photometric candidates were reviewed by eye, to decide which merited observation. It quickly became clear that, because only two short exposures were used in each pointing (in each of g' and $\mathcal{R}$), the "chip gap" and bad column regions of the images yielded spurious detections. Objects near such defects (along with objects near very bright stars) were not observed spectroscopically, and such regions were not counted toward the total effective volume of the survey.

Nearly all of the spectroscopic follow-up was performed with the Double Spectrograph at the Cassegrain focus of the Hale Telescope (DBSP; Oke & Gunn 1982). Various low-resolution configurations were employed: blue side alone, D-68, 300 l/mm; both sides, D-48, 300 l/mm (blue) and 316 l/mm (red); and red side alone, clear, 316 l/mm. All DBSP observations were performed with a single candidate at the center of a 2 arcsec wide slit, oriented near the parallactic angle. Exposure times generally ranged from 1200 to 3600 s, depending on observing conditions and the magnitude of the object being observed. An additional exposure was taken when the first spectrum was inconclusive. The resulting spectra provided adequate signal-to-noise for to determine whether the objects were QSOs, and to measure their redshifts. Most of the non-QSO spectra showed absorption lines positively identifying them as stars. A small number of candidates were observed at the W. M. Keck Observatory using the Low Resolution Imaging Spectrometer (LRIS; Oke et al.

1995). These candidates, none of which are QSOs, were drawn primarily from the faint, red, weak-Lyman-break portion of the color space. These spectra helped to confirm that this part of the selection function yielded many stellar contaminants, and few QSOs.

The spectra were reduced using the `noao.twodspec` and `noao.onedspec` packages for IRAF. The data were flat-fielded using dome flats, and wavelength-calibrated using internal arc lamp illumination (typically helium, neon, and mercury). The arc lamp exposures were taken at the same telescope position and rotator angle as the corresponding science exposures. Flux calibration was performed using the spectrophotometric standards of Massey et al. (1988), but should not be trusted as an absolute calibration. Many of the QSO spectra were taken in non-photometric conditions.

4.3   Results from the medium-luminosity survey

4.3.1   Overview of AGN discovered

Thirteen $z \approx 3$ QSOs in the range $19 < \mathcal{R} < 23$ were discovered in this survey, providing a substantial and useful companion catalog to the LBG survey QSOs. Table 4.2 lists the magnitudes, colors, and redshifts of the new QSOs, and their colors are illustrated in Figure 4.1. The mean redshift of the sample is $\langle z \rangle = 3.12$ with $\sigma_z = 0.28$. That the mean is greater than $z = 3$ is to be expected; candidates whose photometry indicated a strong Lyman break (as defined in §4.2) were preferentially observed. Such QSOs will tend to be at $z > 3$, because the break appears to be stronger as the 912 Å Lyman limit is redshifted completely out of the U filter. The apparent magnitude distribution is described by $\langle \mathcal{R} \rangle = 21.2$ and $\sigma_{\mathcal{R}} = 0.92$.

While the primary goal of the survey was to discover medium-luminosity QSOs, it was also hoped that unusually bright (or lensed) LBGs, akin to MS1512–cB58 (Pettini et al. 2002) might be discovered. No convincing examples have been found, and it is probably safe to say that no LBGs with Lyman-α emission were observed spectroscopically. We cannot positively rule out LBGs without emission lines; not all of the spectra were of sufficient quality to identify a galaxy using absorption lines. An apparent narrow-lined AGN, similar to those discussed in Chapter 2, was discovered in a field near the Groth Strip. The $z = 3.07$, $\mathcal{R} = 22.7$ object was identified from a narrow Lyman-α emission line. C IV was not visible, due to sky lines. Because interstellar absorption lines were not visible in the spectrum, the

Table 4.1 Summary of object selection criteria in each field.

Field	Coordinates	Selection criteria[a]	
		Strong Lyman break[b]	Weak Lyman break[c]
Groth_1	1416+5215	50% to $\mathcal{R} = 23$ $(g' - \mathcal{R} < 0.8)$; 0% otherwise	
Groth_3	1413+5215	100% to $\mathcal{R} = 23$ $(g' - \mathcal{R} < 0.8)$; 0% otherwise	
Hr2_1	0227+0035	100% to $\mathcal{R} = 23$	0%
Hr2_2	0229+0035	100% to $\mathcal{R} = 23$	0%
Hr16_5	1652+3525	100% to $\mathcal{R} = 23$	100% to $\mathcal{R} = 23$ $(g' - \mathcal{R} < 0.8)$; 0% $(g' - \mathcal{R} > 0.8)$
Hr16_6	1652+3555	100% to $\mathcal{R} = 23$	100% to $\mathcal{R} = 23$ $(g' - \mathcal{R} < 0.8)$; 50% to $\mathcal{R} = 23$ $(g' - \mathcal{R} > 0.8)$
Hr23_1	2327+0008	100% to $\mathcal{R} = 23$	100% to $\mathcal{R} = 23$ $(g' - \mathcal{R} < 1.0)$; 0% $(g' - \mathcal{R} > 1.0)$
Hr23_3	2331+0007	100% to $\mathcal{R} = 22$	100% to $\mathcal{R} = 23$ $(g' - \mathcal{R} < 1.0)$; 0% $(g' - \mathcal{R} > 1.0)$

[a] These criteria are expressed as modifications to the basic set of criteria shown in Equations 4.1–4.4.
[b] $(u' - g') - (g' - \mathcal{R}) > 1.2$; these tend to have $z \gtrsim 3.0$.
[c] $1.0 < (u' - g') - (g' - \mathcal{R}) < 1.2$; these tend to have $z \lesssim 3.0$.

Table 4.2 List of QSOs discovered in the medium-luminosity survey.

Identifier	z	$\mathcal{R}$	$g' - \mathcal{R}$	$U - g'$	Observed
2_1_Q5	3.45	22.0	0.8	3.2	Sep. 2002
G1_Q58	2.52	19.6	0.3	1.8	Jun. 2003
G1_Q85	3.15	22.0	0.5	1.6	Jun. 2003
G1_Q82	3.17	22.7	0.5	2.8	Jul. 2003
16_6_Q37	3.08	20.6	0.6	3.0	Sep. 2002
16_6_Q26	3.12	20.5	0.6	2.0	Sep. 2002
16_6_QM4	3.24	22.2	0.0	1.0	Aug. 2003
23_3_Q80	2.85	21.5	0.8	2.9	Jul. 2003
23_3_Q30	2.86	21.0	0.4	1.6	Jul. 2003
23_1_Q6	2.95	21.1	0.4	1.7	Sep. 2002
23_1_Q13	3.18	20.3	0.7	2.0	Sep. 2002
23_3_Q5	3.44	20.3	0.8	3.4	Sep. 2002
23_1_Q12	3.62	22.4	1.0	—	Sep. 2002
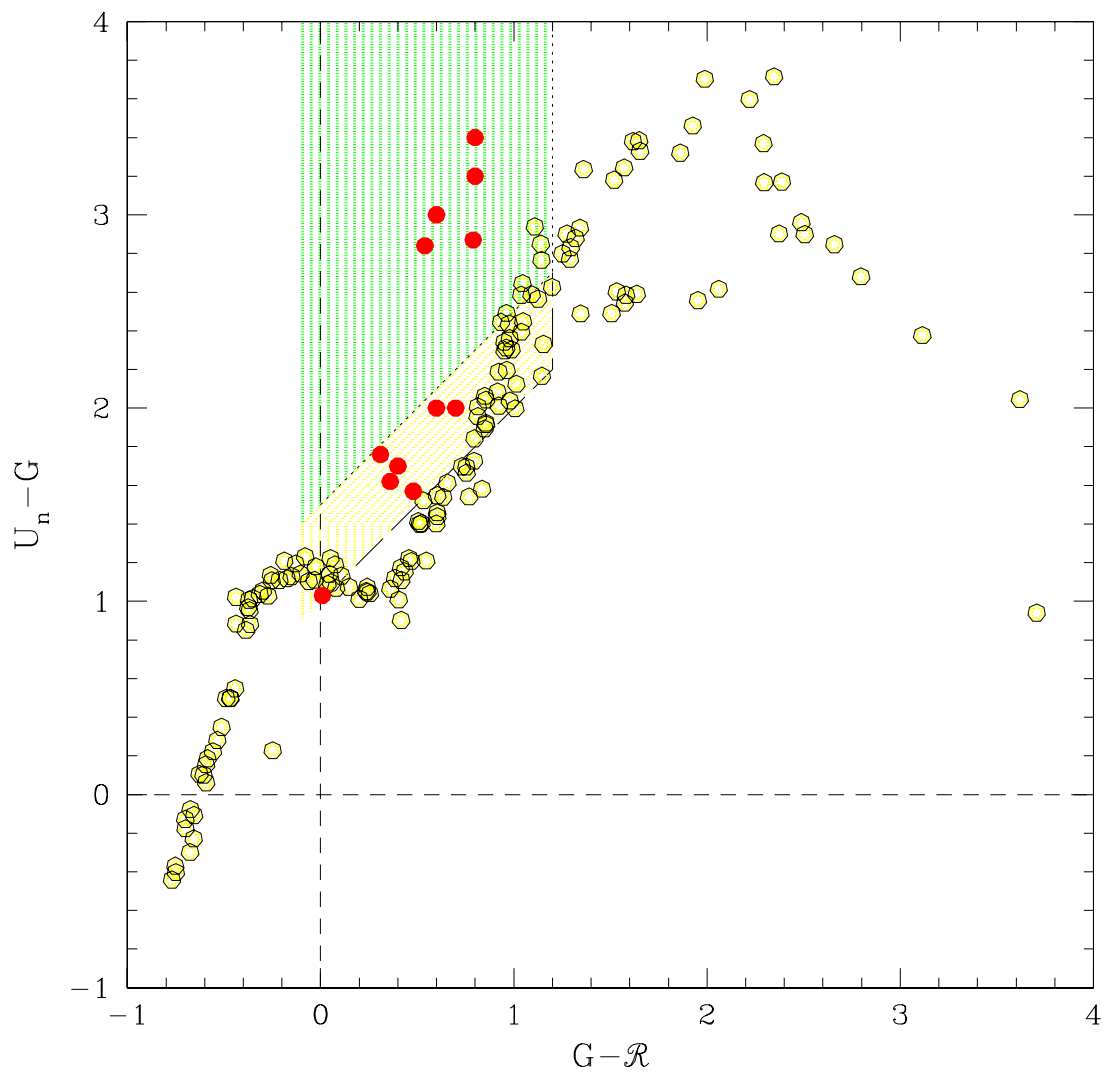
Figure 4.1 The colors of the QSOs discovered in the medium-luminosity survey are shown in red. The yellow points illustrate the stellar locus, using the stars of Gunn & Stryker (1983). The green region is the "Weak Lyman break" selection region, and the yellow region is the "Strong Lyman break" region; these are discussed in §4.2.

object was deemed to be an AGN, rather than a LBG. The apparent magnitude of this object is quite nearly the same as the brightest NL AGN discovered in the LBG survey (Table 2.1). That NL AGN in the two surveys are limited to $\mathcal{R} \gtrsim 22.5$ suggests a NL AGN LF break approximately 2 mag fainter than the QSO LF break.

4.3.2 Characterization of the survey

The characterization of the medium-luminosity survey proceeded similarly to that of the LBG survey, as described in §3.3. First, a template spectrum of a QSO was redshifted to various redshifts; its continuum slope and emission line strengths were randomly altered to reflect the observed distribution of these quantities; Lyman limit systems and a Lyman-α forest were added, corresponding to a random line of sight through the IGM; and its colors in the $Ug'\mathcal{R}$ photometric system were measured and recorded. Such transformations were performed hundreds of times, in order to create a large corpus of synthetic QSO colors, corresponding to the expected distribution of real-life QSO colors.

Then, artificial point sources (convolved with the image PSF) were added to the actual science images, with colors drawn from the distribution generated above. This process was essentially the same as that performed for the LBG survey, but various technical improvements were required:

- The existing code was designed to work with our modified version of FOCAS (Jarvis & Tyson 1981). Because this survey used Sextractor for photometry, the simulation driver had to be adapted to use Sextractor instead.

- As a side effect, the code to add objects to images had to be altered to work with FITS files, instead of `.imh`/`.pix` files. Sextractor works with the former, FOCAS the latter.

- Originally, three instances of the object-adding code were run at once (one for each of the U, g', and $\mathcal{R}$ images). This led to mysterious crashes, because the three instances all tried to load a science image into memory at once. Because the images for this survey are much larger than for the LBG survey, the workstation's memory was exhausted.

- A method was added to query an exposure map for each image. This allowed objects

to be placed only on fully exposed parts of the image, which were the only parts to
be counted in the effective volume computation.

As was the case in the LBG survey, the photometric completeness was determined by
measuring the fraction of simulated QSOs that had measured colors meeting the selection
criteria (Equations 4.1–4.4, as modified by Table 4.1). A decision tree was used to implement
the field-by-field criteria, and the effective volume of the survey, as a function of M_{1450} was
calculated. As in the LBG survey, the M_{1450} magnitudes of objects were estimated using a
redshift-dependent linear combination of $M_{\mathcal{R}}$ and $M_{g'}$, with a redshift-dependent correction
factor for the effect of the Lyman-α forest moving into the g' band. Also as in the LBG
survey, all calculations were performed using an $\Omega_m = 1$, $\Omega_\Lambda = 0$, $h = 0.5$ cosmology, which
is the usual choice for QSO LF work. A plot of the effective volume of the survey, as a
function of absolute magnitude, is shown in Figure 4.2.

4.3.3   The luminosity function

Having calculated the effective volume of the survey, the observed QSOs can be binned
by luminosity, and plotted as a luminosity function. The results from the new survey are
shown in Figure 4.3. In this figure, the fit from Chapter 3, with $\beta_l = 1.24$, is retained. You
can see that the new points are consistent with that fit. It is important to note also that the
brightest point, and the adjacent upper limit, are consistent with existing work, in particular
the results of Warren et al. (1994). This agreement is encouraging; since essentially the same
selection and analysis methods were used in the LBG survey (Chapter 3), we can be quite
confident in the reliability of that survey as well.

When the data from both the LBG and new survey are merged, the points in Figure 4.4
result. A new fit to the merged data set is shown in the figure. With $\beta_l = 1.20$ and
$\beta_h = 4.54$, it is very similar to the fit from Chapter 3. The new fit was computed in the
same way as the previous one, as described in §3.4. Once again, the normalization and
$L_z(z = 3)$ were taken from the Pei (1995) model and held constant in the fit, and the
results of Warren et al. (1994) were used to constrain the bright end.

In addition to the least-squares fit, two other analyses were used to place constraints
on the faint end. First, the method of Kolmogorov-Smirnoff was used to measure the slope
of our unbinned data. The best fit for the slope was $\beta_l = 1.43$, and the 95% confidence
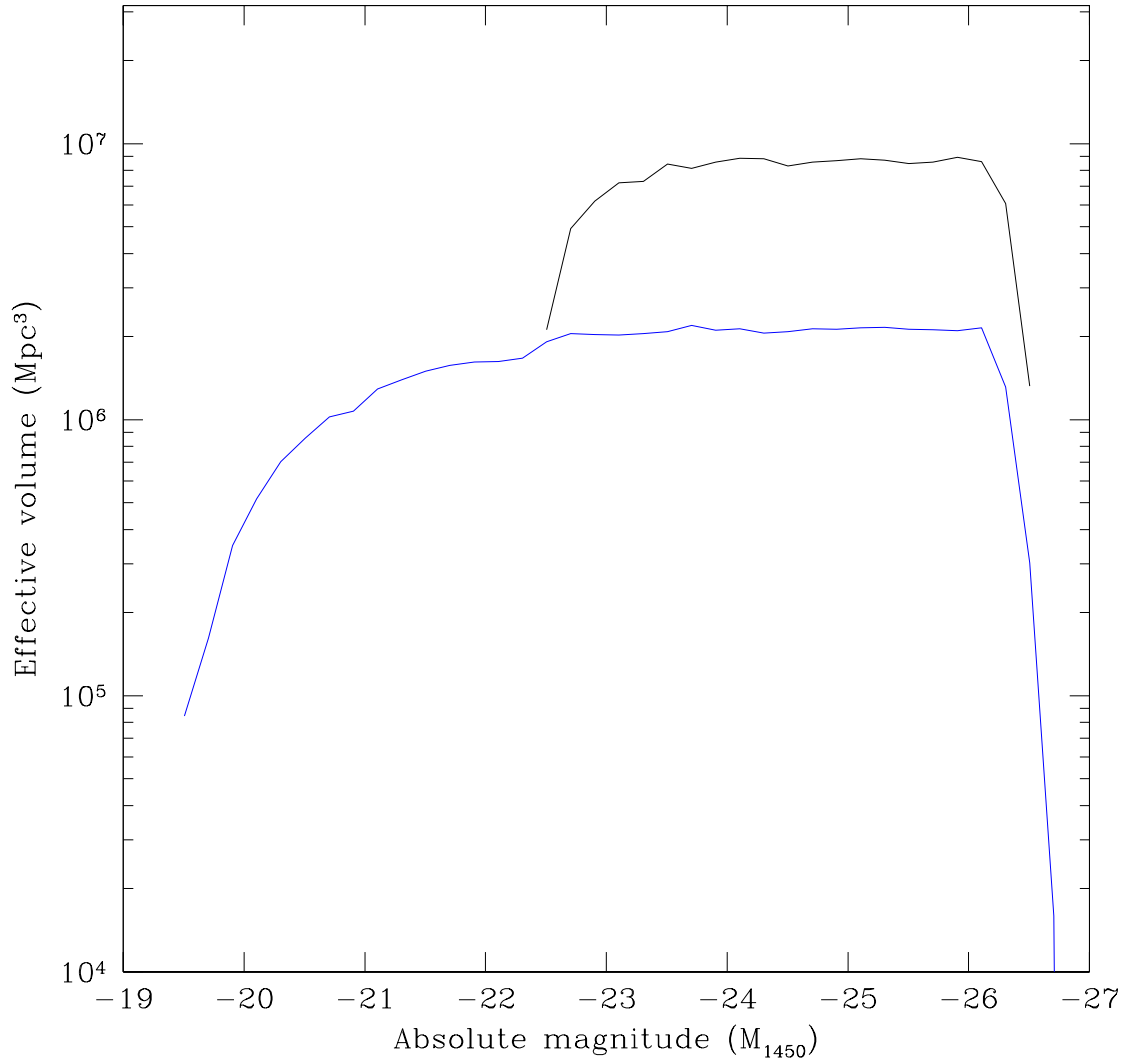
Figure 4.2 The effective volume of the two surveys as a function of absolute magnitude. The medium luminosity survey is shown in black, and the LBG survey is shown in blue. The calculations used an $\Omega_m = 1$, $\Omega_\Lambda = 0$, $h = 0.5$ cosmology.

interval was $1.13 < \beta_l < 1.60$. The Pei (1995) slope of $\beta_l = 1.64$ is ruled out with 98% confidence. This method is blind to normalization, which explains the discrepancy between the least-squares fit and the K-S fit. Fitting the data with a slope of 1.43 would require a decrease in $\Phi_\star$, and an increase in $L_z(z = 3)$ to match the bright end data.

A complimentary test was to compare the predicted number of QSOs in our survey, as a function of β_l, with the actual number, 24. The other LF parameters were held at the Pei (1995) values. The best fit from this approach was $\beta_l = 1.24$, in good agreement with the least-squares fit, with a 95% confidence range $1.05 < \beta_l < 1.38$. Once again, the $\beta_l = 1.64$ model is strongly ruled out.

It is also worthwhile to compare our LF points with those of the COMBO-17 group (Wolf et al. 2003). Figure 4.4 shows points from that survey in red; their 2.4–3.0 and 3.0–3.6 redshift bins have been combined in the plot. At bright luminosities ($M_{1450} \lesssim -23$), there is good agreement with our results. At fainter magnitudes, there is some discrepancy, with the COMBO-17 points lying between our points and the Pei (1995) model. A few factors may contribute to the discrepancy. First, there is evidence that the COMBO-17 measured LF is flatter in the $3.0 < z < 3.6$ interval than in the $2.4 < z < 3.0$ interval (Wolf et al. 2003, fig. 9a). In their two faintest luminosity bins, the authors have more than three times as many QSOs in the lower redshift interval than the higher. Consequently, the flattening of the slope may not be reflected in the merged points. Second, the selection efficiency and (more importantly) the contamination fraction may not be as well understood near the limiting magnitude of COMBO-17. It is reasonable to expect that redshift aliasing becomes an increasingly important problem at faint apparent magnitudes. The authors also note that due to limited spectroscopic confirmation, the selection function for low-luminosity AGN is not completely understood.

4.4   Interpretation and conclusions

The QSO survey described in this chapter strengthens the results presented in Chapter 3. The two surveys clearly show that the faint-end slope of the QSO luminosity function is substantially flatter at $z = 3$ than in the local universe (with $\beta_l = 1.20$), a result that was not generally anticipated. The improved data also suggest that the Pei (1995) model for the evolution of the power law break, $L_z(z)$, continues to hold at $z = 3$. Previously, it
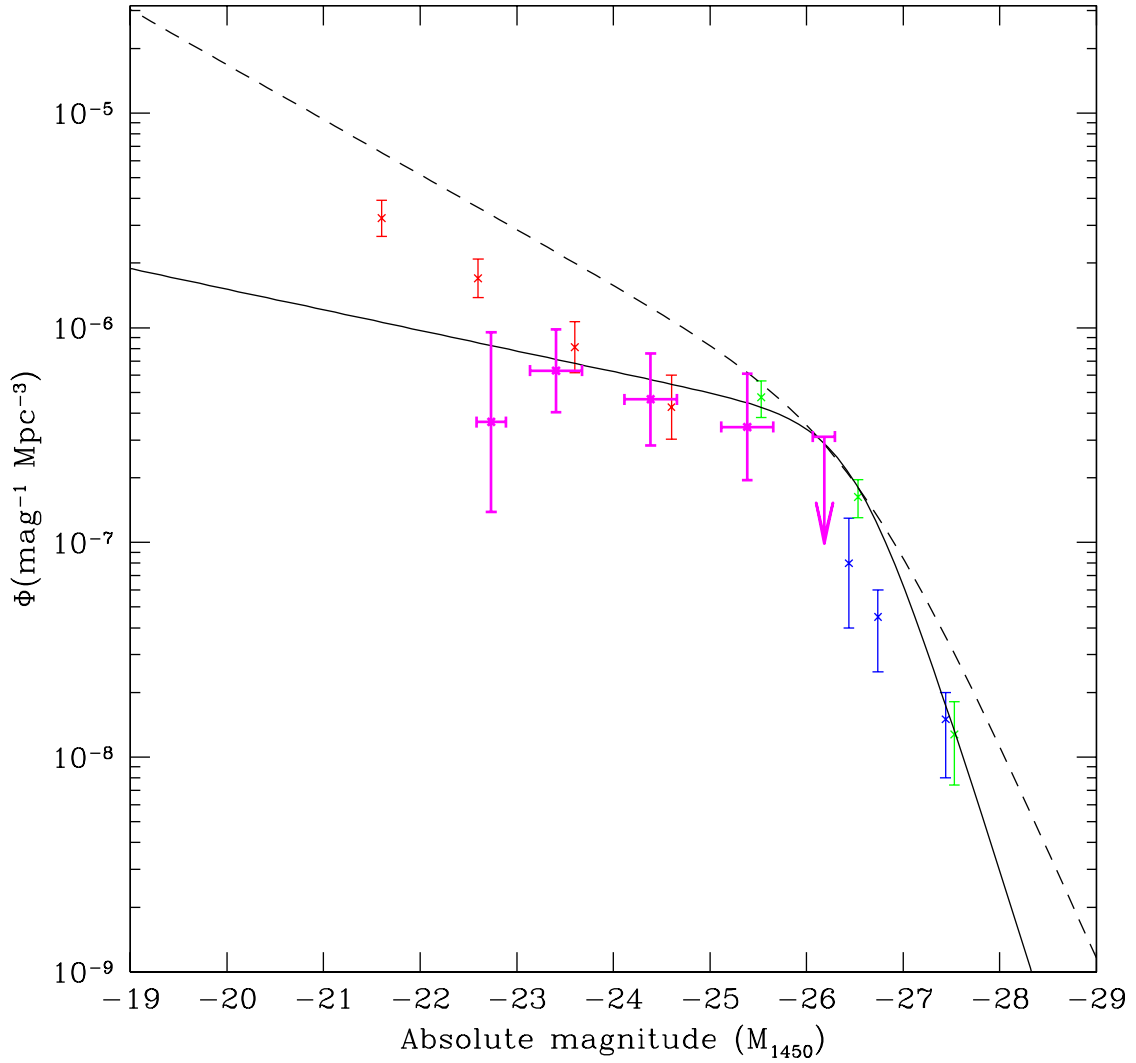
Figure 4.3 The QSO luminosity function from the medium-deep survey. The points from the survey are shown in magenta. All other aspects of the plot are identical to Figure 3.4 (COMBO-17 in red, WHO in green, SDSS in blue; the solid line is the Chapter 3 fit, with $\beta_l = 1.24$).
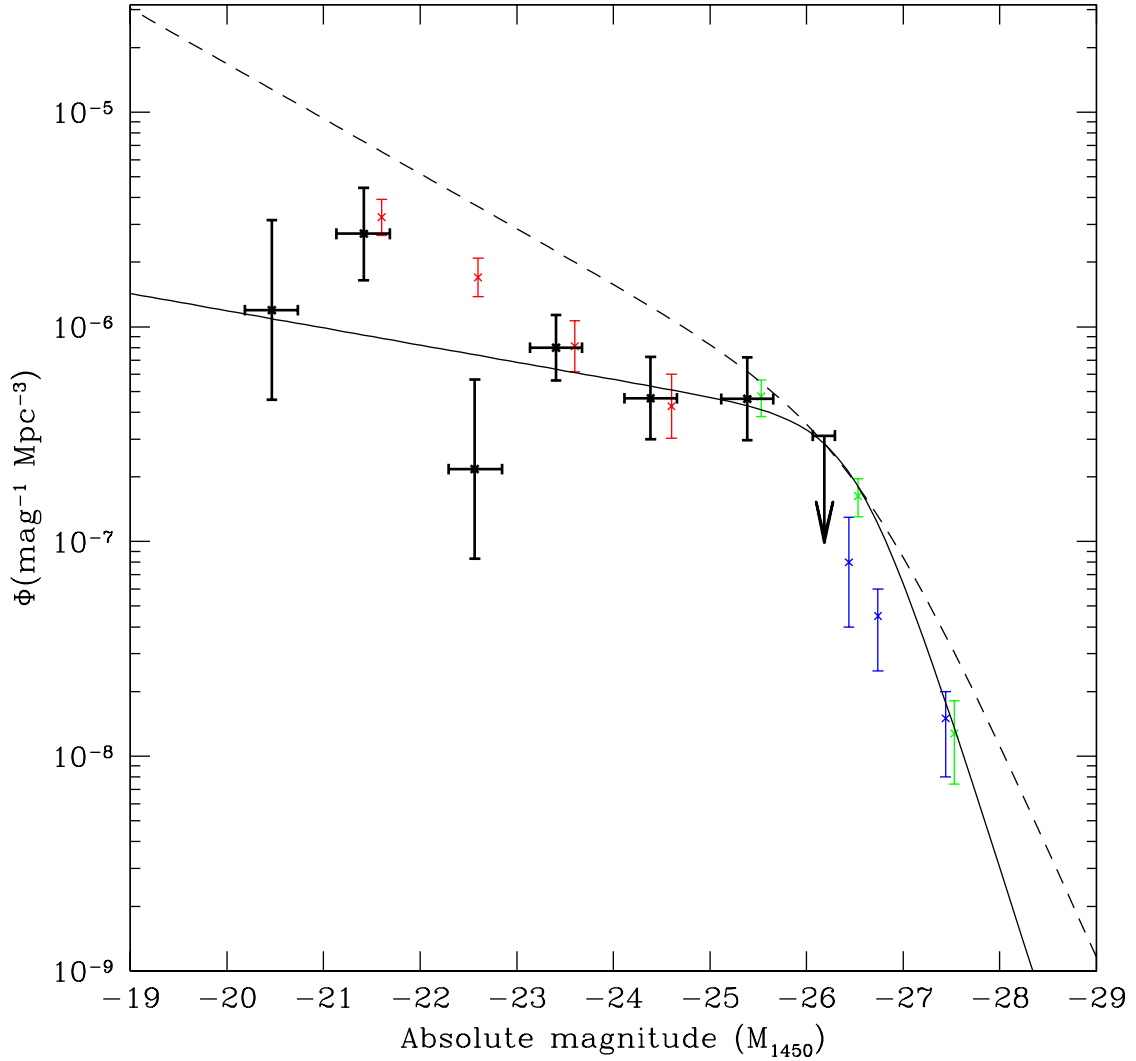
Figure 4.4 The QSO luminosity function from both the LBG survey and the medium-deep survey. The points from the merged surveys are shown in black. The dashed line is the Pei (1995) model for the $z = 3$ LF; the solid line is the new fit presented in §4.3.3, with $\beta_l = 1.20$. All other aspects of the plot are identical to Figure 3.4 (COMBO-17 in red, WHO in green, SDSS in blue).

was difficult to constrain this part of the LF, due to a lack of data on the faint side of the break (Warren et al. 1994; Fan et al. 2001b), or poor statistics (Chapter 3). The integrated luminosity of QSOs is sensitive to the location of the break, so an accurate notion of the break's location is essential to computations of total luminosity.

Because the updated fit for the LF parameters is little changed from the fit in Chapter 3, the conclusions drawn in that chapter are strengthened, not changed. The QSO contribution to the $z = 3$ H I ionizing UV radiation field remains at about 50% of the previously expected value, based on the local slope of $\beta_l = 1.64$; the contribution to the non-ionizing radiation field is about 8% of the contribution from LBGs. Recall, however, that the QSO luminosity is the primary radiation source at shorter wavelengths, such as those required to ionize He II; implications of these results are discussed below.

Our observations are in good agreement with a recent result from the Great Observatories Origins Deep Survey (GOODS) team (Cristiani et al. 2004), who report a substantial deficit of high-redshift ($3.5 \lesssim z \lesssim 5.2$) , medium-luminosity ($M_{1450} \approx -23$) QSOs. The comparison is against a PLE model, where a lower-redshift LF is evolved in luminosity to match SDSS bright-end results at high redshift. At $z > 4$, where they consider their photometric redshifts to be most reliable (and partially confirmed with spectroscopy), the authors report a 3σ disagreement with the PLE model, and note that a flattening of the high-redshift LF slope is required below the $M_{1450} \lesssim -26.5$ regime probed by SDSS.

Thus far, there have been few theoretical predictions about the faint-end slope. One of the few is due to Wyithe & Loeb (2003), who have modeled the QSO LF over a wide range of redshifts, by assuming that the SMBH accretion phase is self-regulating. They assume that a SMBH accretes at a constant fraction $\eta \approx 1$ of its Eddington luminosity, until its luminosity is enough to unbind the gas within its dynamical time. This self-regulated growth model predicts a steeper faint-end slope at high redshift; combined with the observed evolution of the bright-end slope, they predict the "break" to disappear at high redshift. This result, of course, is contrary to the observations presented here. The predicted steepening of the faint end is relatively mild in their model at $z \approx 3$; like the SDSS observations of the faint end, the LF shape evolution occurs primarily at $z \gtrsim 4$. At low redshifts, they attribute the break to a lack of efficient cooling, which makes it possible for low-mass AGN to unbind their gas.

Because the predicted slope is only slightly steeper at $z \approx 3$, only minor adjustments

to the Wyithe & Loeb (2003) model should be necessary to explain the observations. For comparison, other simulations of QSO evolution do not generally predict much faint-end evolution at $z \lesssim 3$. Kauffmann & Haehnelt (2000) have used semianalytic models of SMBH growth, assuming that accretion and the QSO phase occur as a result of major mergers. Several models for the accretion timescale $t_{\mathrm{acc}}(z)$ are attempted, and the model $t_{\mathrm{acc}}(z) = 1.0 \times 10^{7}(1+z)^{-1.5}$ Gyr is found to best reproduce the evolution of bright QSOs. Based on this model of the QSO lifetime, and the availability of gas in their simulations, the authors find that even at $z = 3$, the Eddington ratio is not identical for all QSOs; while bright QSOs are near-Eddington, the faintest in their simulations ($M_B = -22$) have Eddington ratios of about 0.1–0.5. [The Kauffmann & Haehnelt (2000) simulations also suggest that the faint-end slope can be flattened at $z \approx 3$ if cooling flows reach the black hole.] It is likely that if the Wyithe & Loeb (2003) model incorporated the luminosity-dependent Eddington ratio, instead of assuming $\eta \approx 1$ for all luminosities, the faint end slope would be substantially flattened, improving the agreement with our observations.

Granato et al. (2001) suggest that even though the most massive SMBHs grow rapidly and early, before their host galaxies, the situation is reversed for smaller holes. They propose that feedback from supernovae and accretion in smaller halos is capable of slowing down, and halting, both the QSO activity and star formation, leading to a correlation between the BH and stellar masses. In this scenario, LBGs are generally in the pre-QSO phase, undergoing strong star formation before QSO feedback begins. Such a prediction is consistent with the observations described above, and also with the results of Hosokawa (2004), who concludes that most $z \approx 3$ LBGs do not have SMBHs, provided mass accretion is the dominant process for SMBH growth. (If mergers and/or direct formation are important compared to accretion, the author cannot rule out SMBHs in most LBGs.)

The observations presented here also have implications for the state of the UV radiation field at $z \approx 3$, and in particular the reionization of He II. Fardal et al. (1998) present a good overview of results from four $z \approx 3$ QSOs where He II Lyman-α absorption is observed. The spectrum of $z = 2.9$ QSO HE 2347–4342 has shown strong variations in the ratio $\eta = N(\text{He II})/N(\text{H I})$, over the range 0.1–460 (Shull et al. 2004). Much of this variation, but not all, can be explained by the observed range of QSO spectral indices $0 < \alpha < 3$ in the UV. Shull et al. (2004) suggest a variety of explanations for the additional variation. One possibility is that fewer sources ionize He II at a given point in the IGM, resulting in

greater fluctuations in the He II continuum due to, essentially, Poisson statistics. Fardal & Shull (1993) showed, using traditional QSO LF models, that at $z \approx 2.5$, about 300–1000 QSOs lie within the "attenuation sphere" ($\tau \lesssim 1$) at each point in the IGM. However, the He II opacity is considerably higher, and the radius of the attenuation sphere in He II is only about 0.25 that of H I, about 34 physical Mpc (Shull et al. 2004). This reduces the number of sources to about 5–15, and Poisson statistics may become important. Shull et al. (2004) are not confident that this effect is a sufficient explanation for the η variation observed, and call for better simulations that include nonuniform filaments in the IGM, rather than spherical models.

Integrating the LF presented in this chapter, to 3 mag fainter than the power-law break for consistency with Fardal & Shull (1993), we find that the number of QSOs available to ionize He II is reduced by another factor of two, to 2–7. Obviously the Poisson statistics will result in even stronger fluctuations in the He II continuum than previously expected, and we believe that this may be a satisfactory explanation for the HE 2347–4342 observations.

Sokasian et al. (2002) also investigate the process of He II ionization. They use 3D radiative transfer equations and cosmological hydrodynamical simulations to model the process of reionization, and compare the results of the simulations (including simulated He II Lyman-α forest spectra) to UV observations. The ionizing sources for the simulations are QSOs; six different models for the QSO LF were employed. All six models were derived from the Pei (1995) model. Adjustable parameters include the QSO lifetime, minimum mass, beaming angle, hard-UV spectral index, and minimum $z = 0$ luminosity (LF truncation luminosity). Of particular interest is their model 5, which has a brighter truncation luminosity (by a factor of about 6) than the other models, and produced only 35% as many ionizing photons at $z = 2.75$ as the first four models. Model 6 produces a similarly low number of photons, by means of an unusually steep spectral index (2.3 vs. 1.8–1.9). Comparing the results of the simulations to observations, the authors find that model 5 best matches the observed mean optical depth at $z \approx 3$ and pronounce it their "best fit" model (although model 6, with the steep spectral index, also works fairly well).

The results of this chapter are quite consistent with the Sokasian et al. (2002) results. The flat faint-end slope decreases the ionizing photon count by about 50% compared to a Pei (1995) baseline model, comparable[3] to their model 5. Qualitatively, the flat slope

---

[3]No intermediate cases between 100% and 35% of the Pei (1995) photon counts were attempted in their

is similar to the "early truncation" approach of model 5: the QSO deficit comes at faint luminosities. The flat faint-end slope produces their photon deficit in a very natural way, without requiring an arbitrary LF truncation; with a flat slope, the integrated LF becomes less sensitive to the truncation luminosity.

In summary, we have measured the faint end of the $z \approx 3$ QSO LF over 6 mag of luminosity, and found the faint-end slope to be $\beta_l = 1.20$, substantially flatter than in the local universe. This result was unanticipated by theoretical predictions, but in combination with SMBH accretion models suggests that the QSO phase of low-mass holes was more recent than massive holes. The results describe here also serve to improve our understanding of the IGM at high redshift; the flat faint-end slope can serve to explain the strong fluctuations in helium-to-hydrogen column density ratios, and likely yields a better fit to the observed mean He II optical depth than the previously assumed LF shape. We believe that the improved understanding of the QSO LF will serve to improve future models of galaxy formation, SMBH accretion, and the IGM.

---

simulations.

Chapter 5

Reduction of LFC imaging data

5.1   Background

The Large-Format Camera[1] (LFC) is a 6-CCD mosaic imaging camera at the prime focus of the 200-inch Hale Telescope (hereafter P200) at Palomar Observatory. Providing a field of view 24 arcmin in diameter, the LFC offers a combination of collecting area and sky coverage that is useful for large imaging surveys. A description of the instrument (including its mechanical and electronic design, and its control and readout software) is provided by Simcoe (2003).

When the LFC was first delivered to the Observatory in October 1999, it was not clear how best to reduce the copius data that the instrument produced. For each exposure taken, the LFC control software, `mcdcom`, writes one FITS file for each CCD in the focal plane (e.g., `ccd.001.0.fits` through `ccd.001.5.fits`, followed by `ccd.002.0.fits` through `ccd.002.5.fits` for the next exposure). The most useful end-product from the data reduction would be a single, stacked image covering the whole LFC focal plane, derived from all 6 images from all of the exposures taken. Generally, the telescope would be offset slightly (dithered) between exposures, so as to fill in the 15 arcsec gap between adjacent CCDs.

The optical distortion of the images complicates this process. The plate scale (arcsec/pixel) of the CCD array increases by about 6% from the center of the field to the edge; see Figure 5.1. Over the large field of the LFC, this variation has substantial effects; if an astrometric solution were obtained naïvely based on the center of the field, errors of over

---

[1]The LFC was designed and built at Caltech by M. Metzger, R. Simcoe, J. Yamasaki, T. Small, and G. Arays.

40 arcsec would arise at the edges. Similarly, the distortion must be corrected before stacking dithered images; a shift of 30 arcsec corresponds to about 175 pixels at the center of the field. If the distorted images were simply shifted by 175 pixels prior to stacking, objects at the edge of the field would be out-of-register by 1.8 arcsec, because the 30 arcsec dither corresponds to only 165 pixels at the edge of the focal plane. Such an error in registration is much larger than the typical seeing FWHM, and is clearly unacceptable.

For reasons of expediency, many observers initially reduced LFC data by treating each CCD separately, rather than generating a single, complete mosaic. This approach may be satisfactory, especially if one is interested in a single object on a specific chip, and the object of interest is not near the edge of the focal plane. It was not, however, a satisfactory long-term solution to the problem of LFC data reduction.

A more satisfying approach has been developed, which is based on the IRAF `mscred`[2] package, which was originally developed for the reduction of data from the NOAO Mosaic camera. This approach meets the goal described above: The final data product is a stacked, cosmetically clean image of the entire LFC focal plane. It is a tangent-plane projected image with an astrometrically correct World Coordinate System (WCS) embedded in the FITS files, which allows a wide variety of astronomical software to translate between world coordinates (right ascension and declination) and logical coordinates (x and y pixel coordinates). This approach, which is described below, has permitted the rapid and successful reduction of LFC data for a survey of medium-luminosity $z \approx 3$ QSOs (Chapter 4) and a survey of $1.4 \lesssim z \lesssim 2.5$ star-forming galaxies (Steidel et al. 2004). It has become the *de facto* standard method of data reduction for the LFC user community at Caltech.

5.2 Suggestions for observing with LFC

Documentation and assistance for LFC observations is provided by Palomar Observatory. This section provides a few additional suggestions, borne of experience reducing LFC data.

It is better to have too much calibration data than too little. You should plan to obtain the following calibration data, for the best results in your data analysis:

- Bias exposures; some LFC chips have a bias ramp in the direction *perpendicular* to

---

[2]See, for example, `http://www.noao.edu/noao/noaodeep/ReductionOpt/frames.html` by B. Jannuzi, J. Claver, and F. Valdes.
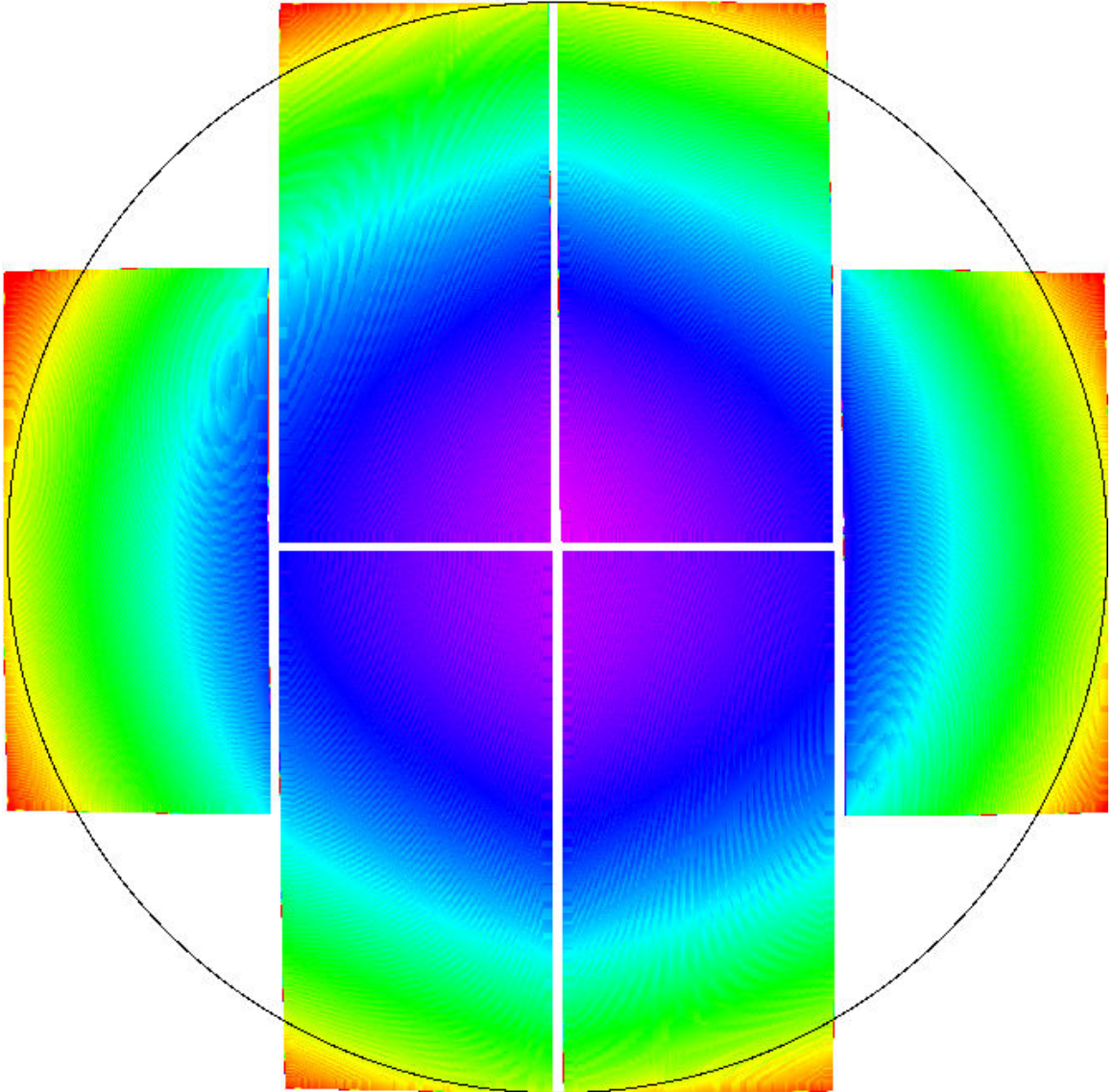
Figure 5.1 Map of the LFC plate scale. The scale ranges from 0.171 arcsec/pixel (purple) to 0.182 arcsec/pixel (red). The black circle is 24 arcmin in diameter. The small-scale structure in the map is a numerical artifact.

the overscan region. This ramp consequently cannot be fit using the overscan.

- Flat-field exposures; dome flats appear to work well in g' and redder bands. Twilight sky flats work well in u'. The LFC shows a pronounced "Aztec" flat-field pattern, especially in the blue. Taking dome flats of two different exposure times, in the same filter, will be helpful if you wish to construct a new bad pixel mask (see §5.4).

- Astrometric field exposures; an astrometric (or distortion) solution is provided with the LFC reduction software, but you may wish to be prepared to create a new solution—especially if the instrument has been worked on since the solution was created. Any field rich in USNO stars will suffice; point the telescope at the Galactic plane (at the start or end of the night, depending on time of year), focus, and expose for 30–60 seconds in g' or r'.

Naturally, you should also take standard star exposures, linearity sequences, and airmass sequences as befit your science program. Plots of linearity curves are available in the LFC documentation at the telescope, to aid with flat-field and standard star exposures.

The LFC's autoguider CCD sits in the instrument focal plane, behind the filter. During u' observations, especially at high galactic latitude, it can be difficult to find a satisfactory guide star. The `lfc-gsc.pl` program takes as input a list of LFC pointings, queries the HST Guide Star Catalog over the Internet, and produces a list of candidate guide stars. Warnings are produced for stars with faint J (photographic) magnitudes, or with positions near or beyond the edge of the guider CCD. If there are no "clean" stars in the list, the position may have to be adjusted slightly to obtain a guide star. The program displays the stars' offsets, relative to the center of the guider CCD, to assist in this process. The `lfc-gsc.pl` program can be obtained as described in §5.3.

5.3   Installing the LFC reduction software

The LFC reduction software described here is available from:

`http://www.pobox.com/~mph/lfcred/`

You can download the latest version, which includes a more consise set of instructions (called `GUIDE`), various ancillary scripts mentioned throughout this document, and the essential IRAF tasks and data files.

The software requires the `mscred` package for IRAF. If your installation does not offer this package, you can download the package from NOAO at:

`ftp://iraf.noao.edu/iraf/extern-v212/mscred/`

Installation instructions are included.

5.4   Assembling your raw images

As previously noted, `mcdcom` writes a separate FITS file for each of the LFC's CCDs. The `mscred` package is instead designed to work with Multiple-Extension FITS files (MEFs). A MEF is a FITS file which is capable of storing multiple images, which are called "extensions." Each extension has its own image headers, in addition to the image data. In the `mscred` model, the first MEF extension has only header data for the file. The extensions are numbered starting from zero, and this extension is referred to as `image.fits[0]` in IRAF. The header data in the `[0]` extension is common to all of the CCDs, and may include the exposure time, date of exposure, telescope pointing, filter, and similar global quantities. The extensions for the six CCDs (in the LFC case) then follow.

Most steps in the reduction process require the user to be in the `mscred` package in IRAF, which is accomplished simply by typing "`mscred`" at the IRAF prompt. Once inside `mscred`, the raw LFC data is assembled into MEFs using the `lfcassemble` task. The only parameter is a list of root names for the input images. If your raw data files are `ccd.001.0.fits` ... `ccd.001.5.fits`, `ccd.002.0.fits` ... `ccd.002.5.fits`, your list of root names is `ccd.001,ccd.002`. The output of `lfcassemble` would then be two MEFs, `ccd.001.fits` and `ccd.002.fits`. Since the `[0]` extension is used for global data, the six CCD images are found in extensions `[1]` through `[6]`. Because `mcdcom` and the LFC documentation refer to the CCDs as 0 through 5, this can be slightly confusing. As a convenience, `lfcassemble` adds symbolic names `lfc0` through `lfc5` to the MEFs it produces. Thus, "Chip 0" of the first exposure can be accessed as either `ccd.001.fits[1]` or `ccd.001.fits[lfc0]`. The `lfcassemble` task makes a few additional modifications to the output images:

- It adds `DETSEC` headers to each extension; these headers indicate where each CCD lies in a large "virtual" focal plane, allowing `mscdisplay` to display the entire mosaic

array correctly, for quick-look viewing. The DETSEC headers have no effect on the final data product.

- It converts the data from true 16-bit unsigned data to 16-bit signed, with a BZERO offset. This is necessary to conform to the FITS standard, which does not provide for a 16-bit unsigned data type.

- It copies certain headers (IMAGETYP, FILTER) to the [0] header.

- It converts the telescope pointing headers from "string" to "real."

- It adds appropriate DATASEC headers, to indicate the image sections that contain valid data. This depends on the LFC binning pattern, which is detected automatically for the popular 1x1 or 2x2 binning patterns.

- It adds appropriate BPM headers that point to bad pixel masks. This also depends on the binning pattern. Bad pixel masks are provided with the software, as described in §5.3. Users may wish to create up-to-date masks using a task like ccdmask; an image that is the ratio of two flatfield images, of different exposure times but in the same filter, works best for this purpose.

- It adds a XTALKFIL header that points to a crosstalk correction file. In the LFC, measurable crosstalk occurs between lfc0 and lfc1, and between lfc2 and lfc3. A crosstalk correction file is provided, or a new one may be created using the xtcoeff task.

With MEFs in hand, you may inspect images with mscdisplay. This task works like the normal display task, but shows all of the extensions in the MEF, in (approximately) their correct positions and orientations.

5.5 Basic image processing

We will now proceed to do basic image processing on the MEFs, such as bias subtraction and flat-fielding. The mscred package includes a version of the ccdproc task which works on MEFs. For organizational purposes, it is helpful at this point to make separate subdirectories for each field observed (and for the various calibrations), and within those

subdirectories, separate subdirectories for each filter employed. We will begin by combining the bias frames. The first step is to trim and overscan-subtract them using `ccdproc`; example settings are shown in Figure 5.2. After processing, the bias exposures can be combined using the `mscred` version of `zerocombine`, as shown in Figure 5.3; an output image called `Zero.fits` is assumed hereafter.

With `Zero.fits` in hand, we can now process each filter's flat-field exposures in a similar fashion. First, the flat-field exposures are processed using `ccdproc`; however, we now set `zerocor=yes` and `zero=Zero.fits` to bias-subtract the images. They may then be combined with `flatcombine`, with settings similar to those used for `zerocombine`. The exposures should typically be mode-scaled with `scale=mode`, and a reasonably small image section specified for the statistics, e.g. `statsec=[1000:1100,1000:1100]`. If stars are present in twilight flats, `combine=median` or more aggressive rejection settings may be required. Output filenames similar to `Flatg.fits` (for g' flats) are assumed in this discussion.

The science exposures may now be processed with `ccdproc`; in addition to the bias-correction settings that we previously turned on, we now set `flatcor=yes` and `flat=Flat*`. After running `ccdproc` on the science images, `mscdisplay` can be used to verify that the flat-field correction has been successful.

5.6 Removing cosmic rays

There are various IRAF tasks that are designed to detect and remove cosmic rays from imaging data (`xzap`, `qzap`, `lacos_im`, etc.). Most observers have a favorite, and this document will not prescribe any one in particular. In general, though, these tasks are all incapable of operating on MEFs. Therefore, you will need to split your MEFs back into individual images in order to run a cosmic ray "zapper." The `mscsplit` task is designed for this purpose. Its use is straightforward, as shown in Figure 5.4. The filename list should consist simply of the MEF filenames, with "`.fits`" omitted: `ccd.001`, `ccd.002`, etc. The output filenames will then be `ccd.001_0.fits` through `ccd.001_6.fits`, `ccd.002_0.fits` through `ccd.002_6.fits`, etc.

Recall that the "`_0.fits`" file for each exposure corresponds to the `[0]` extension, which contains no image data. Therefore, the cosmic ray zapper should only be run on the other 6 files from each exposure. The cosmic ray zapper should produce a cosmic ray mask (usually

```
PACKAGE = mscred
   TASK = ccdproc

images  =                    @bias  List of Mosaic CCD images to process
(output =                       ) List of output processed images
(bpmasks=                       ) List of output bad pixel masks
(ccdtype=                       ) CCD image type to process
(noproc =                     no) List processing steps only?

(xtalkco=                    yes) Apply crosstalk correction?
(fixpix =                     no) Apply bad pixel mask correction?
(oversca=                    yes) Apply overscan strip correction?
(trim   =                    yes) Trim the image?
(zerocor=                     no) Apply zero level correction?
(darkcor=                     no) Apply dark count correction?
(flatcor=                     no) Apply flat field correction?
(sflatco=                     no) Apply sky flat field correction?
(split  =                     no) Use split images during processing?
(merge  =                     no) Merge amplifiers from same CCD?

(xtalkfi=              !xtalkfil) Crosstalk file
(fixfile=                  !bpm) List of bad pixel masks
(saturat=                 INDEF) Saturated pixel threshold
(sgrow  =                     0) Saturated pixel grow radius
(bleed  =                 INDEF) Bleed pixel threshold
(btrail =                    20) Bleed trail minimum length
(bgrow  =                     0) Bleed pixel grow radius
(biassec=               !biassec) Overscan strip image section
(trimsec=               !trimsec) Trim data section
(zero   =                       ) List of zero level calibration images
(dark   =                       ) List of dark count calibration images
(flat   =                       ) List of flat field images
(sflat  =                       ) List of secondary flat field images
(minrepl=                    0.) Minimum flat field value

(interac=                     no) Fit overscan interactively?
(functio=                    leg) Fitting function
(order  =                      2) Number of polynomial terms or spline pieces
(sample =                      *) Sample points to fit
(naverag=                      1) Number of sample points to combine
(niterat=                     10) Number of rejection iterations
(low_rej=                    3.) Low sigma rejection factor
(high_re=                    3.) High sigma rejection factor
(grow   =                    0.) Rejection growing radius
```

Figure 5.2 Example parameter set for processing bias exposures with `ccdproc`.

```
PACKAGE = mscred
   TASK = zerocombine

input   =                    @bias  List of zero level images to combine
(output =                    Zero)  Output zero level name
(combine=                 average)  Type of combine operation
(reject =                  minmax)  Type of rejection
(ccdtype=                       )  CCD image type to combine
(process=                     no)  Process images before combining?
(delete =                     no)  Delete input images after combining?
(scale  =                   none)  Image scaling
(statsec=                       )  Image section for computing statistics
(nlow   =                      1)  minmax: Number of low pixels to reject
(nhigh  =                      1)  minmax: Number of high pixels to reject
(nkeep  =                      1)  Minimum to keep (pos) or maximum to reject (neg)
(mclip  =                    yes)  Use median in sigma clipping algorithms?
(lsigma =                     3.)  Lower sigma clipping factor
(hsigma =                     3.)  Upper sigma clipping factor
(rdnoise=                     0.)  ccdclip: CCD readout noise (electrons)
(gain   =                     1.)  ccdclip: CCD gain (electrons/DN)
(snoise =                     0.)  ccdclip: Sensitivity noise (fraction)
(pclip  =                   -0.5)  pclip: Percentile clipping parameter
(blank  =                     0.)  Value if there are no pixels
```

Figure 5.3 Example parameter set for combining bias exposures with `zerocombine`.

```
PACKAGE = mscred
   TASK = mscsplit

input   =            @mscsplit.in  List of input MEF files
(output =                       )  List of output root names
(mefext =                  .fits)  MEF filename extension
(delete =                     no)  Delete MEF file after splitting?
(verbose=                    yes)  Verbose?
```

Figure 5.4 Example parameter set for splitting MEFs into individual images with `mscsplit`.

in the form of a ".pl" pixel-list file for each image). We will use these masks later, to ensure that pixels affected by cosmic rays are excluded from the stacked image.

After the cosmic ray zapper has finished, the individual images should be re-combined into MEFs using mscjoin, which works much like mscsplit in reverse. If the zapper has produced output images with new names, remember to copy the "_0.fits" files to the appropriate new names before attempting the re-join the files.

5.7   Embedding and refining the World Coordinate System

At this point, we wish to embed a World Coordinate System (WCS) into the MEFs. The WCS provides a mathematical relationship between world coordinates (typically J2000 right ascension and declination) and logical coordinates (pixel x and y coordinates). Because the plate scale of the LFC varies with position, the WCS contains non-linear terms. These terms are stored in a file, such as lfc-gprime.db which is included with the reduction software. This solution was obtained in August 2002[3]. The same solution can be used for either the 1x1 or 2x2 binning pattern, and solutions generated in any filter can be used on data in any other filter. While the filter thickness affects the plate scale of the image, we will fit for that effect in a later step.

The solution is applied to the MEFs with the mscsetwcs task, whose use is straightforward. Example parameters are shown in Figure 5.5. The task simply converts the stored solution from the database file into the appropriate WCS image headers, and sets the reference point of the solution to be the RA and DEC specified by the telescope pointing headers.

Naturally, the telescope pointing is not perfect—certainly not good enough for our desired astrometric accuracy of well under an arcsecond. Thus, the WCS in the images is only a starting point. The msccmatch task will allow us to refine this WCS, by fitting for a pointing correction, as well as a plate scale change. It is normally used in conjunction

---

[3]If work has been performed on the LFC focal plane, a new solution may be required. A solution can be generated in any field with sufficient astrometric reference stars (usually a few hundred USNO–A2 stars); see §5.2. The msctpeak task can be used to generate the solution; see http://iraf.noao.edu/projects/ccdmosaic/astrometry/astrom.html by F. Valdez for details. The tnx geometry with all [xy][xy]order=4, [xy]xterms=half has generally provided a good fit for the LFC. Using mscsetwcs to apply the out-of-date solution to the new calibration field, as described in this section, provides an easier starting point than identifying stars by hand; this allows you to start at the "Updating the WCS" step of Valdez's instructions.

with `mscgetcatalog`, which queries the USNO–A2 catalog over the Internet, to obtain a list of reference stars. The `msccmatch` task is normally run interactively, and a fit is performed using the normal IRAF fitting routines ("d" to delete points, "f" to re-fit the remaining points, and so forth). An example parameter set is shown in Figure 5.6. The `search` and `rsearch` parameters should be larger than the largest plausible errors in the telescope pointing and LFC position angle, respectively. The position angle of LFC is usually accurate to much better than a degree. In some cases, `msccmatch` fails (probably due to it mis-identifying a star in its coarse centering pass). This results in very few catalog stars being centroided successfully. Perturbing the `nsearch`, `search`, and `rsearch` parameters can "bump" `msccmatch` toward a successful solution.

The RMS errors that `msccmatch` reports for the fit should generally be in the neighborhood of 0.3 arcsec. These values represent the RMS errors of the individual USNO stars, and reflect the uncertainty of individual positions in that catalog. The overall accuracy of the solution is likely better than the stated RMS errors.

5.8 Tangent-plane projecting the images

With accurate WCS information in the MEFs, we are nearly prepared to tangent-plane project the images. After tangent-plane projection with `mscimage`, each exposure will be a single, normal FITS file (not a MEF). The pixels will be resampled onto a uniform grid, where each pixel in the image has the same plate scale; this eliminates the distortion in the images. Furthermore, by using the correct `mscimage` parameters, all of the images in a given field will be projected onto the same plate scale, with the same tangent point, and can be placed into pixel register using only integer pixel shifts.

When we tangent-plane project the images, we want to project their bad-pixel masks in the same way, so that we know which resampled pixels had contributions from bad pixels in the original image. These pixels can then be excluded from the final stacked image. The MEFs already have `BPM` headers pointing to a bad pixel map, but the locations of cosmic rays should be added to each image's bad pixel map. Using `awk`, Perl, or your shell, you can generate an IRAF `cl` script to add these masks together, and update the `BPM` headers; see Figure 5.7 for an example.

Some thought must be applied to the running of `mscimage`. It allows you to specify

```
PACKAGE = mscred
   TASK = mscsetwcs

images  =            @mscjoin.out Mosaic images
database=           lfc-gprime.db WCS database
(ra     =                     ra) Right ascension keyword (hours)
(dec    =                    dec) Declination keyword (degrees)
(equinox=                equinox) Epoch keyword (years)
(ra_offs=                    0.) RA offset (arcsec)
(dec_off=                    0.) Dec offset (arcsec)
```

Figure 5.5 Example parameter set for embedding a WCS into MEFs with mscsetwcs.

```
PACKAGE = mscred
   TASK = msccmatch

input   =           @mscjoin.out  List of input mosaic exposures
coords  =       !mscgetcat $I $C  Coordinate file (ra/dec)
(outcoor=                      )  List of updated coordinate files
(usebpm =                   yes)  Use bad pixel mask?
(nsearch=                    51)  Maximum number of positions to use in search
(search =                   20.)  Translation search radius (arcsec)
(rsearch=                   0.5)  Rotation search radius (deg)
(nfit   =                     4)  Min for fit (>0) or max not found (<=0)
(rms    =                    2.)  Maximum fit RMS to accept (arcsec)
(maxshif=                    3.)  Maximum centering shift (arcsec)
(fitgeom=               general)  Fitting geometry
(reject =                    3.)  Fitting rejection limit (sigma)
(update =                   yes)  Update coordinate systems?
(interac=                   yes)  Interactive?
(fit    =                   yes)  Interactive fitting?
(verbose=                   yes)  Verbose?
(listcoo=                    no)  List centered coordinates in verbose mode?
(graphic=               stdgraph) Graphics device
(cursor =                      )  Graphics cursor
accept  =                   yes   Accept solution?
```

Figure 5.6 Example parameter set for refining a WCS with msccmatch.

a "reference image" for the resampling; the output image will have the same plate scale and tangent point as the reference image. These are helpful properties for images that will be stacked together, or otherwise placed in pixel register (for certain types of multi-color photometry, for example). However, it would be a bad idea to use one image as a reference for another image which is in a different part of the sky; the tangent-plane projection only works well near the tangent point. An example follows:

Suppose we have imaged two fields, Q1812 and Q2001, which are well separated on the sky; each of them was imaged in u', g', and r', with several exposures in each. A standard star was also observed in each filter. A reasonable course of action would be to start in the subdirectory containing the Q1812 r' data, and run `mscimage` on all of those MEFs (all at once), with `referen=""`. The task will select a reasonable plate scale and tangent point from the first MEF, and use that as the reference for all of the MEFs resampled at that time. Then, in the Q1812 g' and u' subdirectories, run `mscimage` on those MEFs, but specify as the `referen` any of the Q1812 r' `mscimage` output images. This ensures that all of the Q1812 data will be ready to stack and register.

Then, in the Q2001 r' directory, again run `mscimage` on all the MEFs, with `referen=""`; we do not want to have the same tangent point as the Q1812 projections. Continue with the g' and u' data, but use a Q2001 r' image as the `referen` image. Then, treat the standard star images in the same way (r' first, then using one of those images for g' and u').

An example parameter set for `mscimage` is shown in Figure 5.8. Note that `referen=""` in this example. The `poly5` interpolant generally works well, but smooths the image to a certain extent. The `sinc` interpolants (e.g. `sinc11`) better preserve pixel statistics, but the effect of a bad pixel can be distributed over a much larger area, and "ringing" artifacts are common around bad columns, saturation trails, and so forth. Note also that `fluxcon=no`; a justification for this setting is provided in §5.11.3.

5.9   Sky subtracting the projected images

In general, each exposure will have a different background (or sky) level. The background must be subtracted before stacking the exposures, or else discontinuities in the sky level will be present in the stack (since certain regions are imaged only in a subset of the exposures, due to chip gaps, etc.). If the sky is reasonably uniform, `imsurfit` in `residual` mode

usually works well. An example parameter set is shown in Figure 5.9. Note that with the median box set to 1x1, `imsurfit` will use iterative sigma-clipping to perform the fit. Fit orders of `[xy]order=2` or `3` (linear or quadratic) are generally has high as one should go to avoid ill-constrained fits. In the example, a "sections" file is used to specify the region of good data; since the LFC has a cruciform focal plane, defining the good data region is essential. The "sections" file can be created by inspecting an `mscimage` output image, and identifying the coordinates of three rectangles that cover the imaged region.

In some cases, the low-order `imsurfit` fits will not provide satisfactory sky subtraction; scattered light from stars near the edge of the image, for example, can produce strong background gradients that vary from one exposure to the next. Median-filtered versions of the images can be constructed with `fmedian` to model the background, and then subtraced using `imarith`. Median filtering is a rather slow process, and it can introduce negative "halo" artifacts around bright stars, but it is quite effective at dealing with difficult backgrounds. An example parameter set can be found in Figure 5.10. The median box size may be tweaked as desired, to provide a balance between object removal and effective subtraction.

5.10   Stacking the projected images

The `combine` task will be used to stack the final images. Before stacking, it is generally necessary to scale the exposures so that all objects have the same flux (in counts) in each exposure. Normally, a "reference" exposure is selected; this exposure should be one taken under photometric conditions, and preferably at low airmass. A multiplicative factor is determined for each other exposure, to scale it to the reference exposure. The scale factors are provided as an input to `combine`.

The determination of the scale factors is beyond the scope of this document, and is not peculiar to LFC data reduction. Good results have been obtained by using Sextractor[4] to produce a catalog for each exposure, with the magnitude and WCS coordinates for each object included in the catalog. The objects can then be matched based on WCS coordinates, and a scale factor determined by fitting for a magnitude zeropoint shift between the reference and other catalogs.

Our tangent-plane projected images have valid bad pixel masks. These indicate which

---

[4]Source Extractor by E. Bertin, available from `http://terapix.iap.fr/rubrique.php?id_rubrique=91`.

parts of the projected image should not be used, because of cosmic rays, CCD defects, or non-illumination (chip gaps, etc.). Since only valid pixels will be combined, the exposures can be averaged, rather than median-combined, for optimal signal-to-noise. If the exposures were taken under very different conditions, a "weights" file should be constructed in addition to the "scales" file. The weights should reflect the relative SNR^2 of the images. The "signal" can be determined from the scale factors, and the noise from measurements of the sky RMS (preferably from the non-resampled MEFs). If the images are of different exposure times, but observing conditions remained similar, the exposure time can be used directly in the "weights" file.

The `combine` task will shift the exposures appropriately to bring them in register, provided `offsets=wcs` is set. It will *only* perform shifts, not rotations, scalings, or other transformations. This is why it was essential in §5.8 to make proper use of reference images.

Example parameters for `combine` are shown in Figure 5.11, and an example of the final product is shown in Figure 5.12. The stacked images should be carefully inspected. Doubled images of stars suggest a problem in the WCS; this may be due to a bad solution in `msccmatch`. Alternatively, if a new solution was created using `msctpeak`, it may be ill-constrained at the edges of one or more chips, resulting in a star being projected onto different world coordinates depending on which chip it was imaged on. Object photometry in the stacked image should be compared to the reference exposure for consistency. Once the standard star exposures are reduced in the same way as the science images, a photometric zeropoint can be determined, and adjusted to reflect the exposure time and airmass of the reference exposure. That zeropoint should then be valid for the stacked exposure as well.

For various reasons, including multicolor photometry, it may be convenient to bring the different filters' stacks into pixel register. If the recommendations in §5.8 were followed, all of the stacks should differ only by an integer shift. The `sregister` task can be used to register them based on their world coordinate systems. One stacked image is chosen as the "reference," and the others are registered to it. An example paramter set is shown in Figure 5.13. With `fitgeom=shift`, and the shift known to be an integer, the parameters concerning orders and interpolants have no bearing on the output. The `xmin`, `xmax`, `ymin`, and `ymax` parameters should reflect the size of the reference image.

5.11 Technical notes

5.11.1 Applicability to other instruments

The approach to data reduction described above is hardly unique to LFC; the `mscred` package was originally written for use with NOAO Mosaic, and can be extended to other mosaic imaging systems. D. Kaplan has adapted the `lfcassemble` task for use with the blue side of the Low Resolution Imaging Spectrograph (LRIS; Oke et al. 1995; Steidel et al. 2004) at the W. M. Keck Observatory. Since LRIS is often used at arbitrary position angles, §5.11.2 may be of interest to users.

5.11.2 Rotating solutions

An astrometric solution database file, such as `lfc-gprime.db`, can only be used directly for data taken at the same position angle (PA) as the calibration data that was used to create the solution. This is of little consequence for LFC observers today; the instrument is always installed in the same orientation. But in the early days of the LFC, only 3 or 4 CCDs were installed, and the instrument could be installed with the long axis running north-south or east-west, as befit the observations. Also, as mentioned in §5.11.1, LRIS observations are easily made at any position angle.

Thus, it is useful to have a mechanism for rotating the solution in the database. A purely mathematical approach, based on the direct manipulation of the coefficients in the file, is difficult, because many of the terms pertain to polynomial fits in x and y, rather than in a polar coordinate system. There is a pragmatic approach, however, that works well.

The approach needs an existing solution, at a known PA, and a "scratch" image from the same instrument. The "scratch" image can be anything (a bias exposure, dome flat, science image) at any PA. Use `mscsetwcs` to apply the existing solution to the scratch image. Then, use any programming language to construct a file with x and y coordinates on each line, spanning the CCD size in a grid. Here is an example in Perl, spanning a 2048x2551 LRIS–B CCD with a grid spacing of 30 pixels:

```
for ($i=10; $i<2048; $i+=30) {
        for ($j=10; $j<2551; $j+30) {
                print "$i $j\n";
```

```
                    }
            }
```

The grid spacing is not critical. Now, start with the first CCD of the array, and use `wcsctran` to convert these pixel coordinates to world coordinates, via the original WCS; example parameters are shown in Figure 5.14. Note that the output format should be "`%f %f`" to obtain output in decimal degrees of RA and DEC. Create a file consisting of the x, y, RA, and DEC coordinates (e.g. "`paste grid.xy grid.world > rotate.in`"). Obtain the `rotatethepodhal.pl` program (see §5.3), and edit it to reflect the position angles of the existing and new solutions. Also, edit it to reflect the RA and DEC (in decimal degrees) of the scratch image; these can usually be copied from the image headers. Use the `rotate.in` file as input to this program, and store its output in a new file (e.g. "`./rotatethepodhal.pl < rotate.in > rotate.out`"). The output file contains the same x and y grid positions, and new RA and DEC positions obtained by rotating the old RA and DEC about the provided pointing center, by an angle equal to the difference in position angles.

The output file can be used as input to `ccmap` to generate a new solution database file. Example parameters are shown in Figure 5.15. The `solutio` parameter should match the symbolic name for the CCD you're working on (e.g. `lfc0` through `lfc5` for LFC reduction with `lfcassemble`; `LRISB1` or `LRISB3` for LRIS–B reduction with D. Kaplan's software). The reference point (`refpoint, latref, lngref`) should be explicitly set to the telescope pointing coordinates that you entered into `rotatethepodhal.pl`. The order of the fits should be the same as in the existing solution. Since `ccmap` is fitting a previous fit, not real data, the residuals should be nearly zero (they will not be exactly zero due to rounding errors).

Repeat the procedure for each additional CCD in the mosaic; write the `ccmap` solution to the same file, but update the `solutio` parameter to reflect the CCD you're working on.

This method has worked well for rotating LRIS solutions to arbitrary position angles. A caveat is that the telescope pointing coordinates must quite accurately reflect the sky coordinates of the instrument's rotation center. Small errors in these coordinates will be corrected in the `msccmatch` task (§5.7), but large errors may result in a failure to centroid.

5.11.3 `fluxcon=no`: A justification

In §5.8, we resampled distorted images to produce tangent-plane projections. The `mscimage` setting `fluxcon=no` was proposed; the description for this parameter is, "Preserve flux per unit area?" Specifically, if this parameter is set to "`yes`," the task will preserve counts/arcsec^2.

Consider a hypothetical instrument, with a certain plate scale in the center of the field. At the edge of the field, the linear plate scale increases by a factor of $\sqrt{2}$, so that each pixel sees a solid angle that's twice as large as in the center. Two identical stars (point sources) are imaged at the center and edge of the field. Assume that the star produced 1,000 counts during the exposure. At the edge of the field, the star takes up fewer pixels, due to the change in plate scale, but the total star counts are the same for both stars (since the QE and throughput are not affected by distortion). Assume also that the sky level at the center of the field is 100 counts per pixel; at the edge of the field, the background will be 200 counts per pixel, because each pixel "sees" more of the sky at the edge than the center.

Now, consider the process of data reduction. We must flat-field the data. During the run, we would have produced a flat-field image, using a dome flat or twilight illumination. If the flat-field image has 10,000 counts per pixel in the center of the field, it will have 20,000 counts per pixel at the edge, because of the effect described above. Let us normalize the flat-field image using the central value, and divide the science image by the normalized flat-field image. Now, the sky level of the science image is uniform, at 100 counts per pixel. The central star continues to have 1,000 total counts, but at the edge of the field we've divided the image by a factor of 2, and the star there has been reduced to 500 counts (despite having the same true flux as the central star).

Suppose we now use `mscimage` to tangent-plane project the image with `fluxcon=yes`, with an output plate scale identical to the central plate scale of the original image. The central star will undergo essentially no resampling, and will still have 1,000 total counts on a 100 count/pixel background. The edge star will be resampled; its image occupies fewer pixels than the central star in the original image, but the same solid angle. Since `fluxcon=yes` preserves counts per solid angle, the edge star will continue to have half as many counts as the central star. Since it actually has the same flux, this approach will clearly play havoc with the image's photometry. A non-uniform sky background will also

result, since the background in the original image is uniform per pixel, instead of per unit solid angle.

If we instead use `fluxcon=no`, `mscimage` will also scale the output counts by the Jacobian of the transformation, which will increase the edge star's total counts back up to 1,000, the same as the central star. Likewise, the sky background will be increased at the edges, resulting in a uniform background in the output image.

```
imarith crmask_ccd.001_1.pl + chip0.bad.pl finalmask_ccd.001_1.pl
hedit ccd.001[lfc0] BPM finalmask_ccd.001_1.pl show+ update+
imarith crmask_ccd.001_2.pl + chip1.bad.pl finalmask_ccd.001_2.pl
hedit ccd.001[lfc1] BPM finalmask_ccd.001_2.pl show+ update+
...
imarith crmask_ccd.001_6.pl + chip5.bad.pl finalmask_ccd.001_6.pl
hedit ccd.001[lfc5] BPM finalmask_ccd.001_6.pl show+ update+

imarith crmask_ccd.002_1.pl + chip0.bad.pl finalmask_ccd.002_1.pl
hedit ccd.002[lfc0] BPM finalmask_ccd.002_1.pl show+ update+
...
imarith crmask_ccd.002_6.pl + chip5.bad.pl finalmask_ccd.002_6.pl
hedit ccd.002[lfc5] BPM finalmask_ccd.002_6.pl show+ update+
```

Figure 5.7 Example IRAF `cl` script for merging the bad pixel and cosmic ray masks.

```
PACKAGE = mscred
   TASK = mscimage

input   =          @mscimage.in  List of input mosaic exposures
output  =         @mscimage.out  List of output images
(format =                image)  Output format (image|mef)
(pixmask=                  yes)  Create pixel mask?
(verbose=          )_.verbose)  Verbose output?


                                 # Output WCS parameters
(wcssour=                image)  Output WCS source (image|parameters)
(referen=                    )  Reference image
(ra     =                INDEF)  RA of tangent point (hours)
(dec    =                INDEF)  DEC of tangent point (degrees)
(scale  =                INDEF)  Scale (arcsec/pixel)
(rotatio=                INDEF)  Rotation of DEC from N to E (degrees)


                                 # Resampling parmeters
(blank  =                  0.)  Blank value
(interpo=                poly5)  Interpolant for data
(minterp=                poly5)  Interpolant for mask
(boundar=             constant)  Boundary extension
(constan=                  0.)  Constant boundary extension value
(fluxcon=                   no)  Preserve flux per unit area?
(ntrim  =                    8)  Edge trim in each extension
(nxblock=                INDEF)  X dimension of working block size in pixels
(nyblock=                INDEF)  Y dimension of working block size in pixels


                                 # Geometric mapping parameters
(interac=                   no)  Fit mapping interactively?
(nx     =                   10)  Number of x grid points
(ny     =                   20)  Number of y grid points
(fitgeom=              general)  Fitting geometry
(xxorder=                    6)  Order of x fit in x
(xyorder=                    6)  Order of x fit in y
(xxterms=                 half)  X fit cross terms type
(yxorder=                    6)  Order of y fit in x
(yyorder=                    6)  Order of y fit in y
(yxterms=                 half)  Y fit cross terms type
```

Figure 5.8 Example parameter set for tangent-plane projecting a MEF with mscimage.

```
PACKAGE = imfit
   TASK = imsurfit

input   =                 @ims.in  Input images to be fit
output  =                @ims.out  Output images
xorder  =                       2  Order of function in x
yorder  =                       2  Order of function in y
(type_ou=             residual)  Type of output (fit,residual,response,clean)
(functio=             legendre)  Function to be fit (legendre,chebyshev,spline3)
(cross_t=                  yes)  Include cross-terms for polynomials?
(xmedian=                    1)  X length of median box
(ymedian=                    1)  Y length of median box
(median_=                  50.)  Minimum fraction of pixels in median box
(lower  =                  2.5)  Lower limit for residuals
(upper  =                  2.5)  Upper limit for residuals
(ngrow  =                    2)  Radius of region growing circle
(niter  =                    5)  Maximum number of rejection cycles
(regions=             sections)  Good regions (all,rows,...,sections,...)
(rows   =                    *)  Rows to be fit
(columns=                    *)  Columns to be fit
(border =                   50)  Width of border to be fit
(section=             sections)  File name for sections list
(circle =                     )  Circle specifications
(div_min=                INDEF)  Division minimum for response output
```

Figure 5.9 Example parameter set for background-subtracting images with `imsurfit`.

```
PACKAGE = imfilter
   TASK = fmedian

input   =                @ims.out  Input images to be filtered
output  =            @fmedian.out  Output images
xwindow =                     151  X window size of median filter
ywindow =                     151  Y window size of median filter
(hmin   =                  -32768)  Minimum histogram bin
(hmax   =                   32767)  Maximum histogram bin
(zmin   =                -32768.)  Pixel value corresponding to hmin
(zmax   =                 32767.)  Pixel value corresponding to hmax
(zloreje=                  INDEF)  Lowside pixel value cutoff
(zhireje=                  INDEF)  High side pixel value cutoff
(unmap  =                    yes)  Unmap the digitized values ?
(boundar=                   refl)  Boundary (constant,nearest,reflect,wrap)
(constan=                     0.)  Constant for boundary extension
(verbose=                    yes)  Print messages about actions taken by the task
```

Figure 5.10 Example parameter set for background-subtracting images with `fmedian`.

```
PACKAGE = mscred
   TASK = combine

input   =          @imsurfit.out  List of images to combine
output  =          Q1234-r.fits  List of output images
(headers=                      ) List of header files (optional)
(bpmasks=                      ) List of bad pixel masks (optional)
(rejmask=                      ) List of rejection masks (optional)
(nrejmas=                      ) List of number rejected masks (optional)
(expmask=                      ) List of exposure masks (optional)
(sigmas =                      ) List of sigma images (optional)

(ccdtype=                      ) CCD image type to combine (optional)
(amps   =                    no) Combine images by amplifier?
(subsets=                    no) Combine images by subset?
(delete =                    no) Delete input images after combining?

(combine=               average) Type of combine operation
(reject =                  none) Type of rejection
(project=                    no) Project highest dimension of input images?
(outtype=                  real) Output image pixel datatype
(outlimi=                      ) Output limits (x1 x2 y1 y2 ...)
(offsets=                   wcs) Input image offsets
(masktyp=               goodval) Mask type
(maskval=                    0.) Mask value
(blank  =                    0.) Value if there are no pixels

(scale  =               @scales) Image scaling
(zero   =                  none) Image zero point offset
(weight =              @weights) Image weights
(statsec=                      ) Image section for computing statistics

(Remaining parameters do not matter when reject=none)
```

Figure 5.11 Example parameter set for stacking exposures with combine.

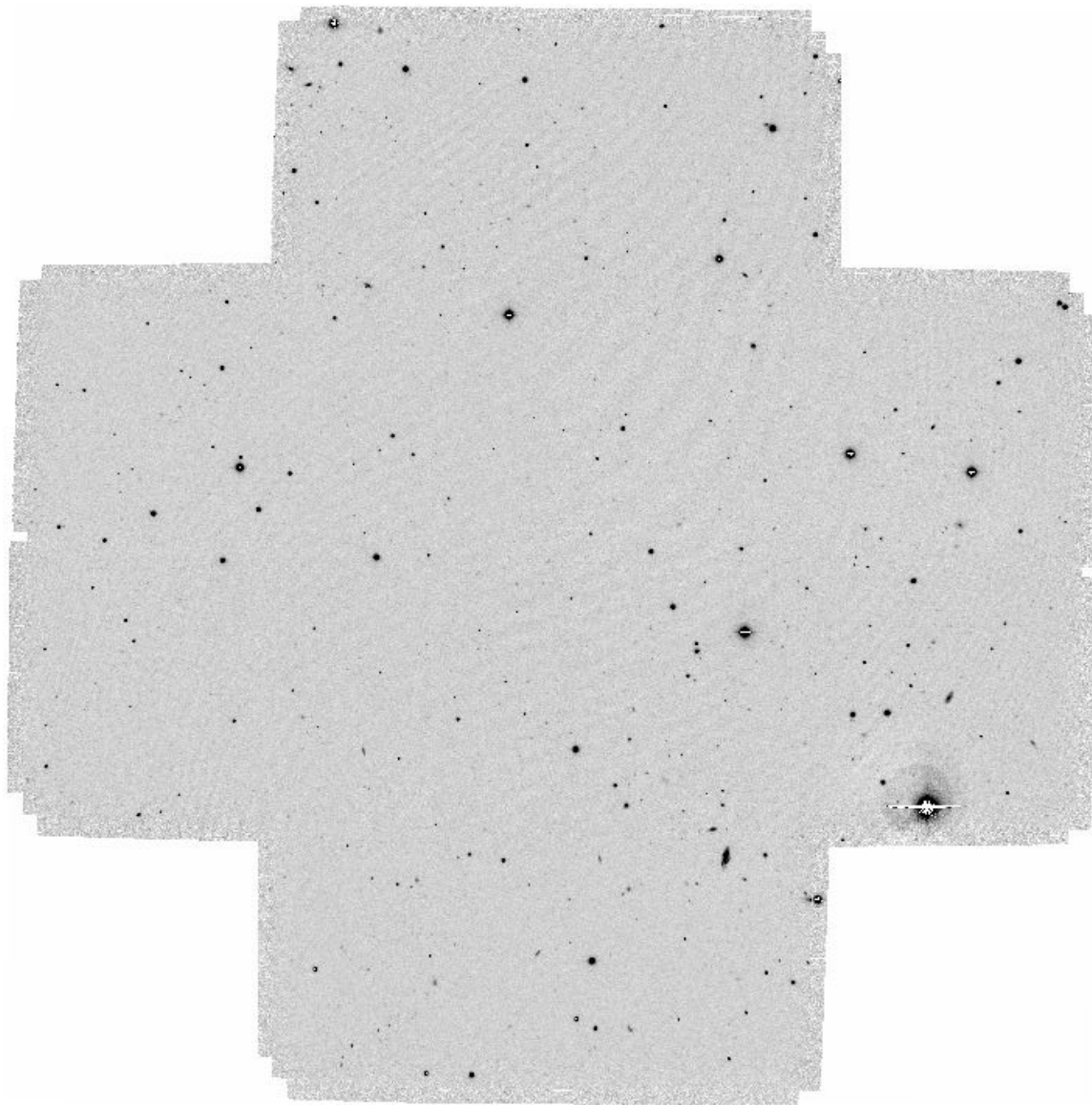Figure 5.12 An example of the final, stacked LFC u' image obtained by the methods described in this chapter. Note that a cosmetically clean result, with no obvious chip gap residuals, is possible. Some residual, structured noise is visible as a "cirrus" pattern; this comes from the electrical noise in the LFC's readout electronics, and most severely affects images in u' (because of the minimal sky background).

```
PACKAGE = immatch
   TASK = sregister

input   =                Q1234-g  The input images
referenc=                Q1234-r  Input reference images
output  =            Q1234-g.reg  The output registered images
(xmin   =                    1.)  Minimum logical x reference coordinate value
(xmax   =                 2046.)  Maximum logical x reference coordinate value
(ymin   =                    1.)  Minimum logical y reference coordinate value
(ymax   =                 2223.)  Maximum logical y reference coordinate value
(nx     =                  200)  Number of grid points in x
(ny     =                  200)  Number of grid points in y
(wcs    =                world)  The default world coordinate system
(xformat=               %10.3f)  Output logical x coordinate format
(yformat=               %10.3f)  Output logical y coordinate format
(rwxform=                     )  Output reference world x coordinate format
(rwyform=                     )  Output reference world y coordinate format
(wxforma=                     )  Output world x coordinate format
(wyforma=                     )  Output world y coordinate format
(fitgeom=                shift)  Fitting geometry
(functio=             legendre)  Type of coordinate surface to be computed
(xxorder=                   6)  Order of x fit in x
(xyorder=                   6)  Order of x fit in y
(xxterms=                half)  X fit cross terms type
(yxorder=                   6)  Order of y fit in x
(yyorder=                   6)  Order of y fit in y
(yxterms=                half)  Y fit cross terms type
(reject =                INDEF)  The rejection limit in units of sigma
(calctyp=                 real)  Transformation computation type
(geometr=            geometric)  Transformation geometry
(xsample=                   1.)  X coordinate sampling interval
(ysample=                   1.)  Y coordinate sampling interval
(interpo=                poly5)  The interpolant type
(boundar=             constant)  Boundary extensiontype
(constan=                   0.)  Constant for constant boundary extension
(fluxcon=                  yes)  Preserve image flux ?
(nxblock=                10000)  X dimension blocking factor
(nyblock=                  512)  Y dimension blocking factor
(wcsinhe=                  yes)  Inherit wcs of the reference image ?
(verbose=                  yes)  Print messages about progress of task?
(interac=                   no)  Compute transformation interactively?
(graphic=             stdgraph)  The standard graphics device
(gcomman=                     )  The graphics cursor
```

Figure 5.13 Example parameter set for registering stacked images with `sregister`.

```
PACKAGE = imcoords
TASK = wcsctran

input    =                grid.xy  The input coordinate files
output   =             grid.world  The output coordinate files
image    =             scratch[1]  The input images
inwcs    =                logical  The input coordinate system
outwcs   =                  world  The output coordinate system
(columns=                    1 2)  List of input file columns
(units   =          native native) List of input coordinate units
(formats=                  %f %f)  List of output coordinate formats
(min_sig=                      5)  Minimum precision of output coordinates
(verbose=                     no)  Write comments to the output file ?
```

Figure 5.14 Rotating solutions: Sample parameter set for converting grid coordinates from pixel to world with wcsctran.

```
PACKAGE = imcoords
   TASK = ccmap

input    =               rotate.out  The input coordinate files
database=                   New.db  The output database file
(solutio=                   LRISB1)  The database plate solution names
(images =               scratch[1])  The input images
(results=                        )  The optional results summary files
(xcolumn=                        1)  Column containing the x coordinate
(ycolumn=                        2)  Column containing the y coordinate
(lngcolu=                        3)  Column containing the ra / longitude
(latcolu=                        4)  Column containing the dec / latitude
(xmin   =                    INDEF)  Minimum logical x pixel value
(xmax   =                    INDEF)  Maximum logical x pixel value
(ymin   =                    INDEF)  Minimum logical y pixel value
(ymax   =                    INDEF)  Maximum logical y pixel value
(lngunit=                      deg)  Input ra / longitude units
(latunit=                      deg)  Input dec / latitude units
(insyste=                    j2000)  Input celestial coordinate system
(refpoin=                     user)  Source of the reference point definition
(lngref =                152.97495)  Reference point ra / longitude telescope coord
(latref =                 29.69472)  Reference point dec / latitude telescope coord
(refsyst=                    j2000)  Reference point telescope coordinate system
(lngrefu=                      deg)  Reference point ra / longitude units
(latrefu=                      deg)  Reference point dec / latitude units
(project=                      tnx)  Sky projection geometry
(fitgeom=                  general)  Fitting geometry
(functio=               polynomial)  Surface type
(xxorder=                        4)  Order of xi fit in x
(xyorder=                        4)  Order of xi fit in y
(xxterms=                     half)  Xi fit cross terms type
(yxorder=                        4)  Order of eta fit in x
(yyorder=                        4)  Order of eta fit in y
(yxterms=                     half)  Eta fit cross terms type
(maxiter=                        2)  The maximum number of rejection iterations
(reject =                       3.)  Rejection limit in sigma units
(update =                       no)  Update the image world coordinate system ?
(pixsyst=                  logical)  Input pixel coordinate system
(verbose=                      yes)  Print messages about progress of task ?
(interac=                      yes)  Fit the transformation interactively ?
(graphic=                 stdgraph)  Default graphics device
(cursor =                        )  Graphics cursor
```

Figure 5.15 Rotating solutions: Sample parameter set for creating the rotated solution with
`ccmap`.

Bibliography

Adelberger, K. L. 2002, PhD thesis, California Institute of Technology

Adelberger, K. L., & Steidel, C. C. 2000, *Astrophys. J.*, 544, 218

Alexander, D. M., Bauer, F. E., Brandt, W. N., Schneider, D. P., Hornschemeier, A. E.,
Vignali, C., Barger, A. J., Broos, P. S., Cowie, L. L., Garmire, G. P., Townsley, L. K.,
Bautz, M. W., Chartas, G., & Sargent, W. L. W. 2003, *Astron. J.*, 126, 539

Alexander, D. M., Brandt, W. N., Hornschemeier, A. E., Garmire, G. P., Schneider, D. P.,
Bauer, F. E., & Griffiths, R. E. 2001, *Astron. J.*, 122, 2156

Baldwin, J. A. 1977, *Astrophys. J.*, 214, 679

Barger, A. J., Cowie, L. L., Capak, P., Alexander, D. M., Bauer, F. E., Fernandez, E.,
Brandt, W. N., Garmire, G. P., & Hornschemeier, A. E. 2003, ArXiv Astrophysics e-
prints

Barger, A. J., Cowie, L. L., Mushotzky, R. F., & Richards, E. A. 2001, *Astron. J.*, 121, 662

Bershady, M. A., Charlton, J. C., & Geoffroy, J. M. 1999, *Astrophys. J.*, 518, 103

Boyle, B. J., Shanks, T., Croom, S. M., Smith, R. J., Miller, L., Loaring, N., & Heymans,
C. 2000, *Mon. Not. R. Astron. Soc.*, 317, 1014

Boyle, B. J., Shanks, T., & Peterson, B. A. 1988, *Mon. Not. R. Astron. Soc.*, 235, 935

Cristiani, S., Alexander, D. M., Bauer, F., Brandt, W. N., Chatzichristou, E. T., Fontanot,
F., Grazian, A., Koekemoer, A., Lucas, R. A., Monaco, P., Nonino, M., Padovani, P.,
Stern, D., Tozzi, P., Treister, E., Urry, C. M., & Vanzella, E. 2004, *Astrophys. J. Lett.*,
600, L119

Dunlop, J. S., & Peacock, J. A. 1990, *Mon. Not. R. Astron. Soc.*, 247, 19

Fan, X., Strauss, M. A., Richards, G. T., Newman, J. A., Becker, R. H., Schneider, D. P., Gunn, J. E., Davis, M., White, R. L., Lupton, R. H., Anderson, J. E., Annis, J., Bahcall, N. A., Brunner, R. J., Csabai, I., Doi, M., Fukugita, M., Hennessy, G. S., Hindsley, R. B., Ivezić, Ž., Knapp, G. R., McKay, T. A., Munn, J. A., Pier, J. R., Szalay, A. S., & York, D. G. 2001a, *Astron. J.*, 121, 31

Fan, X., Strauss, M. A., Schneider, D. P., Gunn, J. E., Lupton, R. H., Becker, R. H., Davis, M., Newman, J. A., Richards, G. T., White, R. L., Anderson, J. E., Annis, J., Bahcall, N. A., Brunner, R. J., Csabai, I., Hennessy, G. S., Hindsley, R. B., Fukugita, M., Kunszt, P. Z., Ivezić, Ž., Knapp, G. R., McKay, T. A., Munn, J. A., Pier, J. R., Szalay, A. S., & York, D. G. 2001b, *Astron. J.*, 121, 54

Fardal, M. A., Giroux, M. L., & Shull, J. M. 1998, *Astron. J.*, 115, 2206

Fardal, M. A., & Shull, J. M. 1993, *Astrophys. J.*, 415, 524

Ferland, G. J., & Osterbrock, D. E. 1986, *Astrophys. J.*, 300, 658

Gonzalez Delgado, R. M., Leitherer, C., Heckman, T., Lowenthal, J. D., Ferguson, H. C., & Robert, C. 1998, *Astrophys. J.*, 495, 698

Granato, G. L., Silva, L., Monaco, P., Panuzzo, P., Salucci, P., De Zotti, G., & Danese, L. 2001, *Mon. Not. R. Astron. Soc.*, 324, 757

Grazian, A., Negrello, M., Moscardini, L., Cristiani, S., Haehnelt, M. G., Matarrese, S., Omizzolo, A., & Vanzella, E. 2004, *Astron. J.*, 127, 592

Green, P. J., Schartel, N., Anderson, S. F., Hewett, P. C., Foltz, C. B., Brinkmann, W., Fink, H., Truemper, J., & Margon, B. 1995, 450, 51

Gunn, J. E., & Stryker, L. L. 1983, *Astrophys. J. Supp.*, 52, 121

Haardt, F., & Madau, P. 1996, *Astrophys. J.*, 461, 20

Haehnelt, M. G., Natarajan, P., & Rees, M. J. 1998, *Mon. Not. R. Astron. Soc.*, 300, 817

Ho, L. 1999, in ASSL Vol. 234: Observational Evidence for the Black Holes in the Universe, 157−+

Hornschemeier, A. E., Brandt, W. N., Garmire, G. P., Schneider, D. P., Barger, A. J., Broos, P. S., Cowie, L. L., Townsley, L. K., Bautz, M. W., Burrows, D. N., Chartas, G., Feigelson, E. D., Griffiths, R. E., Lumb, D., Nousek, J. A., Ramsey, L. W., & Sargent, W. L. W. 2001, *Astrophys. J.*, 554, 742

Hosokawa, T. 2002, *Astrophys. J.*, 576, 75

—. 2004, *Astrophys. J.*, 606, 139

Jakobsen, P., Boksenberg, A., Deharveng, J. M., Greenfield, P., Jedrzejewski, R., & Paresce, F. 1994, *Nature*, 370, 35

Jarvis, J. F., & Tyson, J. A. 1981, *Astron. J.*, 86, 476

Kauffmann, G., & Haehnelt, M. 2000, *Mon. Not. R. Astron. Soc.*, 311, 576

Kennefick, J. D., Djorgovski, S. G., & de Carvalho, R. R. 1995, *Astron. J.*, 110, 2553

Koo, D. C., & Kron, R. G. 1988, *Astrophys. J.*, 325, 92

Koo, D. C., Kron, R. G., & Cudworth, K. M. 1986, *Proc. Astron. Soc. Pacific*, 98, 285

Kormendy, J., & Richstone, D. 1995, *Ann. Rev. Astron. & Astrophys.*, 33, 581

Madau, P. 1995, *Astrophys. J.*, 441, 18

Magorrian, J., Tremaine, S., Richstone, D., Bender, R., Bower, G., Dressler, A., Faber, S. M., Gebhardt, K., Green, R., Grillmair, C., Kormendy, J., & Lauer, T. 1998, *Astron. J.*, 115, 2285

Massey, P., Strobel, K., Barnes, J. V., & Anderson, E. 1988, *Astrophys. J.*, 328, 315

McCarthy, P. J. 1993, *Ann. Rev. Astron. & Astrophys.*, 31, 639

Merritt, D., & Ferrarese, L. 2001, *Mon. Not. R. Astron. Soc.*, 320, L30

Miralda-Escudé, J., Haehnelt, M., & Rees, M. J. 2000, *Astrophys. J.*, 530, 1

Muller, G. P., Reed, R., Armandroff, T., Boroson, T. A., & Jacoby, G. H. 1998, in Proc. SPIE Vol. 3355, p. 577-585, Optical Astronomical Instrumentation, Sandro D'Odorico; Ed., 577–585

Mushotzky, R. F., Cowie, L. L., Barger, A. J., & Arnaud, K. A. 2000, *Nature*, 404, 459

Nandra, K., Mushotzky, R. F., Arnaud, K., Steidel, C. C., Adelberger, K. L., Gardner, J. P., Teplitz, H. I., & Windhorst, R. A. 2002, *Astrophys. J.*, 576, 625

Norman, C., Hasinger, G., Giacconi, R., Gilli, R., Kewley, L., Nonino, M., Rosati, P., Szokoly, G., Tozzi, P., Wang, J., Zheng, W., Zirm, A., Bergeron, J., Gilmozzi, R., Grogin, N., Koekemoer, A., & Schreier, E. 2002, *Astrophys. J.*, 571, 218

Oke, J. B., Cohen, J. G., Carr, M., Cromer, J., Dingizian, A., Harris, F. H., Labrecque, S., Lucinio, R., Schaal, W., Epps, H., & Miller, J. 1995, *Proc. Astron. Soc. Pacific*, 107, 375

Oke, J. B., & Gunn, J. E. 1982, *Proc. Astron. Soc. Pacific*, 94, 586

Papovich, C., Dickinson, M., & Ferguson, H. C. 2001, *Astrophys. J.*, 559, 620

Pei, Y. C. 1995, *Astrophys. J.*, 438, 623

Pettini, M., Rix, S. A., Steidel, C. C., Adelberger, K. L., Hunt, M. P., & Shapley, A. E. 2002, *Astrophys. J.*, 569, 742

Ridgway, S. E., Heckman, T. M., Calzetti, D., & Lehnert, M. 2001, *Astrophys. J.*, 550, 122

Sargent, W. L. W., Steidel, C. C., & Boksenberg, A. 1989, *Astrophys. J. Supp.*, 69, 703

Schmidt, M., Schneider, D. P., & Gunn, J. E. 1995, *Astron. J.*, 110, 68

Scott, J., Bechtold, J., Morita, M., Dobrzycki, A., & Kulkarni, V. P. 2002, *Astrophys. J.*, 571, 665

Shapley, A. E., Steidel, C. C., Adelberger, K. L., Dickinson, M., Giavalisco, M., & Pettini, M. 2001, *Astrophys. J.*, 562, 95

Shapley, A. E., Steidel, C. C., Pettini, M., & Adelberger, K. L. 2003, *Astrophys. J.*, 588, 65

Shaver, P. A., Hook, I. M., Jackson, C. A., Wall, J. V., & Kellermann, K. I. 1999, in ASP Conf. Ser. 156: Highly Redshifted Radio Lines, 163–+

Shull, J. M., Tumlinson, J., Giroux, M. L., Kriss, G. A., & Reimers, D. 2004, *Astrophys. J.*, 600, 570

Simcoe, R. A. 2003, PhD thesis, California Institute of Technology

Small, T. A., & Blandford, R. D. 1992, *Mon. Not. R. Astron. Soc.*, 259, 725

Sokasian, A., Abel, T., & Hernquist, L. 2002, *Mon. Not. R. Astron. Soc.*, 332, 601

Steidel, C. C., Adelberger, K. L., Giavalisco, M., Dickinson, M., & Pettini, M. 1999, *Astrophys. J.*, 519, 1

Steidel, C. C., Adelberger, K. L., Shapley, A. E., Pettini, M., Dickinson, M., & Giavalisco, M. 2003, *Astrophys. J.*, 592, 728

Steidel, C. C., & Hamilton, D. 1993, *Astron. J.*, 105, 2017

Steidel, C. C., Pettini, M., & Adelberger, K. L. 2001, *Astrophys. J.*, 546, 665

Steidel, C. C., Shapley, A. E., Pettini, M., Adelberger, K. L., Erb, D. K., Reddy, N. A., & Hunt, M. P. 2004, *Astrophys. J.*, 604, 534

Stengler-Larrea, E. A., Boksenberg, A., Steidel, C. C., Sargent, W. L. W., Bahcall, J. N., Bergeron, J., Hartig, G. F., Jannuzi, B. T., Kirhakos, S., Savage, B. D., Schneider, D. P., Turnshek, D. A., & Weymann, R. J. 1995, *Astrophys. J.*, 444, 64

Stern, D., Dey, A., Spinrad, H., Maxfield, L., Dickinson, M., Schlegel, D., & González, R. A. 1999, *Astron. J.*, 117, 1122

Stern, D., Moran, E. C., Coil, A. L., Connolly, A., Davis, M., Dawson, S., Dey, A., Eisenhardt, P., Elston, R., Graham, J. R., Harrison, F., Helfand, D. J., Holden, B., Mao, P., Rosati, P., Spinrad, H., Stanford, S. A., Tozzi, P., & Wu, K. L. 2002, *Astrophys. J.*, 568, 71

Vanden Berk, D. E., Richards, G. T., Bauer, A., Strauss, M. A., Schneider, D. P., Heckman, T. M., York, D. G., Hall, P. B., Fan, X., Knapp, G. R., Anderson, S. F., Annis, J., Bahcall, N. A., Bernardi, M., Briggs, J. W., Brinkmann, J., Brunner, R., Burles, S., Carey, L., Castander, F. J., Connolly, A. J., Crocker, J. H., Csabai, I., Doi, M., Finkbeiner, D., Friedman, S., Frieman, J. A., Fukugita, M., Gunn, J. E., Hennessy, G. S., Ivezić, Ž., Kent, S., Kunszt, P. Z., Lamb, D. Q., Leger, R. F., Long, D. C., Loveday, J., Lupton, R. H., Meiksin, A., Merelli, A., Munn, J. A., Newberg, H. J., Newcomb, M., Nichol,

R. C., Owen, R., Pier, J. R., Pope, A., Rockosi, C. M., Schlegel, D. J., Siegmund, W. A., Smee, S., Snir, Y., Stoughton, C., Stubbs, C., SubbaRao, M., Szalay, A. S., Szokoly, G. P., Tremonti, C., Uomoto, A., Waddell, P., Yanny, B., & Zheng, W. 2001, *Astron. J.*, 122, 549

Vestergaard, M. 2004, *Astrophys. J.*, 601, 676

Warren, S. J., Hewett, P. C., Irwin, M. J., & Osmer, P. S. 1991, *Astrophys. J. Supp.*, 76, 1

Warren, S. J., Hewett, P. C., & Osmer, P. S. 1994, *Astrophys. J.*, 421, 412

White, R. L., Becker, R. H., Gregg, M. D., Laurent-Muehleisen, S. A., Brotherton, M. S., Impey, C. D., Petry, C. E., Foltz, C. B., Chaffee, F. H., Richards, G. T., Oegerle, W. R., Helfand, D. J., McMahon, R. G., & Cabanela, J. E. 2000, *Astrophys. J. Supp.*, 126, 133

Willott, C. J., Rawlings, S., Blundell, K. M., Lacy, M., & Eales, S. A. 2001, *Mon. Not. R. Astron. Soc.*, 322, 536

Wolf, C., Wisotzki, L., Borch, A., Dye, S., Kleinheinrich, M., & Meisenheimer, K. 2003, *Astron. & Astrophys.*, 408, 499

Wyithe, J. S. B., & Loeb, A. 2002, *Astrophys. J.*, 581, 886

—. 2003, *Astrophys. J.*, 595, 614

Yu, Q., & Lu, Y. 2004, *Astrophys. J.*, 602, 603

Yu, Q., & Tremaine, S. 2002, *Mon. Not. R. Astron. Soc.*, 335, 965